ABSTRACT

Title of Thesis: PREDICTING THE SEISMIC SIGNATURE OF LAVA TUBES FOR THE EARTH, THE MOON, AND MARS

Linden Wike, Master of Science, 2024

Thesis Directed By: Professor Nicholas C. Schmerr
Department of Geology

Lava tubes are a type of volcanically-generated subsurface void structure found on Earth, the Moon, and Mars and hold the potential to serve as shelters for crew members, preservation sites of pristine geological samples, and locations of *in situ* resources. A key question for lava tube science is how to locate them through geophysical methods. Here, we create a workflow that locates and characterizes the geometry of subsurface voids. We build a suite of subsurface synthetic seismic wavefield models that contain lava tube structures and investigate which seismic method best images them. Our models show that the more readily detectable lava tube simulations have a geophone spacing of 0.5 m, variable diameter, and shallow ceiling depth; and reverse-time migration and phase-shift-plus-interpolation migration techniques produce more accurate lava tube reconstructions than the Kirchhoff method. The synthetic modeling serves as a benchmark for understanding seismic wave propagation around lava tubes and helps answer how voids on the Moon and Mars would be imaged through seismology.

PREDICTING THE SEISMIC SIGNATURES OF LAVA TUBES FOR THE EARTH, THE MOON, AND MARS

by

Linden Wike

Thesis submitted to the Faculty of the Graduate School of the
University of Maryland, College Park, in partial fulfillment
of the requirements for the degree of
Master of Science
2024

Advisory Committee:
Professor Nicholas C. Schmerr, Chair
Professor Vedran Lekić
Professor Laurent G.J. Montési
Dr. Jacob A. Richardson

Acknowledgements

I would like to thank my advisor, Dr. Nick Schmerr, for his mentorship and support.

I would also like to thank the following support and funding that helped me complete my research: Dr. Doyeon Kim, Dr. Jingchuan Wang, and Dr. Naoma McCall for their mentorship on modelling, simulating, and processing the lava tube data; the GEODES team; X. Mu for sharing his seismic codes with us; and Dr. Patrick Whelley and Dr. Mike Zanetti for sharing their LiDAR data.

This work was supported by the NASA SSERVI GEODES grant 80NSSC19M0216.

Table of Contents

List of Tables

List of Figures

Figure 5. Nine example Skull Cave *gmsh* models exported to JPEG image format and imported into MATLAB as matrices, which are assigned seismic velocities fitting the basaltic material and lava tube environments. These models have a 0.5 m grid spacing. a) 2.3 m diameter, 6 m depth; b) 2.3 m diameter, 25 m depth; c) 2.3 m diameter, 50 m depth; d) 23 m diameter, 6 m depth; e) 23 m diameter, 25 m depth; f) 23 m diameter, 50 m depth; g) 46 m diameter, 6 m depth; h) 46 m diameter, 25 m depth; i) 46 m diameter, 50 m depth.

Figure 6. LiDAR outline of the cross-section of Lava River Cave used to create the mesh geometries. This LiDAR section was collected under the seismic line in Figure 2 and represents the tube geometry at that location. The ceiling depth beneath the surface is 10 m.

Figure 7. Nine example Lava River Cave *gmsh* models exported to JPEG image format and imported into MATLAB as matrices, which are assigned seismic velocities fitting the basaltic material and lava tube environments. These models have a 0.5 m grid spacing. a) 5 m diameter, 5 m depth; b) 5 m diameter, 25 m depth; c) 5 m diameter, 50 m depth; d) 10 m diameter, 5 m depth; e) 10 m diameter, 25 m depth; f) 10 m diameter, 50 m depth; g) 20 m diameter, 5 m depth; h) 20 m diameter, 25 m depth; i) 20 m diameter, 50 m depth.

Figure 8. Synthetic FDM results for a lava tube. (left) Example FDM seismic waveform shot gather for sources 1-10 (spaced 0 m to 90 m every 10 m) for the Skull Cave model with a 23 m diameter, 25 m ceiling depth, and 0.5 m receiver spacing. Distance in meters correlates to the waveform index, or geophone locations, and amplitude is a measure of displacement. (right) The input velocity model used to

simulate the seismic shot gather. The material 1 (yellow; rock) has a velocity of 3.0 km/s, while material 2 (blue; air) has a P-wave velocity of 0.35 km/s. The FDM code does not incorporate densities.

Figure 9. Snapshots of the SPECFEM2D output for a 50 m-diameter void lacking mesh elements within a 300 m by 100 m box (Fig. 3). 181 stations (green) are deployed at the surface with a station spacing of 0.5 m. Seismic waves generated by the vertically-incident Ricker wavelet 100 Hz source at the surface (with amplitudes in red (positive) and blue (negative)) that propagate downward with time and reflect off the void space. a) time step 2000 at 0.02 s; b) time step 5000 at 0.05 s; c) time step 8000 at 0.08 s.

Figure 10. Setup of the 90 m seismic lines on the surface over each modeled tube. Upward-facing triangles represent the 10 m spaced sources. Downward-facing triangles represent the 0.5 m spaced receivers. The number of receivers is simplified to the first and final set of receivers along the 90 m line; the "~~~" represents seven more sections of 0.5 m spaced receivers between the sections shown.

Figure 11. Flowchart illustrating the steps taken in reflection processing the synthetic seismograms and the workflow for their respective migration techniques, discussed in Section 2.6.

Figure 12. Examples of migration results for a void model. The a) input velocity model, with P-wave velocity indicated in the scale, and our b) RTM reconstruction, c) Kirchhoff migration reconstruction, and d) PSPI migration reconstruction for the 46 m diameter, 25 m ceiling depth Skull Cave model with 0.5 m geophone spacing. Input parameters for the migrations are described in Section 2.5. Scale bars for the

migrations are amplitude as a measure of the displacement, with increased contrast to highlight void signatures.

Figure 13. a) Example of an RTM result showing the seismic waveform for the migration at each geophone. The region where we pick the depth to the ceiling of the lava tube is highlighted in red. b) First arrival picks at each receiver position for determining the misfit in depth between each migration method (RTM, Kirchhoff, PSPI) reconstruction of a tube and the input tube model (v-model). This example is for the 46 m diameter, 25 m ceiling depth Skull Cave model with 0.5 m geophone spacing.

Figure 14. a) Example of a PSPI result showing the seismic waveform for the migration below each geophone. The region where we pick the width of the lava tube is between the two vertical red lines with the green checkmark. The region where we denote failure to resolve tube width from is highlighted as the red box. Picks within the vertical lines do not add to the misfit, while picks within the red box add to the misfit. b) First arrival picks at each receiver for determining the total misfit in depth and width between each migration method (RTM, Kirchhoff, PSPI) and the input velocity model (v-model), measured in meters. This example is for the 46 m diameter, 25 m ceiling depth Skull Cave model with 0.5 m geophone spacing.

Figure 15. Example (left) image y from the reverse-time migration reconstruction of the input lava tube and (right) image x of the horizontal gradient of the velocity model that is used to evaluate the SSIM (Eq. 3). Future work would use a vertical gradient of the velocity field for a more accurate comparison.

Figure 16. Homogeneous migration model experiment. a) The migration velocity model is purely a basaltic background velocity (3 km/s). Results for b) RTM, c) Kirchhoff migration, and d) PSPI. For this model, the tube was 46 m diameter, 25 m ceiling depth, using the Skull Cave shape model with 0.5 m geophone spacing experimental design. Scale bars represent relative amplitude of the migrated seismic waveform.

Figure 17. Results for RTM for each of the nine Skull Cave model spaces for a 0.5 m geophone spacing. Scale bars represent relative amplitude of the migrated seismic waveform. The background model space is the same as in Figure 5.

Figure 18. Results for PSPI migrations for each of the nine Skull Cave model spaces for a 0.5 m geophone spacing. Scale bars represent relative amplitude of the migrated seismic waveform. The background model space is the same as in Figure 5.

Figure 19. Results for Kirchhoff migrations for each of the nine Skull Cave model spaces for a 0.5 m geophone spacing. Scale bars represent relative amplitude of the migrated seismic waveform. The background model space is the same as in Figure 5.

Figure 20. Results for RTM for each of the nine Lava River Cave model spaces for a 0.5 m geophone spacing. Scale bars represent relative amplitude of the migrated seismic waveform. The background model space is the same as in Figure 7.

Figure 21. Results for PSPI migrations for each of the nine Lava River Cave model spaces for a 0.5 m geophone spacing. Scale bars represent relative amplitude of the migrated seismic waveform. The background model space is the same as in Figure 7.

Figure 22. Results for Kirchhoff migrations for each of the nine Lava River Cave model spaces for a 0.5 m geophone spacing. Scale bars represent relative amplitude

List of Abbreviations

Finite-Difference Method (FDM)

Geophysical Exploration of the Dynamics and Evolution of the Solar System (GEODES)

Global positioning system (GPS)

Ground-penetrating radar (GPR)

LASer (LAS)

Lava Beds National Monument (LBNM)

Light, detection, and ranging (LiDAR)

Low-velocity zone (LVZ)

Kirchhoff (KIRK)

Multi-channel analysis of surface waves (MASW)

National Aeronautics and Space Administration (NASA)

Phase-shift-plus-interpolation (PSPI)

Reverse-time migration (RTM)

Root mean square error (RMSE)

San Francisco Volcanic Field (SFVF)

Spectral analysis of surface waves (SASW)

Spectral Element Method (SEM)

Solar System Exploration Research Virtual Institute (SSERVI)

Structural similarity matrix (SSIM)

University of Maryland (UMD)

Chapter 1: Introduction

1.1 Lava Tubes

Lava tubes are void spaces that form when a conduit filled with lava develops a solid ceiling. Initially, tubes are active, with lava still flowing through them; the void forms when the conduit is drained of lava. Lava tube dimensions on Earth vary from meters to kilometers in length, and meters to tens of meters in height, and have a rounded or hemispherical shape (Thienat et al. 2020, Sauro et al. 2020). Tube morphology is diverse, with geometries ranging from a single conduit, braided conduits, multi-level conduits, or a combination of morphologies (Sauro et al. 2020). There are four primary mechanisms by which lava tubes form: 1) over-crusting of lava channels, 2) shallow inflation of lava sheets, 3) deep-inflated entrenchment along lava flow boundaries, and 4) formation along pre-existing fractures and fissures (Sauro et al. 2020). For each of these four cases, the surface expressions of tubes can commonly be found in the form of collapse chains resulting from the gravitational effects of pressure from overburden; these collapse chains serve as evidence for extra-terrestrial lava tubes (Sauro et al. 2020).

1.2 Lava Tubes on the Moon and Mars

Basaltic volcanism on the Moon has spanned past 1 Ga, and there is evidence of eruptions even as early as within the last 100 Ma (Haruyama et al. 2009, Braden et al. 2014, Richardson et al. 2017, Xiao et al. 2015, Zhang et al. 2015). Evidence for lava tubes existing on the Moon and Mars comes from observations of discontinuous sinuous rilles (Hurwitz et al. 2013, Blair et al. 2017) and sinkholes in volcanic regions. The Marius Hills region on the Moon has a feature called Marius Hills Pit that is inferred to be a collapse pit or skylight leading into a lava tube (Haruyama et al. 2009, Haruyama et al. 2010). Study of Lunar Reconnaissance Orbiter Narrow Angle Camera visual data confirmed the hole to be a skylight leading into a large void space (Haruyama et al. 2009, Haruyama et al. 2010, van der Bogert 2010). Identified collapse pits and skylights (Haruyama et al. 2009, Wagner and Robinson 2014, Sauro et al. 2020) may be due to underlying lava tubes but may also be explained via alternate mechanisms (Sauro et al. 2020). The distinction between a sinuous collapse pit chain and a skylight (collapse specifically involved in lava tube formation) can be inferred from terrestrial analogs, as well as identification of vents along collapse chains containing potential skylights (Sauro et al. 2020). These characteristics were determined by Sauro (2020) through an Earth dataset of 120 jameos and skylights, a Moon dataset of twenty-seven collapses in three separate collapse chains, and a Mars dataset of 122 collapse tube candidates for three volcanic regions. Sauro (2020)'s identification of potential tubes led to estimations of the volumes of lunar and martian lava tubes to be respectively one to three orders of magnitude larger than terrestrial ones, with martian tubes following over-crusting and inflation (Earth-like) formation mechanisms and lunar tubes following the mechanism of deep inflation and thermal entrenchment (Sauro et al. 2020). Both lunar and martian tubes exhibit collapse, with the former due to impacts while the latter results from gravitational effects (Sauro et al. 2020). Lunar tubes, however, exist within the stability threshold and may remain intact for seismic detection and study (Blair et al. 2017).

1.3 The Importance of Lava Tubes

Lava tubes are a type of subsurface void on the Moon (Haruyama et al. 2009, Blair et al. 2017, Paris et al. 2019) and Mars (Sauro et al. 2020). The Moon and Mars are identified as key research and exploration targets in the most recent NASA Decadal Survey (National Academies of Sciences, Engineering, and Medicine 2023), with lava tubes holding the potential to aid in the objectives of the "Near-term Human Exploration Plans, Relationship to Science, and *In Situ* Resource Utilization" section. One of the programs designed to further our understanding of these planetary bodies is the Artemis Missions, which will be the next set of crewed missions to the Moon and form the basis for future crewed exploration of Mars (NASA 2020a, NASA 2020b). The science objectives of the Artemis program include understanding planetary processes through the lens of the Moon, characterizing the origin and location of lunar polar volatiles, conducting experimental science in the lunar environment, and investigating and mitigating exploration risks (NASA 2020a, NASA 2020b). Subsurface void spaces, including lava tubes, caves, and large-scale fractures, have the potential to serve as shelter (Kalita et al. 2021, Martin and Benaroya 2023) from a multitude of hazards (Reitz et al. 2012), such as impacts, weather, radiation, and unstable landing sites, for these crewed missions to extra-terrestrial surfaces. The formation and volcanic history of lunar and martian analog lava tubes on Earth impacts our understanding of these same processes on the Moon and Mars (Sauro et al. 2020). Turning a lava tube into a shelter is an example of *in* *situ* resource utilization, wherein crewed and uncrewed missions will use the resources available to further self-sustainability when outside of Earth's reach. Additionally, voids can preserve pristine rock samples, volatiles (Blair et al. 2017), and evidence of past biological signatures (Northup et al. 2012, Leveille 2011), furthering two of the Decadal Survey's topics of study: dynamic habitability and the search for life elsewhere (National Academies of Sciences, Engineering, and Medicine 2023). Thus, lava tubes may answer the key scientific questions concerning the search for life and the evolution of the shallow subsurface, as well as be a resource for scientific and exploratory objectives.

1.4 Void Space Detection

Void spaces include fractures, seams, karst media, sinkholes, or more general cavern spaces. There are multiple geophysical methods appropriate for detecting void spaces, including GPR (e.g., Esmaeili et al. 2020), magnetic (Bell et al. 2022), gravity (Kruger et al. 2002), and seismic techniques (Mirzanejad et al. 2021, Sloan et al. 2010). Kaku et al. (2017), used SELENE (Kaguya) Lunar Radar Sounder data to propose that peaks in the ground-penetrating radar (GPR) data correspond to the Marius Hill Pit lava tube's ceiling and floor. GPR has been used to explore the detection of terrestrial analog lava tubes, as well as in the modeling of simulated tubes on the Moon and Mars (Esmaeili et al. 2020, Wike et al. 2022). The Esmaeili et al. (2020) study utilized light, detection, and ranging (LiDAR), global positioning system (GPS), and GPR data sets collected at Lava Beds National Monument (LBNM) to identify lava tube reflections over Skull Cave and Valentine Cave (Whelley et al. 2021), with constraints on depth and size readily found. Esmaeili et al.

(2020) went on to model the GPR response of Valentine Cave and input lunar and martian material dielectric properties to conclude that similar methods of detection can be used on these planetary bodies.

Here, we focus on the detection of lava tubes using seismic methods. Seismic methods of void detection include refraction-based (Feigenbaum et al. 2019, Sheehan et al. 2005), surface waves (Park et al. 1999, Xia et al. 2006, Alam et al. 2021, Nolan et al. 2013, Phillips et al. 2002), reflection (Miller et al. 1991, Gritto et al. 2004, Peterie et al. 2009, Chalikakis et al. 2011), attenuation (Sherman et al. 2014, Buckley and Lane 2012), and combinations of two or more approaches (Nolan et al. 2011, Sherman et al. 2014, Sloan et al. 2010, Buckley and Lane 2012, Riddle et al. 2010, Peterie et al. 2009, Sloan et al. 2012).

Refraction-based methods utilize first arrival travel times and wave velocity tomography methods to identify low-velocity anomalies, noting that on the Moon, the void would function as a free surface. Feigenbaum et al. (2019) showed that a karst is associated with a low-velocity anomaly in refraction data. Pure refraction studies include delay-time and reciprocal methods (Shearer 2009) and use travel times for 2D or 3D tomography; however, these techniques are limited by refracted waves failing to image void spaces, analogous to lateral low-velocity zones (LVZ) (Shearer 2009). Sheehan et al. (2005) demonstrated this problem of inconclusive recovery of an LVZ through the comparison of both field data over karst regions and synthetics of wavefields modeling karst media when analyzed using the same suite of refraction tomography codes. The refraction LVZ problem makes it necessary to utilize multiple techniques of seismology for void detection, an objective of this project.

Surface wave methods are also useful for void detection and utilize ground roll, or Rayleigh waves (Park et al. 1999). Surface waves are versatile with a variety of applications, including use of the following: Rayleigh wave diffraction travel-time (Xia et al. 2006); joint Love and Rayleigh shear wave inversion, which together illustrate wave polarity and magnitude changes signaling voids (Alam et al. 2021); passive source multichannel surface wave detection of voids formed through salt dissolution that identified an increase in shear velocity surrounding the voids (Nolan et al. 2013); and applications of the spectral analysis of surface waves (SASW) method with multiple receivers, thus allowing for the implementation of the method with lateral heterogeneities, or voids (Phillips et al. 2002). While each of these methods has a degree of success in locating their target void, they lack a widespread application to diverse void spaces and are tailored to find voids of a predefined size and shape.

Reflection methods make use of traditional techniques to identify voids, such as analyzing seismic waves that are reflected from the impedance contrast at a void-rock interface. Processing steps that are employed during reflection analysis include signal processing steps such as common-depth-point acquisition, bandpass filtering, time windowing of data, experimental design steps including common-depth-point acquisition, and seismic processing of normal-moveout correction and comparison of the characteristic shape of the seismic moveout velocity interacting with void spaces as hyperbolic rather than linear (e.g., for the direct wave, air wave, and refracted wave) (Miller et al. 1991). Tomographic reflection analysis and 2D finite-difference modeling have been utilized together to locate subsurface features such as cracks

(Gritto et al. 2004). Diffraction-based methods are another void detection tool (Peterie et al. 2009). The field of karst exploration has extended reflection amplitude variations to map caverns' vertical boundaries to refraction techniques, providing a clearer picture near the surface (Chalikakis et al. 2011). This study of karst media has evolved into 2D full-waveform modeling efforts, with Zheng et al. (2016) proposing a scheme of modeling karst media at depth and successfully identifying resultant wavefield reflections.

Seismic methods provide more information when combined with multiple techniques. Nolan et al. (2011) conducted a joint refraction tomography and Multi-channel Analysis of Surface Waves (MASW) study to detect a subsurface void, with their results accurately locating the void at depth. A combination of surface wave methods, together with 1D and 2D scattering attenuation, was used to accurately locate two near-surface tunnels, but only for void spaces within one wavelength of the surface (Sherman et al. 2014). Techniques based on surface waves have also been utilized with diffraction and reflection methods. Sloan et al. (2010) presented a joint body wave diffraction, surface wave backscattering, and reflection moveout velocity analysis to detect wavefield effects of void spaces and their relation to surrounding media for modeled and real-world data. Buckley and Lane (2012) applied shear velocity and attenuation tomography, via traditional first arrival travel-time attenuation tomography and a total trace energy derived tomography method to locate near-surface void spaces. Their methods resulted in velocity and attenuation tomograms that consistently located the void spaces, yet they note the lack of application to deeper voids within complex subsurface structure.

Another option is to combine seismic methods with other geophysical methods, such as refraction tomography and electrical resistivity dipole-dipole tomography (Torrese et al. 2021). When utilized together these methods located a near-surface meter-scale tunnel within a drainage ditch, while individually their results were inconclusive (Riddle et al. 2010). Glaser et al. (2021) similarly applied a mix of electrical resistivity tomography and refraction seismology to detect a void space created after dewatering of the groundwater table.

Most past studies investigated specific void spaces with *a priori* knowledge on depth, size, or location; work remains to be done on identifying voids without prior knowledge. Sloan et al. (2012) worked to benchmark P-wave diffraction and surface wave backscattering techniques to locate known void spaces, but the data was analyzed blindly without background information and found ground-truth agreement across results. New methods can expand upon known results; for example, diffraction methods based on a traditional reflection study can image not only an original, known void, but previously unknown voids (Peterie et al. 2009). This is an example of a benchmarked tool, reflection, being extended to infer more about a known subsurface structure. To expand upon this, our developed technique is applied to a host of void spaces to demonstrate its robustness for variations in depth, size, and location: variations simulating a lack of *a priori* information.

A lack of *a priori* information will be the norm for future geophysical missions to the Moon and Mars, where ground truth will not be readily available, and require mission designs that are capable of navigating the often irregular and hazardous surface conditions within tubes. Geophysical tools such as this our workflow can be used to establish what void spaces can and should be explored into, with estimates of depth, size, and shape on hand. Here, I establish the viability of reflection seismic processing for characterizing voids of varying sizes using approximate morphologies from terrestrial analogs.

Chapter 2: Methods

Past work in void detection has established that seismology can identify void spaces. Here, we model the effect of a lava tube at depth on seismic waves and use the resulting wavefields to establish the most effective seismic processing workflow to retrieve the known structures. Our workflow is: 1) the definition of two terrestrial analog sites, 2) the construction of mesh model spaces for each site, 3) the synthetic simulation of seismic waves interacting with the lava tubes at depth using the finite-difference method (FDM), and 4) the evaluation of seismology's ability to define the input lava tube models through migration techniques.

2.1 Terrestrial Analog Lava Tubes

We define terrestrial analogs as locations on Earth with geologic and volcanic processes resembling those seen on other planetary bodies (e.g., the Moon and Mars). Terrestrial analogs have been used since the late 1950s for the Apollo missions' planning and execution (Shoemaker 1959, Bailey 1967). They provide the opportunity to combine modeled data with data gathered *in situ* during field expeditions and have been applied to studies of Mars (Marusiak et al. 2020) and more distant planetary bodies exhibiting volcanism (e.g., Io) (Mouginis-Mark and Wilson 2022). The Geophysical Exploration of the Dynamics and Evolution of the Solar System (GEODES) team selected Skull Cave and Lava River Cave as Earth analog lava tubes due to their shared basaltic volcanism with the Moon and Mars. In general, lava tubes on Earth vary on the order of 0.5 m to 30 m (Sauro et al. 2020); Skull Cave and Lava River Cave fall into the middle of this range at 23 m and 10 m in diameter, respectively, and are thus representative of a typical Earth lava tube.

2.1.1 Field Site 1: Skull Cave

The first selected location of study is Skull Cave (Fig. 1), located within the Modoc crater basaltic flow lava tube network within LBNM. The Modoc crater lava tube network originated from Medicine Lake shield volcano's eruptive history over the past 12 ka-500,000 ka (Donnelly-Nolan 2010). Skull Cave is 10-20 m in diameter (Esmaeili et al. 2020, Bell et al. 2022) with a basaltic overburden three to five meters thick over the tube roof (Esmaeili et al. 2020). The June 2023 GEODES field expedition collected co-located LiDAR, GPR, magnetic, and seismic data at a Skull Cave transect, with the intention of enabling a joint effort to resolve tube depth and spatial parameters. LiDAR data (Whelley et al. 2021) detected the upper segment of Skull Cave, which can be converted to *gmsh* format (Geuzaine and Remacle 2009) and implemented in FDM methods of seismic wavefield simulation. The LiDAR data of the interior of Skull Cave and the surface above it was collected by Whelley et al. 2021 using a Riegl VZ-400 tripod mounted terrestrial laser scanner, were geo-referenced into UTM coordinates, and archived in LAS (LASer) format. In June 2023, the GEODES team conducted a seismic line directly over Skull Cave. This line consisted of six 11.5 m overlapping segments (roughly 80.5 m total seismic line length), with receivers spaced every 0.5 m and sources every 1 m. Our synthetic modeling is designed to replicate this receiver spacing.

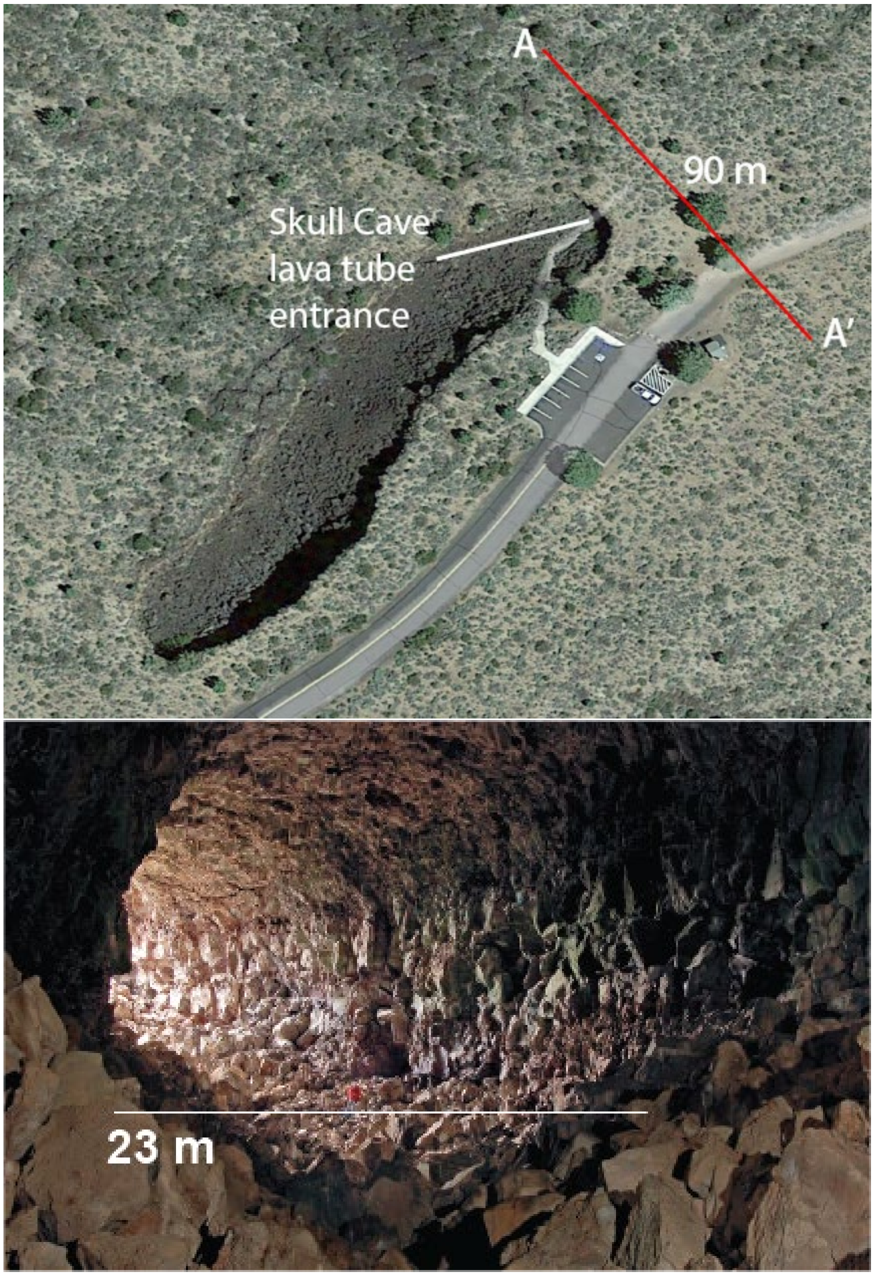

Figure 1. Skull Cave in Lava Beds National Monument. (top) Google Earth view of the location at which the 90 m synthetic line A(41°43'54.50"N by 121°30'38.94"W)to A’ (41°43'52.09"N by 121°30'36.47"W) would be situated over Skull Cave, at 16 m past the skylight. LiDAR data used for models corresponds to this location. (bottom) Image of the interior of Skull Cave, LBNM, field site 1, over the tube outline in

Figure 4. (Photo by National Park Service, Skull Cave, https://www.nps.gov/places/skull-cave.htm)

2.1.2 Field Site 2: Lava River Cave

The second tube we chose as a terrestrial analog is Lava River Cave (Fig. 2), located in the San Francisco Volcanic Field (SFVF). The SFVF is a young, late Cenozoic volcanic field made up of hundreds of volcanoes of basaltic and silicic compositions that overlies an early Pliocene rim basalt layer; the field decreases in age from west to east, with the oldest volcanic material originating 60 Ma and the youngest material at Sunset Crater 900 years ago (Gullikson 2021). A further overview of SFVF's geologic history is provided by Gullikson (2021), with the age of the flows increasing from east to west. During a previous field expedition LiDAR data for the tube was collected by Dr. Mike Zanetti, Marshall Space Flight Center, using the Kinematic Navigation and Cartography Knapsack (KNaCK). These data are not yet publicly available; however, Zanetti et al. (2024) described the KNaCK LiDAR instrument. We acquired LiDAR cross-sections below surface-level seismic lines, which implemented 0.5 m geophone spacing along an 83.5 m line. The LiDAR geometry data were acquired through via traversal of the interior of the lava tube and archived in LAS LiDAR point cloud format. Lava tube geometry for a specific cross-section was obtained via cross-reference two sources: 1) the Lava River Cave region map, available on the Forest Service website of the U.S. Department of Agriculture, and 2) the National Agricultural Image Program data for 3511142_NW detailing the surface. There is uncertainty on the order of meters in terms of reference lava tube ceiling depth and width. However, for the purposes of this research, we are scaling the lava tubes in depth and size to obtain a varied dataset at an order of magnitude larger than these meter-scale variations.

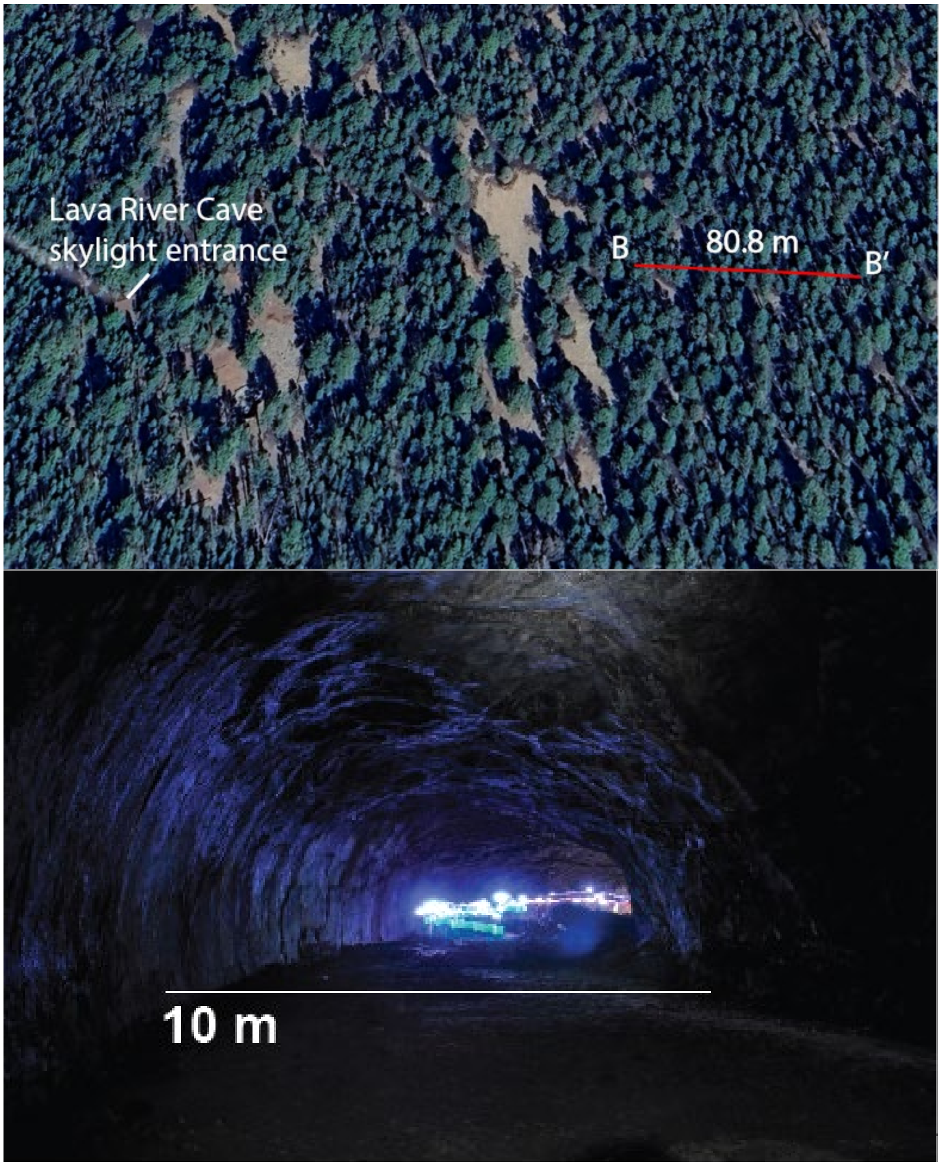

Figure 2. Lava River Cave in San Francisco Volcanic Field. (top) Google Earth view of the location at which the synthetic line B (35°20'33.25"N by 111°50'2.80"W) to B' (35°20'33.00"N by 111°49'59.59"W) would be placed over Lava River Cave, field site 2, over the tube outline in Figure 6. LiDAR data used for models corresponds to this location. (bottom) Long-exposure photograph of the interior of Lava River Cave,

AZ, field site 2. (Photo by Coconino National Forest Photography, Lava River Cave, August 2015, https://www.fs.usda.gov/recarea/coconino/recarea/?recid=55122)

2.2 Void Space Modeling

Wave propagation models of scattering cavities have been implemented for over sixty years from cylindrical cavities within solids scattering elastic waves (Gilbert and Knopoff 1960, Lewis et al. 1976, Liu et al. 2000). Seismic wave propagation models have been used in whole-earth scenarios (Wang et al. 2003) and in the implementation of 2D modeling of void spaces in karst media (Zheng et al. 2016). For the purpose of this thesis, seismic wave propagation is modeled using a forward model FDM MATLAB (The MathWorks, Inc 2022) code developed by X. Mu, with the implementation of mesh geometries from those we created via *gmsh* and MATLAB, for our analog tube locations.

2.3 Mesh Model Space and Seismic Simulation Parameters

2.3.1 Meshing the Models

Gmsh (Geuzaine and Remacle 2009) is an open-source finite element mesher that is used to create our lava tube models that contain a void space. The mesh space is defined as a nine-node second-order quadrangle, with four nodes corresponding to quadrangle vertices, four to quadrangle edges, and one to the face (Geuzaine and Remacle 2022); the physical properties of the medium (Table 1) are assigned at the nodes. In a simplistic model of a tube, the void space (Fig. 3, a) orange, b) grey) is represented as a 50 m diameter semicircle with its ceiling placed at 25 m depth within a basaltic medium (Fig. 3, green) and centered at 150 m horizontally. The floor of the tube is 50 m below the surface. Model dimensions are set to 300 m wide by 100 m deep to mitigate any effects of side reflections on the wavefield that may occur for smaller model spaces (e.g., 50 m wide by 25 m deep). A typical model has sub-meter mesh spacing and node point numbers on the order of a million. Limitations of *gmsh* include the restriction of defining only the boundary surfaces of the box as absorbing or free, but not within at the tube boundary; a mesh size factor representing the spacing between mesh elements that does not scale linearly with the total number of elements; and sequential creation of points and curves within the mesh, increasing computation time to develop the mesh. As an example, the mesh for a 46 m diameter Skull Cave lava tube model at 6 m ceiling depth contains $3 \cdot 10^6$ and $8 \cdot 10^5$ elements. For the purpose of this research, this level of fine mesh geometries and spacing was not required to satisfy the Courant condition (Courant et al. 1928, Courant et al. 1967), avoiding issues of high computation time. This combined with the ability to create voids without mesh elements inside of them (Fig. 3), makes *gmsh* appropriate as the modeling software for void studies.

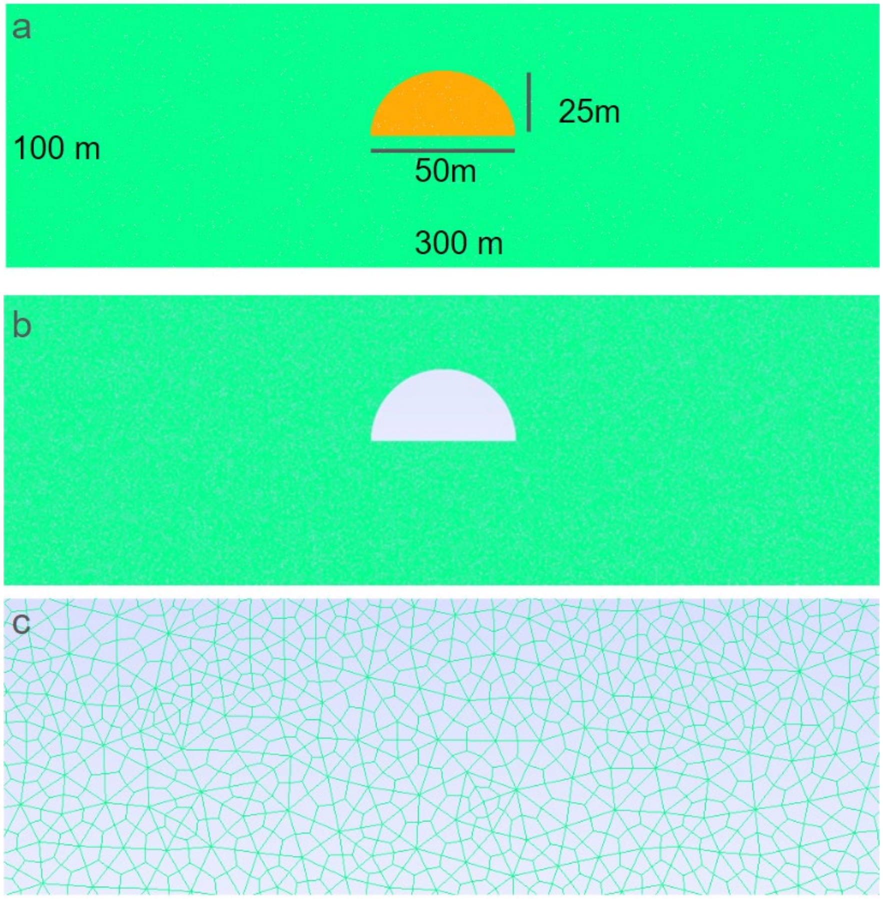

Figure 3. Example *Gmsh* mesh for a 50 m diameter void space filled with a) air or b) vacuum situated in an unconsolidated basaltic composition matrix. c) Zoom in on the mesh space with quadrangles at about one meter in diameter. Seismic properties of the materials are defined in Table 1.

Material	**P-wave Velocity (km s^{-1})**	**S-wave Velocity km s^{-1})**
Air	0.343	0.0
Void	0.0	0.0
Basalt, Skull Cave	3.0	1.5
Basalt, Lava River Cave	1.5	0.75
Consolidated Basalt	5.0-6.0	2.8-3.4

Table 1. Properties of the air, void, unconsolidated basalt (Skull Cave, Lava River Cave), and consolidated basalt materials utilized in our seismic simulations. Values obtained from Christensen and Stanley (2003) and GeoSci Developers (2017).

2.3.2 Skull Cave Models

Based upon LiDAR (Fig. 4) data we created a total of nine models for Skull Cave collected at this site. Each tube model is constructed in *gmsh*, with a mesh grid size factor, or scalar value of the distance between nodes, of one (Fig. 5), and sub-meter point spacing, and converted into JPEG image format to inject into MATLAB as a matrix. This is done by recording points from the LiDAR data that define the lava tube outline and using said points to create a *gmsh* shape corresponding to the lava tube within a box (Fig. 4). We originally chose *gmsh* for mesh creation as it can be used in SPECFEM2D (Komatitsch and Vilotte 1998) wave simulations, discussed further in Section 2.4. Rather than recreate the mesh spaces via MATLAB or other software, the *gmsh* meshes were exported to JPEG raster format and converted into MATLAB format as matrices with assigned seismic wave velocities at each index. These matrices are then utilized by our seismic wavefield simulation code to model wave interactions with the lava tubes at depth.

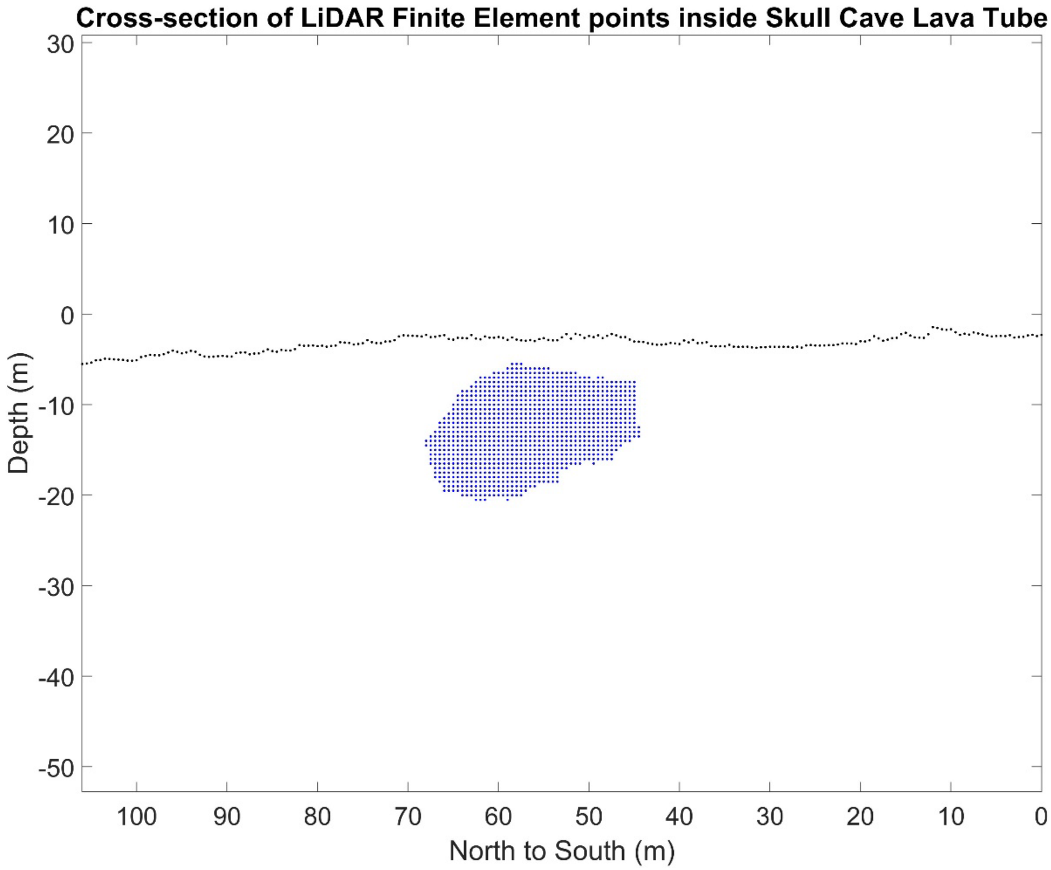
Cross-section of LiDAR Finite Element points inside Skull Cave Lava Tube
30
20
10
0
-10
-20
-30
-40
-50
Depth (m)
100
90
80
70
60
50
40
30
20
10
0
North to South (m)

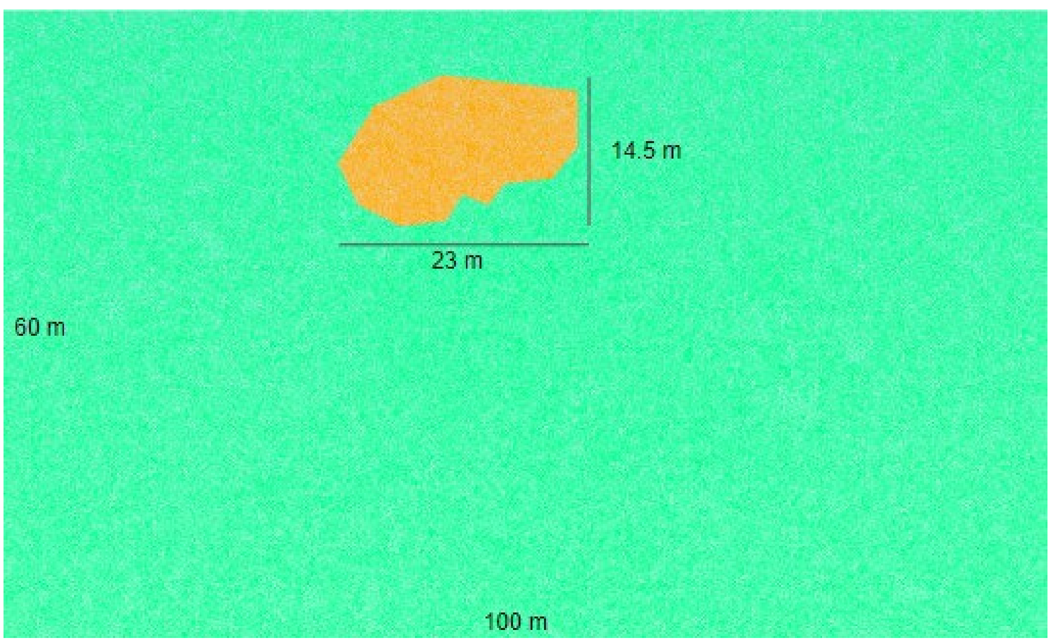
14.5 m
23 m
60 m
100 m

Figure 4. (top) Cross-section of Skull Cave from LiDAR data (courtesy of Dr. E. Bell, data from Whelley et al. 2021). (bottom) *Gmsh* recreation of the Skull Cave geometry at depth.

We vary the Skull Cave tube geometry model across three parameters: depth, size, and receiver, or geophone, spacing. The spacing between receivers is 0.5 m, 1.0 m, and 2.0 m. For each of the three receiver spacing sets, there are three depth variations and three size variations: a 2.3 m diameter tube at 6 m, 25 m, and 50 m ceiling depths; a 23 m diameter tube at 6 m, 25 m, and 50 m ceiling depths; and a 46 m diameter tube at 6 m, 25 m, and 50 m ceiling depths. These tubes are padded on the sides with absorbing boundaries totaling thirty grid elements to mitigate undesirable boundary reflections.

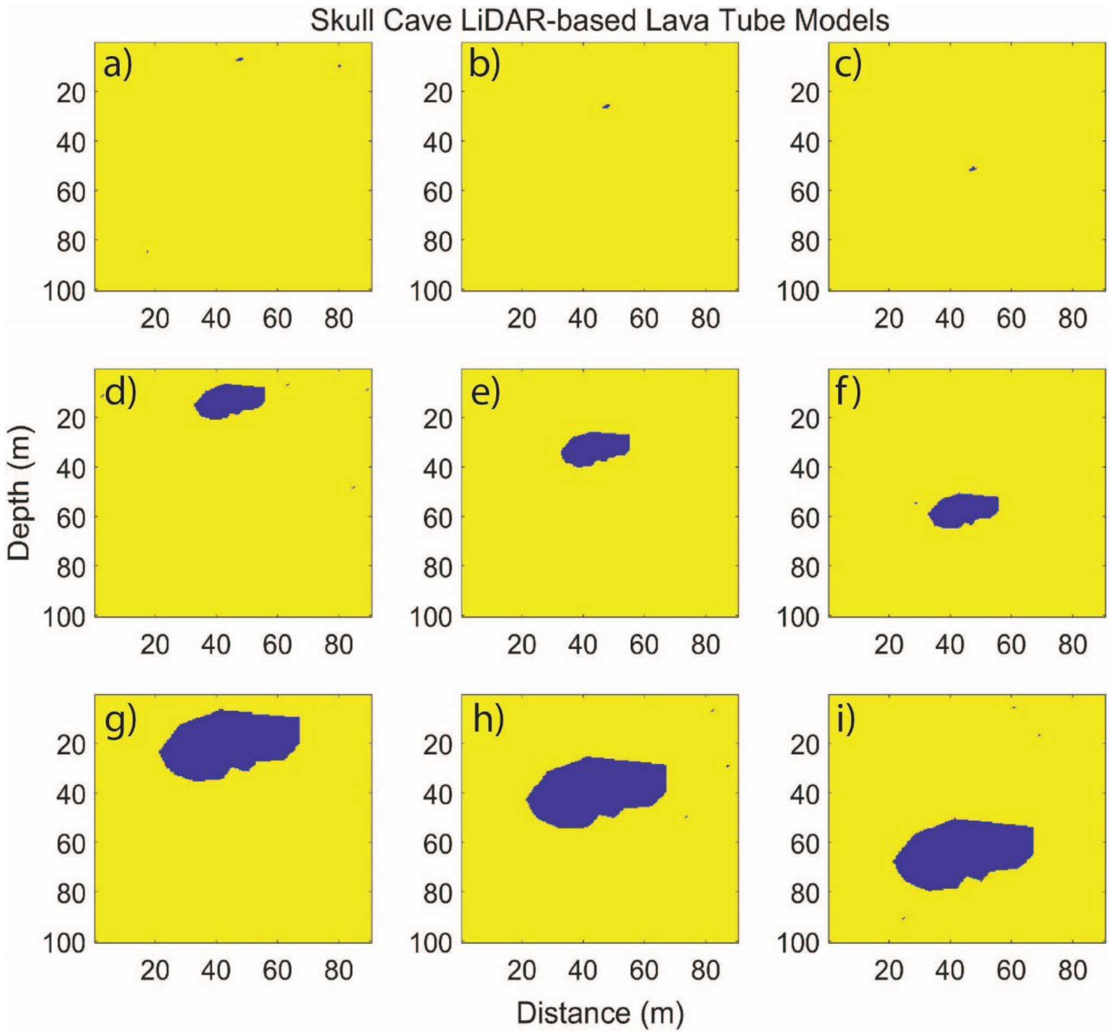

Figure 5. Nine example Skull Cave *gmsh* models exported to JPEG image format and imported into MATLAB as matrices, which are assigned seismic velocities fitting the basaltic material and lava tube environments. These models have a 0.5 m grid spacing. a) 2.3 m diameter, 6 m depth; b) 2.3 m diameter, 25 m depth; c) 2.3 m diameter, 50 m depth; d) 23 m diameter, 6 m depth; e) 23 m diameter, 25 m depth; f) 23 m diameter, 50 m depth; g) 46 m diameter, 6 m depth; h) 46 m diameter, 25 m depth; i) 46 m diameter, 50 m depth.

2.3.3 Lava River Cave Models

An additional nine *gmsh* models for Lava River Cave are constructed from LiDAR (Fig. 6), following the same guidelines as for Skull Cave (Fig. 7), with the same box size and dimensions. We vary the receiver spacing between 0.5 m, 1.0 m, and 2.0 m to explore how it affects the initial nine models. For each of the three grid spacing sets, there are three depth variations and three size variations: a 5 m diameter tube at 5 m, 25 m, and 50 m ceiling depths; a 10 m diameter tube at 5 m, 25 m, and 50 m ceiling depths; and a 20 m diameter tube at 5 m, 25 m, and 50 m ceiling depths. These tubes are likewise padded with absorbing boundaries to mitigate undesirable boundary reflections.

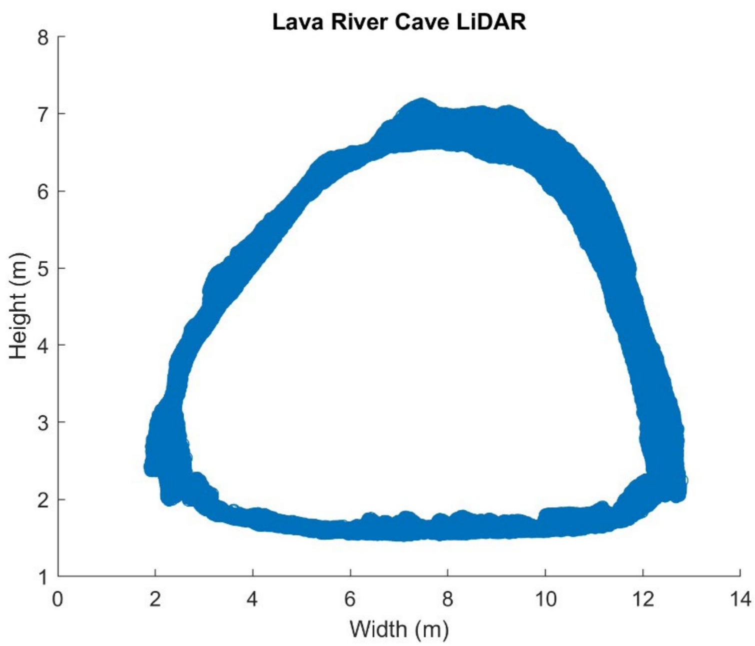

Figure 6. LiDAR outline of the cross-section of Lava River Cave used to create the mesh geometries. This LiDAR section was collected under the seismic line in Figure 2 and represents the tube geometry at that location. The ceiling depth beneath the surface is 10 m.

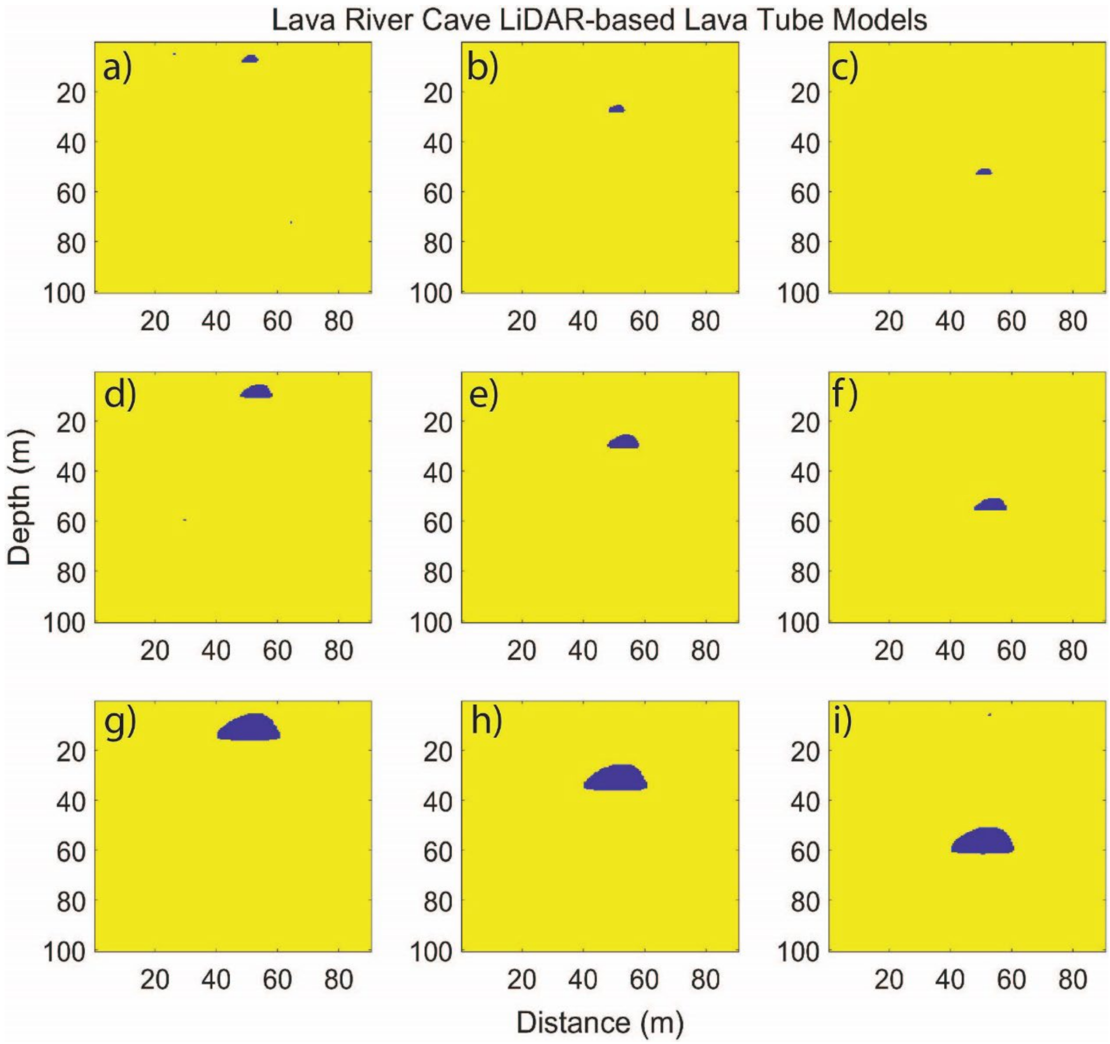

Figure 7. Nine example Lava River Cave *gmsh* models exported to JPEG image format and imported into MATLAB as matrices, which are assigned seismic velocities fitting the basaltic material and lava tube environments. These models have a 0.5 m grid spacing. a) 5 m diameter, 5 m depth; b) 5 m diameter, 25 m depth; c) 5 m diameter, 50 m depth; d) 10 m diameter, 5 m depth; e) 10 m diameter, 25 m depth; f) 10 m diameter, 50 m depth; g) 20 m diameter, 5 m depth; h) 20 m diameter, 25 m depth; i) 20 m diameter, 50 m depth.

2.4 Synthetic Seismograms

2.4.1 Spectral Element Method and Finite-Difference Method

Seismic wave simulation methods include the FDM (Tezuka 2006, Tromp 2015), the Pseudospectral Method (Tromp 2015), the Rayleigh-Ritz Method, the Finite-Element Method (FEM) (Tezuka 2006, Tromp 2015), and the Spectral Element Method (SEM) (Tromp et al. 2008, Tromp 2015). The FDM and Pseudospectral methods are based in reformatting the seismic wave equation (Equation 1) in terms of the velocity-stress formulation, or in terms of first-order space and time derivatives.

$$\frac{\partial^2 u}{\partial^2 t} = v^2\left(\frac{\partial^2 u}{\partial^2 x} + \frac{\partial^2 u}{\partial^2 z}\right) \tag{1}$$

Equation 1 is the wave equation. The variables are as follows: u represents the wavefield displacement and varies in space and time, t represents time, v represents the material velocity field, a constant, and x and z represent the spatial dimensions with x the horizontal, and z the vertical directions. The FDM code (courtesy of X. Mu) solves these derivatives via difference between grid points; the resultant wavefield becomes increasingly inaccurate towards the edges of a defined grid domain; this can lead to problems in free surface implementation and modeling of surface waves (Tromp 2015), two key factors in modeling of voids and heterogeneous void media. For the FDM methodology we employ here, grid dispersion is accounted for by padding our mesh spaces with absorbing boundaries surrounding the model space, widening the range of the grid to increase the accuracy of the simulation within the region of interest. An example seismic shot gather resultant from an input Skull Cave geometry is illustrated in Fig. 8. The code uses a second order in time and tenth order in space scheme to solve Equation 1 via the FDM, shown as Equation 2, and the following finite-difference coefficients: -2.9272, 1.6667, -0.2381, 0.0397, -0.0050, 0.0003.

$$u_{i,j}^{k+1} = 2u_{i,j}^{k} - u_{i,j}^{k-1} + \frac{1}{2}\left(\frac{v\Delta t}{\Delta x}\right)^2 \left[a_0 u_{i,j}^{k} + \sum_{m=1}^{L} a_m \left(u_{i+m,j}^{k} + u_{i-m,j}^{k}\right)\right] + \frac{1}{2}\left(\frac{v\Delta t}{\Delta z}\right)^2 \left[a_0 u_{i,j}^{k} + \sum_{m=1}^{L} a_m \left(u_{i,j+m}^{k} + u_{i,j-m}^{k}\right)\right]$$

where $u_{i+p,j+q}^{k+r} = u(x + p\Delta x, z + q\Delta z, t + r\Delta t)$.

(2)

Equation 2 is the FDM solution to Equation 1. The variables are as follows: *u* represents displacement as a function of space and time, *t* represents time, *v* represents P-wave velocity, *x* and *z* represent the two space dimensions, and a_0 and a_m are coefficients. *L* denotes the order of the solution, where we use a 2nd order in time and 10th order in space approximation.

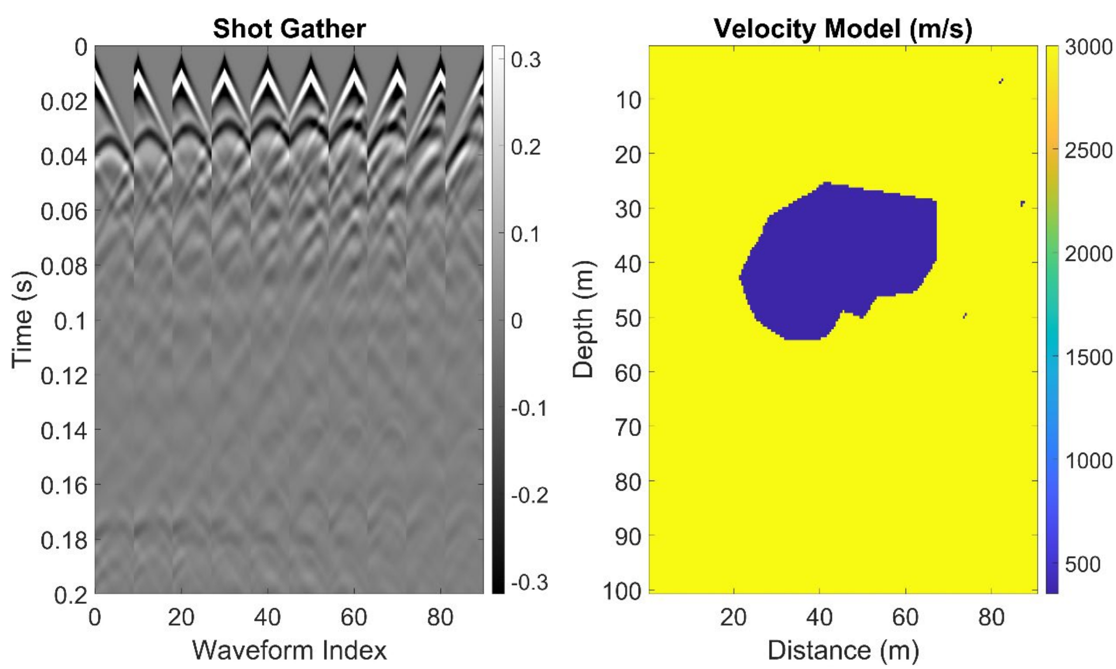

Figure 8. Synthetic FDM results for a lava tube. (left) Example FDM seismic waveform shot gather for sources 1-10 (spaced 0 m to 90 m every 10 m) for the Skull Cave model with a 23 m diameter, 25 m ceiling depth, and 0.5 m receiver spacing. Distance in meters correlates to the waveform index, or geophone locations, and amplitude is a measure of displacement. (right) The input velocity model used to simulate the seismic shot gather. The material 1 (yellow; rock) has a velocity of 3.0 km/s, while material 2 (blue; air) has a P-wave velocity of 0.35 km/s. The FDM code does not incorporate densities.

The FDM code we use implements a stability check to confirm that the input space steps and time steps of our simulations satisfy the Courant condition (Courant et al. 1928, Courant et al. 1967). The condition is satisfied if the time step is less than the square root of two multiplied by the minimum of the difference in space steps divided by pi and the maximum velocity (Eq. 4). Each of our simulations uses a time step of $5 \cdot 10^{-4}$ and varying space steps of 0.5, 1.0, and 2.0. The space steps in the *x* and *z* dimensions are always equal (i.e., *dx*/*dz* is always one). The minimum velocity in our models is 350 m/s for an air-filled tube and the maximum velocity in our models is 1500 m/s or 3000 m/s for a basaltic medium. The right-hand-side of the equation has values of $1.3 \cdot 10^{-3}$, $3 \cdot 10^{-4}$, or $1.5 \cdot 10^{-4}$ for the three velocities (350 m/s, 1500 m/s, 3000 m/s) used in our simulations, these values are all greater than the time step of $5 \cdot 10^{-4}$. Therefore, we find that our simulations satisfy the Courant condition for stable seismic simulation of the wavefield.

$$dt < 2^{1/2} \times \frac{\text{minimum}\left(\frac{dx}{dz}\right)}{\pi \times \text{maximum}(v)} \quad (4)$$

Prior to our work with the FDM, we investigated using the SEM for our simulations and analysis. For this work, we used the open-source full-waveform inversion software *SPECFEM2D* (Komatitsch and Vilotte 1998), parallel version 8.0.0. *SPECFEM2D* is an open-source simulator of acoustic, elastic, viscoelastic, or poroelastic seismic wave propagation (Komatitsch and Vilotte 1998) that can intake external meshes (i.e., *gmsh*). It utilizes a 2D spectral element solver that follows the SEM, combining the benefits of a PM's accuracy and a FEM's flexibility (Tromp et al. 2008), with suitability for parallel computing (Tromp 2015). A Python code included in the *SPECFEM2D* version 8.0.0 package converts the *gmsh* model into *SPECFEM2D's* format. The code is written by Cristini Paul, Laboratoire de Mecanique et d'Acoustique, CNRS, Marseille, France. Simulation parameters are set via source and parameter text files before simulations were run using the University of Maryland's HPCC Deepthought2 and Zaratan clusters (https://hpcc.umd.edu/). We define the basaltic composition matrix surrounding the void space as 1600 kg/m^3 density, 3 km/s P-wave velocity, and 1.5 km/s S-wave velocity. For models that contain a mesh within the tube, vacuum is defined as 10 kg/m^3 density, 0.001 km/s P-wave velocity, and 0 km/s S-wave velocity; as an air-filled cavity, it is defined as having 1.204 kg/m^3 density, 0.343 km/s P-wave velocity, and 0 km/s S-wave velocity. We note that SPECFEM2D cannot implement zero density and zero P-wave velocity; hence our choice for the lowered the density and velocity for the initial vacuum scenario to create a large impedance contrast that replicates the properties of the free surface. This code outputs BXZ and BXX files containing the vertical and horizontal components of the wavefield, as well as image snapshots taken at timestep intervals (Fig. 9). We evaluated the scenario for vacuum-in-void simulations through removal of mesh elements from the lava tube regions (*SPECFEM2D* would not have to assign density at these points, negating the zero-density problem) in the models and found agreement between our low density and P-wave void simulations (Fig. 3, Fig. 9).

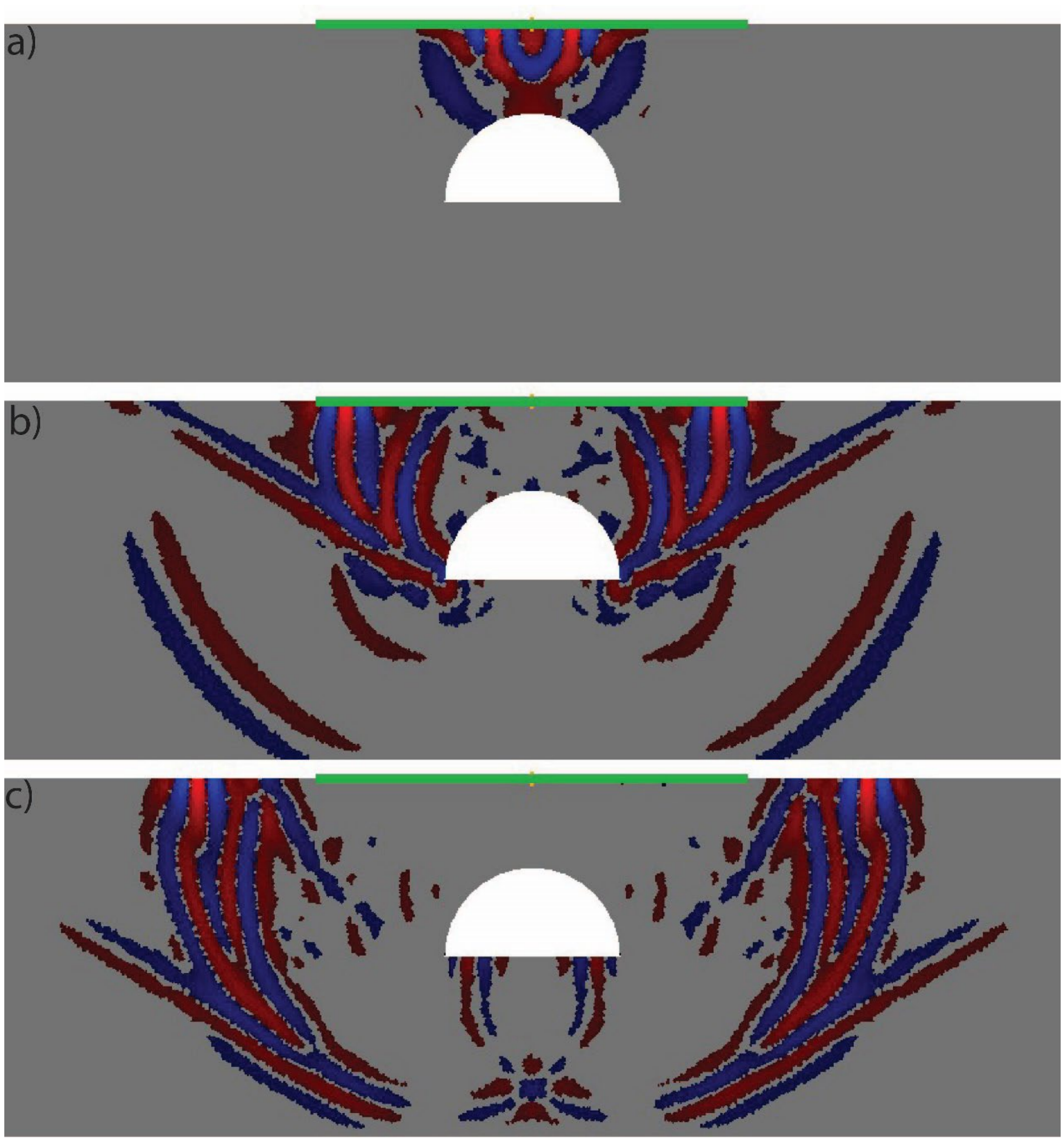

Figure 9. Snapshots of the SPECFEM2D output for a 50 m-diameter void lacking mesh elements within a 300 m by 100 m box (Fig. 3). 181 stations (green) are deployed at the surface with a station spacing of 0.5 m. Seismic waves generated by the vertically-incident Ricker wavelet 100 Hz source at the surface (with amplitudes in red (positive) and blue (negative)) that propagate downward with time and reflect off the void space. a) time step 2000 at 0.02 s; b) time step 5000 at 0.05 s; c) time step 8000 at 0.08 s.

Ultimately, we chose not to use *SPEFEM2D* and instead used FDM for our analysis due to the latter method being more cost-effective. Its cost-effectiveness is mainly due to the acoustic-only nature which takes into account the P-waves and excludes S-waves and surface waves from the simulations, thus simplifying the synthetic wavefield created. Our SEM synthetics with the same model space and seismic waveforms took on the order of 20 hours to complete a single simulation, while the FDM analyses took on the order of 15 minutes to complete. We did not note a decrease in fidelity of the seismic waveforms created between the two methods beyond the lack of S-waves and surface waves. For our research, we look at only the P-wave propagation. Both simulation results are provided as supplementary material described in Appendix A for future validation efforts. A direct comparison between the two methods is left for future work.

2.4.2 FDM Simulation Parameters

Each of the simulations utilizes source, receiver, and media parameters that match fieldwork expeditions to these locations, derived from adaptation of seismic line length and receiver spacing along it, as well as expected general basaltic material properties (Table 1). All fifty-four simulations contain ten total 100 Hz center frequency sources, spaced 10 m apart along a 90 m line of seismic receivers (geophones) (Fig 10). The source frequency and spacing match those we have used in fieldwork expeditions, while the receiver spacings between simulations are variable (0.5 m, 1.0 m, 2.0 m). These geophones are variably spaced to simulate the balance between time-effective (higher receiver spacing) and data-effective (lower receiver spacing) field experiments. There is a tradeoff between the number of stations, the number of receivers, the receiver spacing, and the time it takes to conduct a seismic experiment that impacts the time-effectiveness, cost-effectiveness, and data-effectiveness of an experiment; here, we analyze these parameters through only varying the receiver spacing. Increasing receiver spacing decreases receiver number, as line length remains the same, and increases time-effectiveness while lowering data-effectiveness. Decreasing receiver spacing increases receiver number and increases data effectiveness while lowering time-effectiveness. The costliest, in terms of time, 90 m line of receivers has 181 total geophones spaced every 0.5 m (Fig. 10), while the second line has them spaced every 1.0 m, and the final, least time cost setup, has geophones every 2.0 m. The finest-sampled line imitates the geophone geometry of the seismic experiments conducted by the GEODES team over Skull Cave and Lava River Cave. Future work would down-sample receivers from the synthetics to simulate larger receiver spacings (e.g., down sample the 1.0 m scenario by five to get 5.0 m spacing).

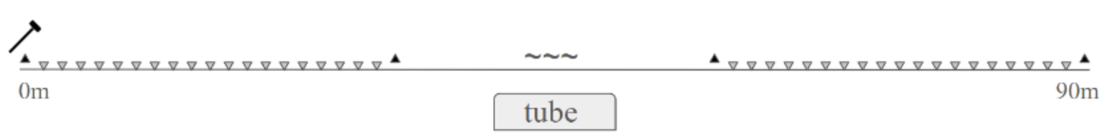

Figure 10. Setup of the 90 m seismic lines on the surface over each modeled tube. Upward-facing triangles represent the 10 m spaced sources. Downward-facing triangles represent the 0.5 m spaced receivers. The number of receivers is simplified to the first and final set of receivers along the 90 m line; the "~~~" represents seven more sections of 0.5 m spaced receivers between the sections shown.

2.5 Reflection Processing Methods

Our reflection seismic experiments are then processed via three different migration tools 1) RTM, 2) PSPI, and 3) Kirchoff migration, to compare and contrast recovery of the underlying tube structure. For reverse-time migration (RTM), we implement the same underlying FDM code as for simulating the seismic waveforms, using the finite-difference order and coefficients as in Section 2.4.1, and apply a Laplacian filter (Youn and Zhou 2001, Yang et al. 2020, Mousavi et al. 2022) to remove low-frequency artifacts of the RTM method, defined as: L = [0 -1 0; -1 4 -1; 0 -1 0] Hz. For the other two methods (Kirchoff and PSPI) we apply common-midpoint stacking to our data before employing each migration technique. For the latter two migration techniques, we also implement a normal-moveout velocity, with the common-midpoint method utilizing a velocity minimum and maximum of 1 km/s and 3 km/s. Normal moveout, common-midpoint stacking, and velocity model manipulation and analysis all use open-source code developed by Sacchi and Hall (2022). We use the CREWES MATLAB Software Package (Margrave and Lamoureux 2019) codes for Kirchhoff and PSPI migration. For PSPI migration, we specify a frequency range of 5 Hz to 300 Hz to be migrated, otherwise we input the CREWES default parameters. For Kirchhoff migration these defaults are a migration aperture the length of the migrated section, an aperture taper equal to five percent of the aperture, a cosine taper, a maximum dip limit angle of 60 degrees, an angle limit taper equal to fifteen percent of the limit angle, a cosine angle taper, a linear interpolation, minimum and maximum migration time windows equal to the full simulation time, and no box-car filter applied to the migration. For PSPI migration the defaults are no specified depth of expected migration section, a temporal pad created every five time steps to remove any possible effects of temporal wraparound. These methods are outlined in Fig. 11.

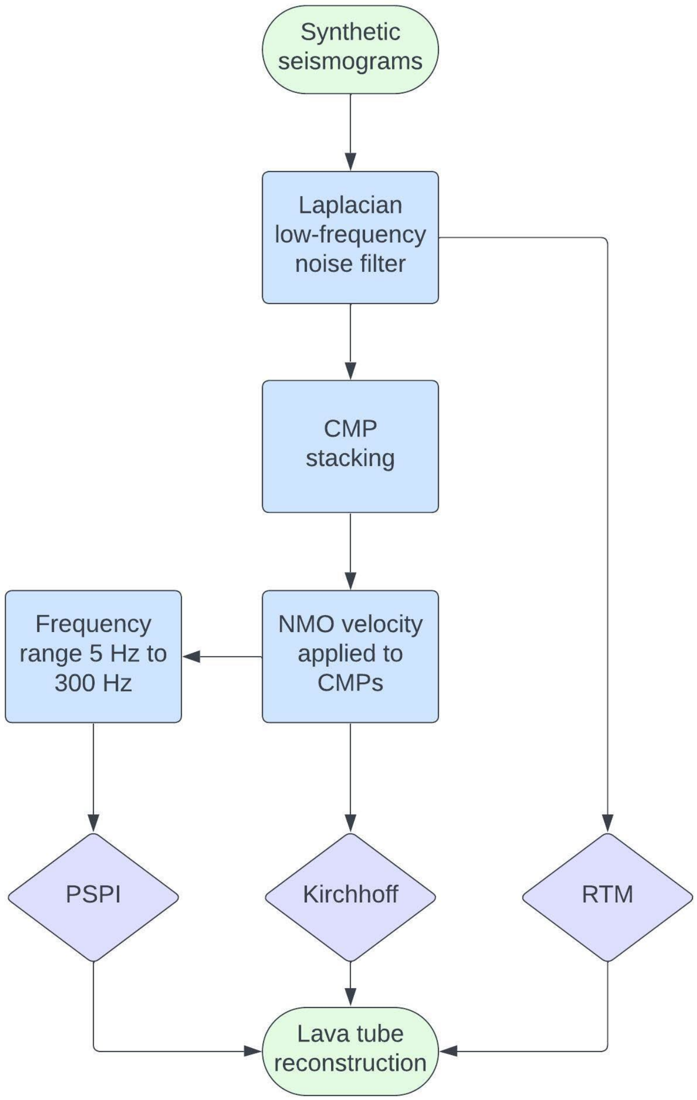

Figure 11. Flowchart illustrating the steps taken in reflection processing the synthetic seismograms and the workflow for their respective migration techniques, discussed in Section 2.6.

2.6 Migration Methods

A comparison of the efficiencies of each of the RTM, Kirchhoff, and PSPI methods of depth migration (Bednar 2005) in both isotropic and anisotropic media was presented in Du et al. (2006). They evaluated the trades between method cost (computational time to complete the migration), and method accuracy (ability to recover the starting model). Their study found that Kirchhoff migration is the most cost-effective, that RTM the most accurate, but computationally expensive, and that PSPI migration the balance between accuracy and computational cost. This study extends the comparison of the three methods to migration within media containing void spaces (Fig. 11, Fig. 12).

The Kirchhoff migration method has been utilized extensively to determine the structure and depth of subsurface features for seismic and GPR methods (Zhu and Lines 1998, Smitha et al. 2016, Esmaeili et al. 2019, Buske 1999; Rosten and Ramstad 1998). This method applies Green's Theorem in the distance-time domain and integrates the predicted seismic energy along a surface or volume based upon the sensitivity of reflections to 2- and 3-D structure. Its strengths derive from its flexibility, with changes in topography, line geometry, and pre-stack migration possible (Margrave and Lamoureux 2019, Zhu and Lines 1998). Kirchhoff migration has proved a viable tool in recovering information from irregular boundaries (Shearer 2009), of which void spaces are a subsect.

Similar to Kirchhoff migration, the RTM method is calculated within the distance-time domain (Du et al. 2006). Relative to the Kirchhoff method of migration, the RTM method can be more accurate in structure recovery when both vertical and lateral velocity changes are present (Zhu and Lines 1998, Du et al. 2006) (e.g., a lava tube). RTM utilizes a forward-modeled wavefield based upon an input velocity model and a migration derived through a wavefield created in reverse-time and seeks the most accurate “image” that matches these two wavefields as the solution.

Our third method of migration, PSPI, is calculated in the frequency-wavenumber domain (Du et al. 2006). This approach applies Fourier transforms in space and time to the data, an approach that nominally alleviates dispersion effects and is effective for pre-stack and 3D migration techniques (Stolt 1978). The PSPI method can present inaccuracies when considering lateral homogeneities in velocity (i.e., lava tubes). Numerical solutions of the partial differential equations that define the PSPI method, such as the fifteen-degree equation, have been applied to extend PSPI’s migration capacity to inhomogeneous media (Gazdag 1978), lending proof of concept to its efficacy at void space reconstruction.

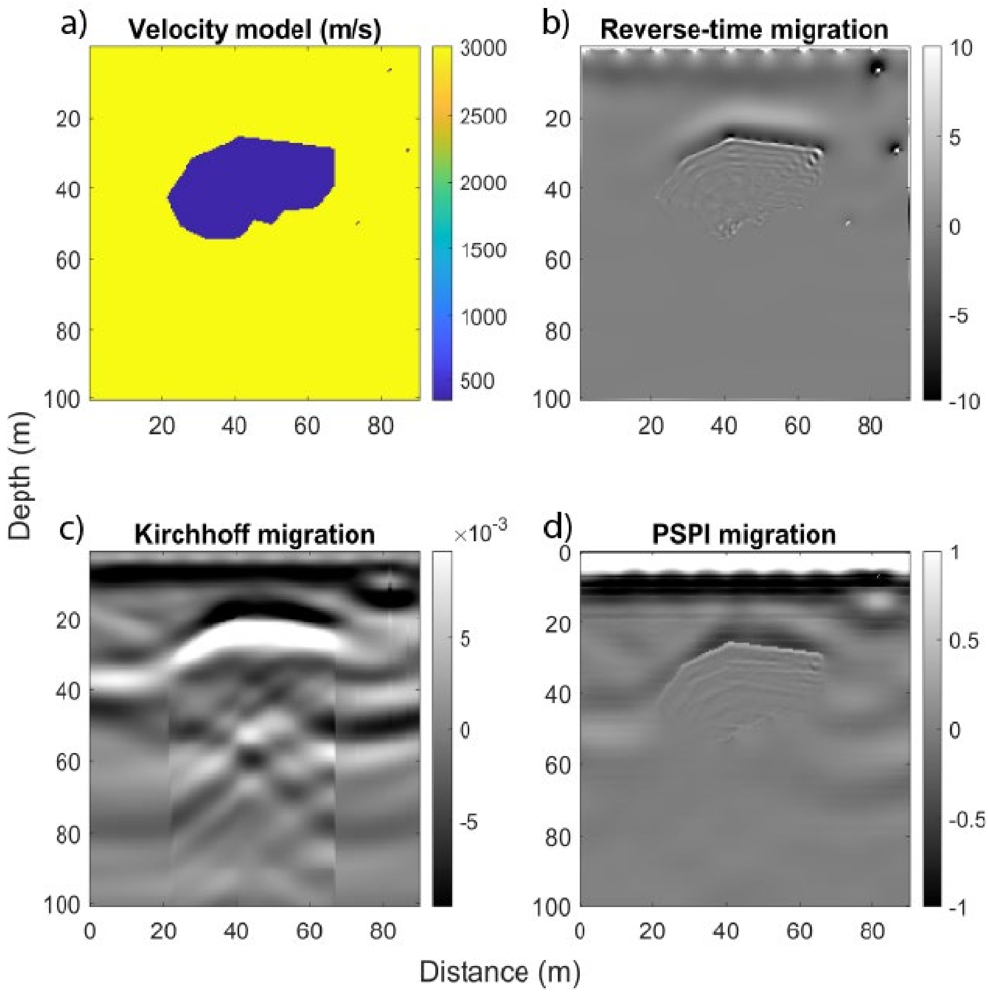

Figure 12. Examples of migration results for a void model. The a) input velocity model, with P-wave velocity indicated in the scale, and our b) RTM reconstruction, c) Kirchhoff migration reconstruction, and d) PSPI migration reconstruction for the 46 m diameter, 25 m ceiling depth Skull Cave model with 0.5 m geophone spacing. Input parameters for the migrations are described in Section 2.5. Scale bars for the migrations are amplitude as a measure of the displacement, with increased contrast to highlight void signatures.

2.7 Comparison of Migration Methods

In order to determine the effectiveness of each migration method's ability to reconstruct the input lava tube, we first pick the seismic wave first arrivals that we interpret to be attributed to the lava tube. This provides a way to compare the accuracy of the reconstructions for our interpretation of the only subsurface structure that the wavefield interacted with. We resample the input RTM, PSPI, and Kirchhoff migrations to a uniform matrix size shared with the input velocity model (e.g., 181 by 201 for 0.5 m geophone spacing and 45 by 50 for 2.0 m geophone spacing). This is necessary to run the FDM and CREWES migration codes as the resolution, or matrix size, of the migration images must match the input velocity model and synthetic seismic wavefield resolution. A velocity model outline of the tube ceiling is constructed from the input model (e.g., Fig. 10, left) by finding the boundary between basalt and air velocity and serves as the ground-truth to compare migration results against. To exclude outlier peak amplitudes or numerical noise of high amplitude that is not collocated with an expected lava tube signal, we calculate histograms of the migration amplitude values, or amplitudes, of the matrices attributed to each migration method and exclude values with a probability density lower than 0.0001, which we deem sufficiently low. This methodology defines how we automate picking of the wave peaks. We then normalize the migrated images to their maximum values, which are defined as the threshold values. The first arrivals are defined as the first peak amplitudes within a depth range surrounding the lava tube boundary above 20% of the respective threshold value for RTM and PSPI; this is analogous to the first arrivals in seismic field data demonstrating the largest amplitude signal, followed by smaller amplitude multiples. The Kirchhoff migration image values do not contain stark outliers, and we do not threshold it beyond the exclusion of outliers and normalization.

2.7.1 Depth Analysis

The first variable attributed to each method is the depth inaccuracy as the root mean square error (RMSE) between known depth profile of the lava tube's ceiling and the outline obtained through the first arrival picks, itself a result of our assumption of a velocity model to migrate them to depth. The RMSE is defined as the standard deviation of the residuals, where the residuals are the difference between the expected values (model ceiling depth vector) and the actual values (migration reconstructed ceiling depth vector). This is illustrated in Fig. 13, where the RTM, PSPI, and Kirchhoff methods, respectively, have increasing depth inaccuracies.

a)

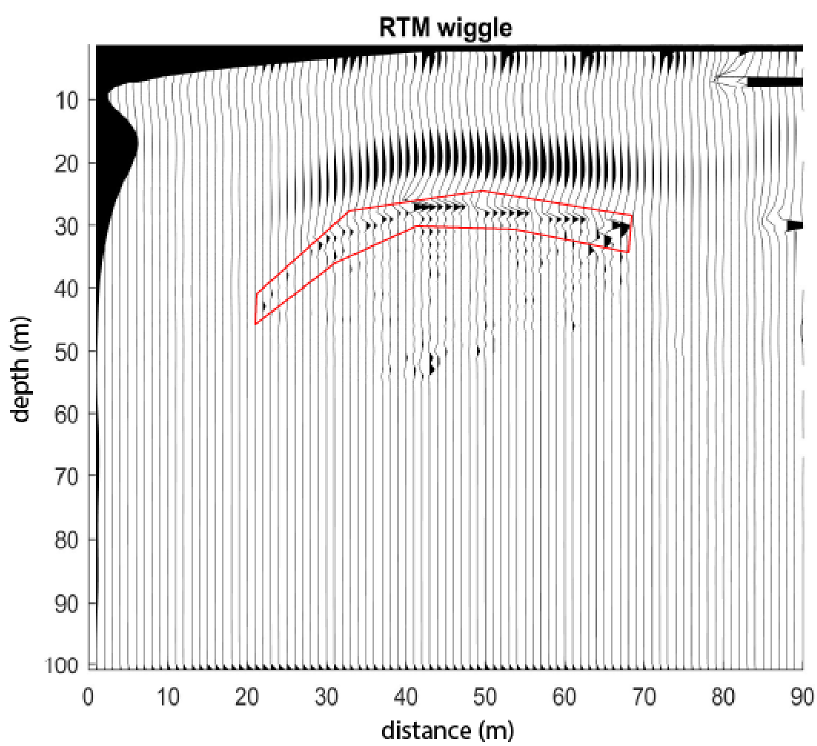

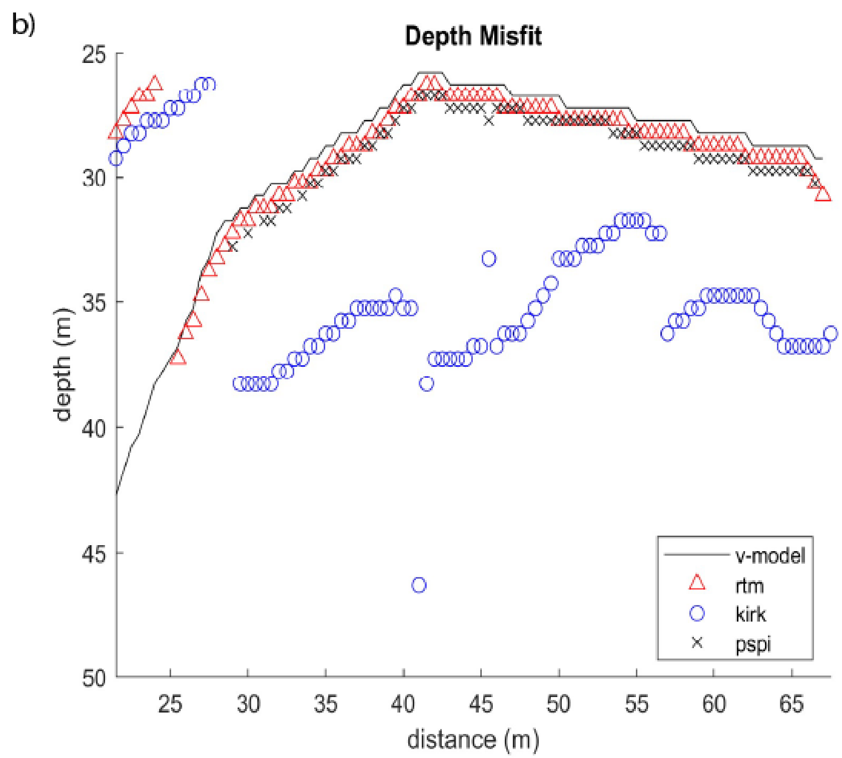

Figure 13. a) Example of an RTM result showing the seismic waveform for the migration at each geophone. The region where we pick the depth to the ceiling of the lava tube is highlighted in red. b) First arrival picks at each receiver position for determining the misfit in depth between each migration method (RTM, Kirchhoff, PSPI) reconstruction of a tube and the input tube model (v-model). This example is for the 46 m diameter, 25 m ceiling depth Skull Cave model with 0.5 m geophone spacing.

2.7.2 Width Analysis

We estimate the width inaccuracy as the sum of the misfit between the expected lateral extent of the lava tube's ceiling and that obtained from the starting point and the ending point where we detect first arrival picks (Fig. 14). For every receiver spacing (e.g., 0.5 m, 1.0 m, 2.0 m) within the expected lava tube range where there exists a pick, regardless of depth inaccuracy, a value of 0 is assigned; for every index within the expected range where there is no pick, a value of 1 is assigned. The reverse applies outside of the expected lava tube lateral extent, with each pick assigned a value of 1, and regions without a pick assigned a value of 0. The total values are then adjusted to reflect the variances in grid size by normalizing them to the 1.0 m estimation, thus the 0.5 m grid-spacing width misfit values are divided in half and the 2.0 m grid-spacing width misfit values are scaled by two; this process renormalizes each width inaccuracy to be comparable to the 1.0 m scenario. The picking process is illustrated in Fig. 14, where we note that the PSPI, RTM, and Kirchhoff methods, respectively, have increasing width inaccuracies.

a)

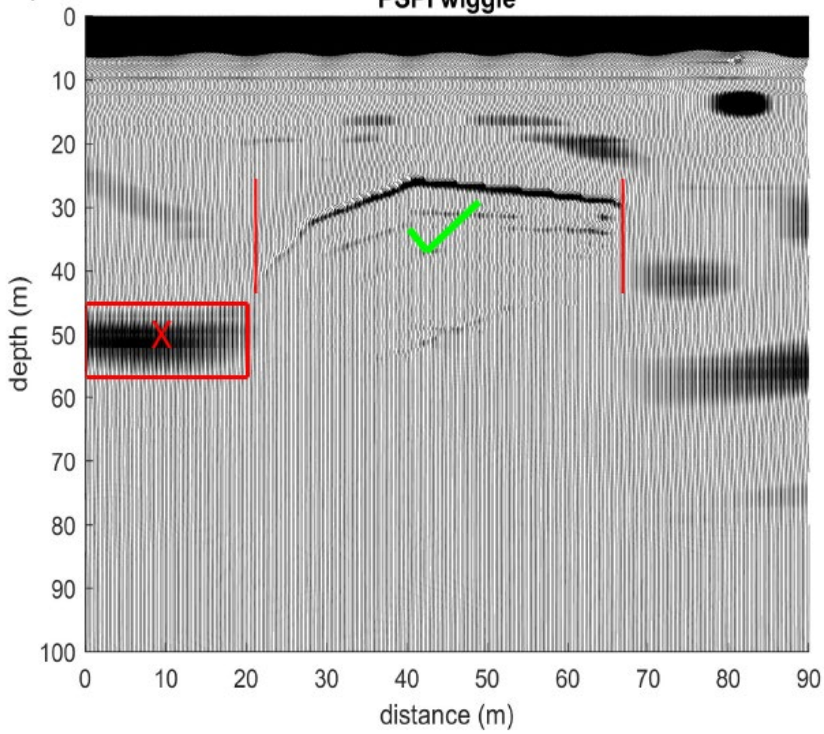
PSPI wiggle
depth (m)
distance (m)

b)

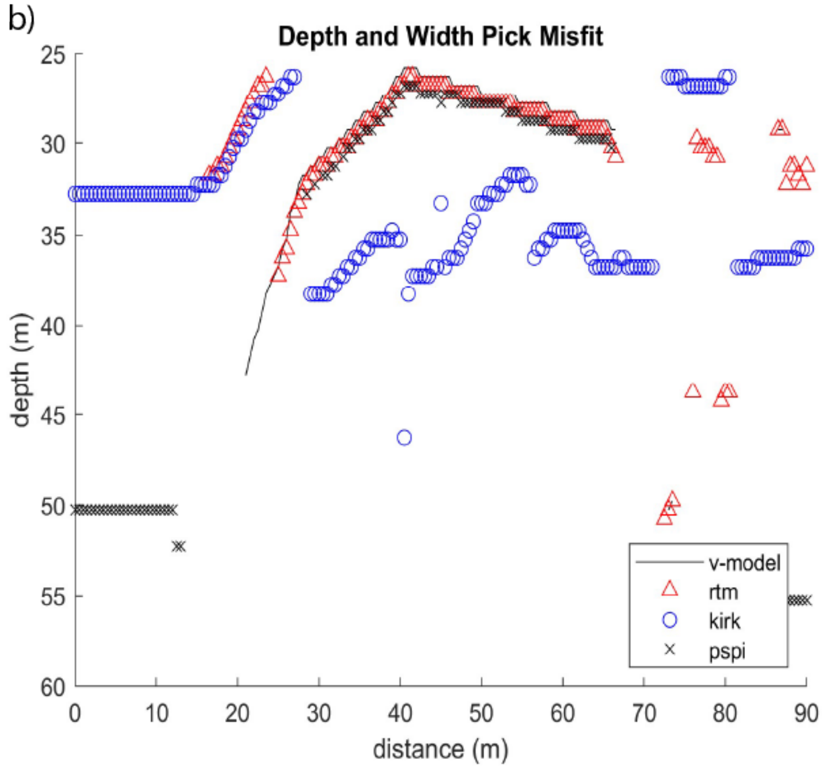
Depth and Width Pick Misfit
depth (m)
distance (m)
v-model
rtm
kirk
pspi

Figure 14. a) Example of a PSPI result showing the seismic waveform for the migration below each geophone. The region where we pick the width of the lava tube is between the two vertical red lines with the green checkmark. The region where we denote failure to resolve tube width from is highlighted as the red box. Picks within the vertical lines do not add to the misfit, while picks within the red box add to the misfit. b) First arrival picks at each receiver for determining the total misfit in depth and width between each migration method (RTM, Kirchhoff, PSPI) and the input velocity model (v-model), measured in meters. This example is for the 46 m diameter, 25 m ceiling depth Skull Cave model with 0.5 m geophone spacing.

2.7.3 Image Similarity

We further estimate each migration method's reconstruction of the input model space in terms of the similarity between the output and input images, or matrices (Fig. 15). This similarity is calculated utilizing the MATLAB structural similarity matrix (SSIM) function (Bakurov et al. 2022, Nilsson and Akenine-Möller 2020, Wang et al. 2003). The SSIM is defined in Equation 3 from Zhou et al. (2004), where μx is the local mean of image x, μy is the local mean of image y, σx is the standard deviation of image x, σy is the standard deviation of image y, σxy is the cross-correlation between x and y, and C1 and C2 are constants (Eq. 3). We determine the similarity between matrices as a unitless number, with 1 the highest value for a perfect fit. SSIM has been utilized in determining the efficiency of seismic denoising (Almadani et al. 2021), in evaluating the best method of reducing full-waveform inversion's computation costs (Lee et al. 2023), and in validating seismic migration technique development (Castañeda Marin 2016). As such, SSIM offers a recursive, high-fidelity method of measuring how well an output seismic reconstruction from migration fits the expected model.

$$SSIM(x, y) = \frac{(2\mu_x\mu_y + C_1)(2\sigma_{xy} + C_2)}{(\mu_x^2 + \mu_y^2 + C_1)(\sigma_x^2 + \sigma_y^2 + C_2)} \tag{3}$$

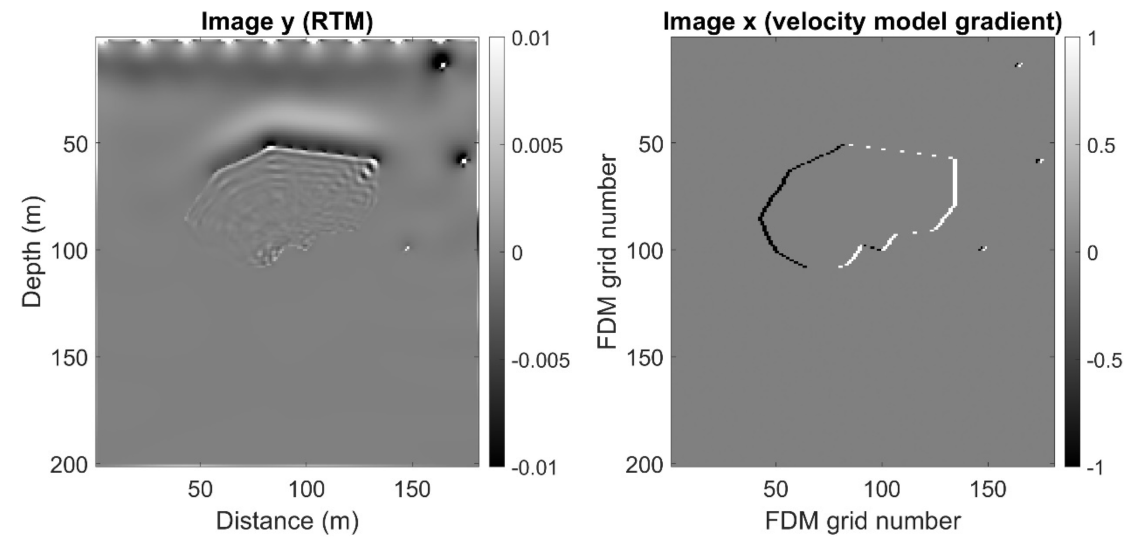

Figure 15. Example (left) image y from the reverse-time migration reconstruction of the input lava tube and (right) image x of the horizontal gradient of the velocity model that is used to evaluate the SSIM (Eq. 3). Future work would use a vertical gradient of the velocity field for a more accurate comparison.

Chapter 3: Results

We apply three types of migration to the two terrestrial analog lava tube scenarios, Skull Cave and Lava River Cave. We investigate the dependence of each migration method on the assumed background model for a given lava tube, as well as the dependence of each migration method on the seismic line geophone spacing, lava tube depth, and lava tube size. Our goal is to understand how these variables have separate impacts on the migration methods' ability to reconstruct the input tube model. A summary table of all of the results of these diagnostic measures are presented in Appendix B, Table B1.

3.1 Migration Method Differences: Homogeneous Velocity Model

Our first validation step was to evaluate the ability of each migration method to reconstruct a signal without a detailed (containing a lava tube) velocity model input. We expect that in most natural scenarios a seismic investigation will lack an accurate background model, although in principle one could be obtained from refraction data or LiDAR constraints on tube geometry. In this experiment the migration code was given the synthetic data computed using the background velocity model for the 46 m diameter, 25 m ceiling depth Skull Cave model (Fig. 12a), and we assume a homogeneous basalt-only (3 km/s) background velocity model for migration. Each method returns a migrated image that contains a tube-like structure, validating that the methods can indeed recover lava tube structure without *a priori* knowledge of their depth, shape, and interior velocity (Fig. 16). The respective RMSEs from our automated picking of the arrivals from the top of the tube for RTM, Kirchhoff, and PSPI are: 7.06 m, 10.91 m, and 7.69 m. The respective width inaccuracies for this scenario for RTM, Kirchhoff, and PSPI are: 2 m, 22 m, and 20.5 m. RTM is the most accurate, with Kirchhoff and PSPI an order of magnitude higher in uncertainty over RTM.

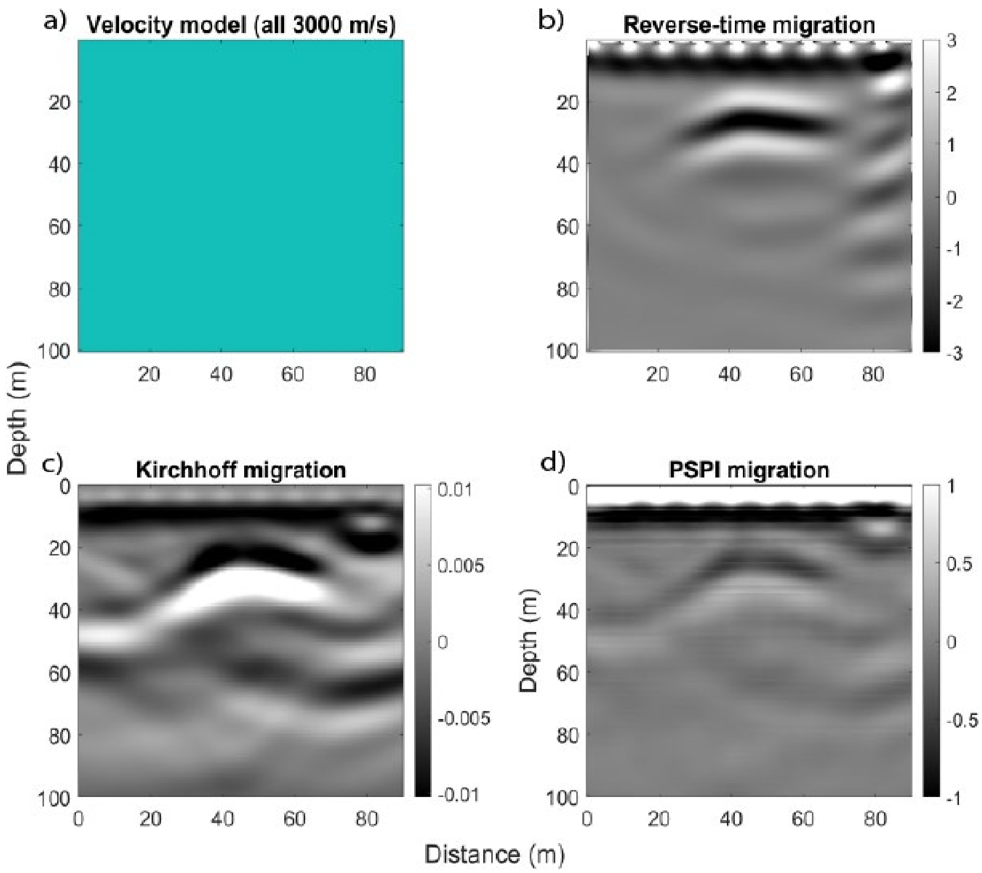

Figure 16. Homogeneous migration model experiment. a) The migration velocity model is purely a basaltic background velocity (3 km/s). Results for b) RTM, c) Kirchhoff migration, and d) PSPI. For this model, the tube was 46 m diameter, 25 m ceiling depth, using the Skull Cave shape model with 0.5 m geophone spacing experimental design. Scale bars represent relative amplitude of the migrated seismic waveform.

3.2 Migration Reconstructions

3.2.1 Skull Cave

Here we examine the migrations for each of the fifty-four Skull Cave geometry, depth, and geophone spacing seismic simulations were created using RTM, PSPI, and Kirchhoff migration. The results for RTM (Fig. 17), PSPI migration (Fig. 18), and 2D Kirchhoff migration (Fig. 19), each qualitatively show differences in the technique's reconstruction for the 0.5 m geophone spacing models. From Fig. 17, the RTM results show a well-defined lava tube roof across all nine model spaces, with some low-frequency numerical noise content that does not saturate the signal. The results of PSPI migration similarly define the lava tube ceiling and lateral extent; however, they present more low-frequency noise, artificial and a numerical artifact of FDM simulation, surrounding the void space. The Kirchhoff migration presents the greatest amount of low-frequency noise and the least-defined lava tube ceiling and lateral extent, from a visual perspective. For the Kirchhoff results, the lava tubes with smaller diameter migrate to a focused area, or a point, while the larger diameter lava tubes seismic waveforms migrate in depth to wide arcs, with high amplitude trails extending across the migration space.

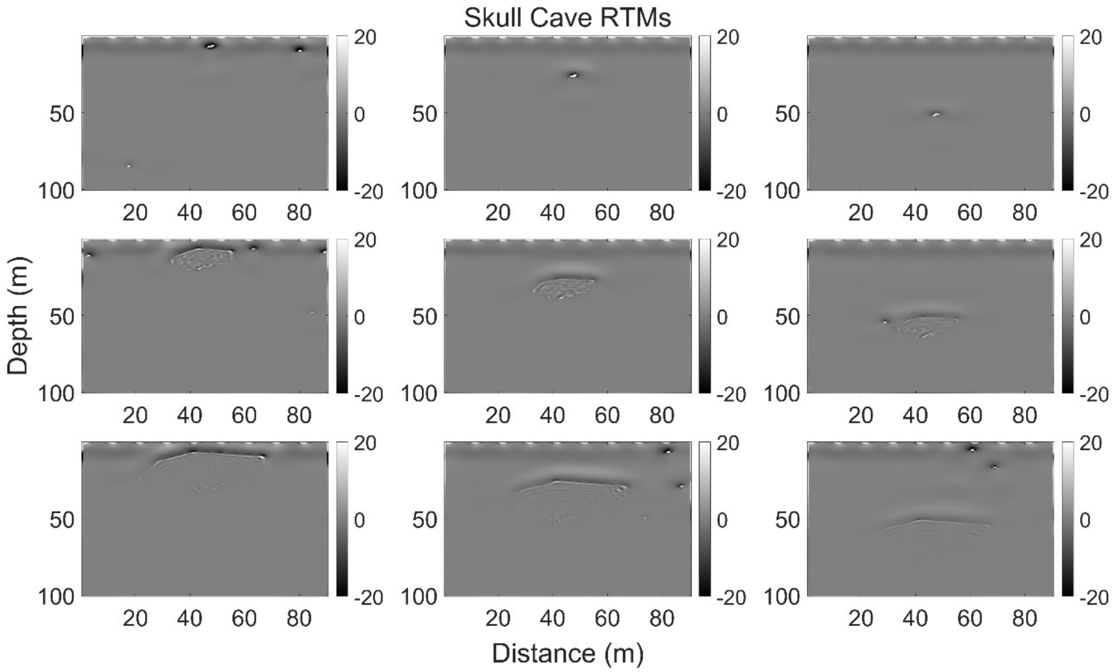

Figure 17. Results for RTM for each of the nine Skull Cave model spaces for a 0.5 m geophone spacing. Scale bars represent relative amplitude of the migrated seismic waveform. The background model space is the same as in Figure 5.

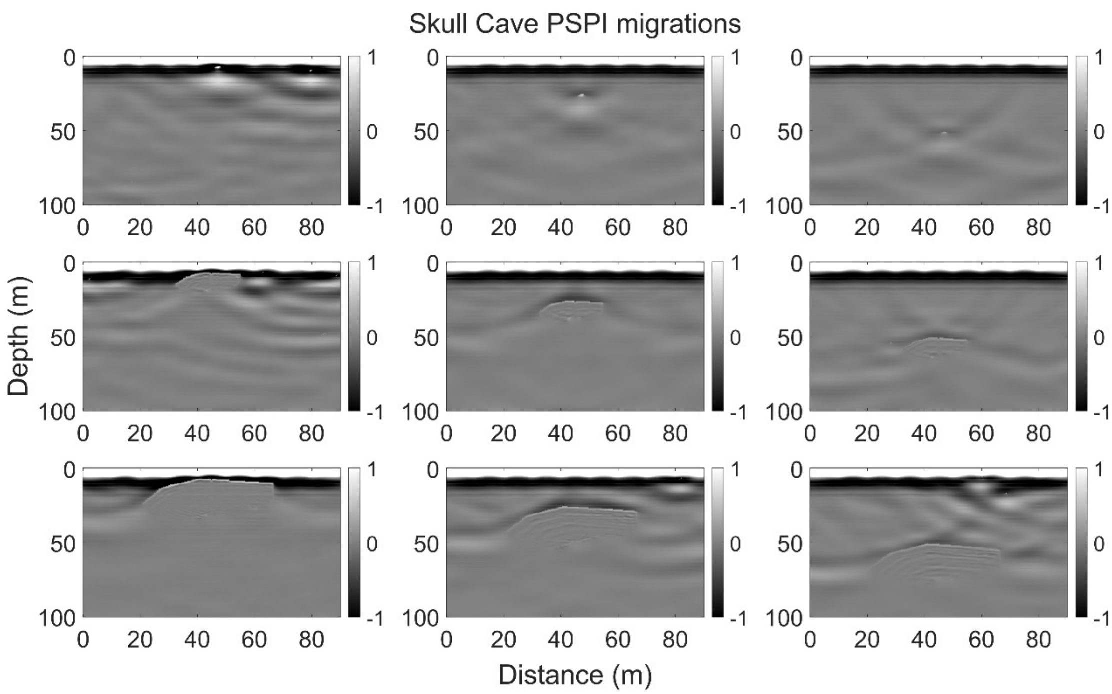

Figure 18. Results for PSPI migrations for each of the nine Skull Cave model spaces for a 0.5 m geophone spacing. Scale bars represent relative amplitude of the migrated seismic waveform. The background model space is the same as in Figure 5.

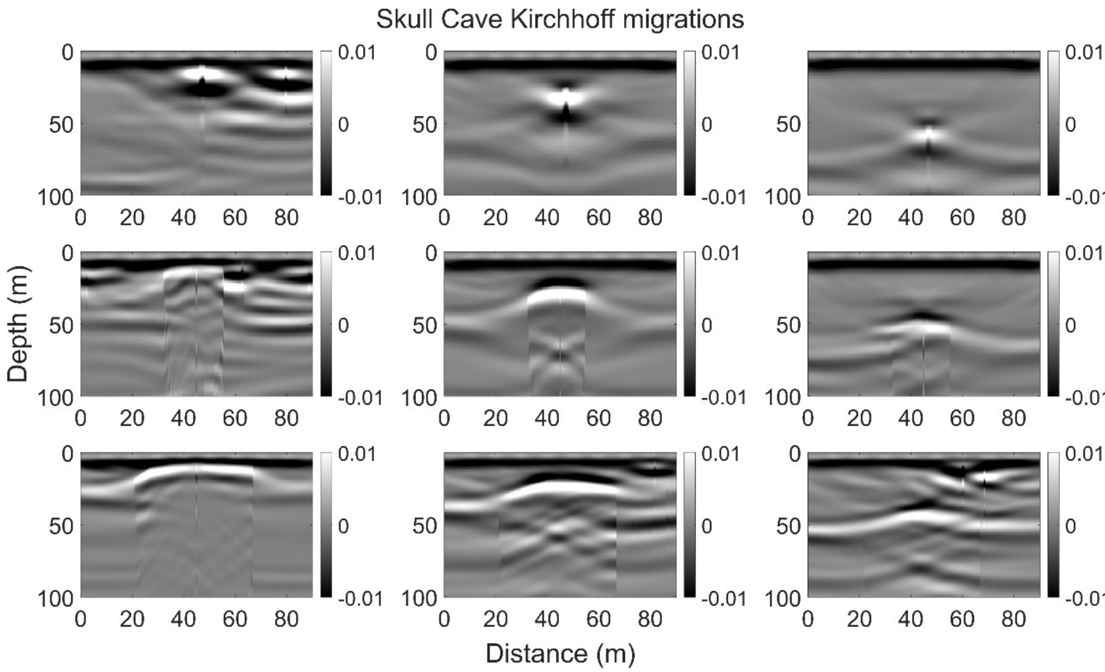

Figure 19. Results for Kirchhoff migrations for each of the nine Skull Cave model spaces for a 0.5 m geophone spacing. Scale bars represent relative amplitude of the migrated seismic waveform. The background model space is the same as in Figure 5.

3.2.2 Lava River Cave

The migration results for the fifty-four Lava River Cave simulations are similar to those presented in Section 3.1.1 for Skull Cave, demonstrating that the primary differences between methods are a result of depth and width rather than exact tube shape. Qualitatively, RTM results (Fig. 20) show the lava tube ceiling and lateral extent, with a relative amplitude on the order of 100 times that of the surrounding material. PSPI migration (Fig. 21) incorporates more numerical, low-frequency noise surrounding the lava tube geometry, and Kirchhoff migration (Fig. 22) shows the highest degree of noise and numerical artifacts, or noise resultant from the construction of each mesh space and FDM simulation. With the caveat of imposing background velocity model for the highest fidelity results, RTM presents the best migration qualitatively.

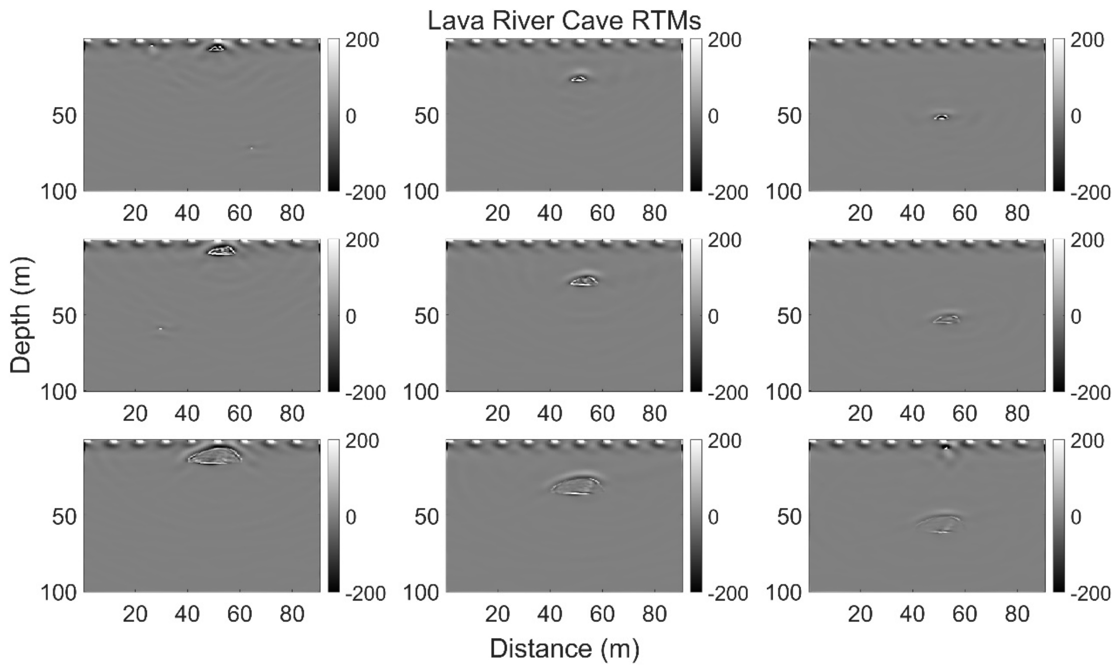

Figure 20. Results for RTM for each of the nine Lava River Cave model spaces for a 0.5 m geophone spacing. Scale bars represent relative amplitude of the migrated seismic waveform. The background model space is the same as in Figure 7.

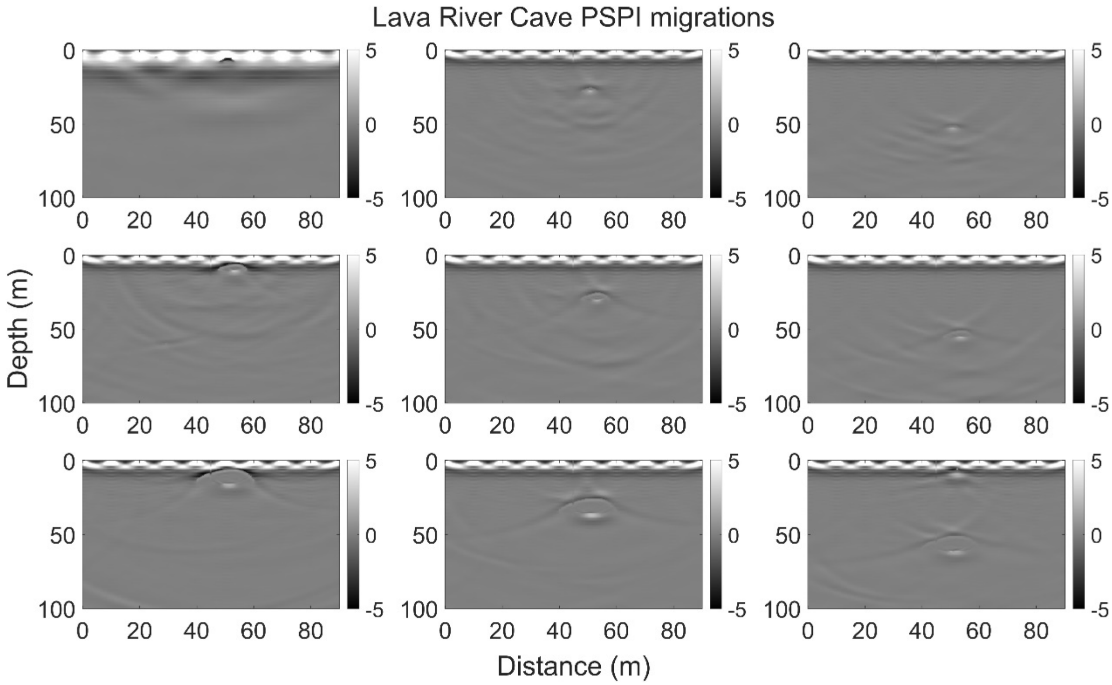

Figure 21. Results for PSPI migrations for each of the nine Lava River Cave model spaces for a 0.5 m geophone spacing. Scale bars represent relative amplitude of the migrated seismic waveform. The background model space is the same as in Figure 7.

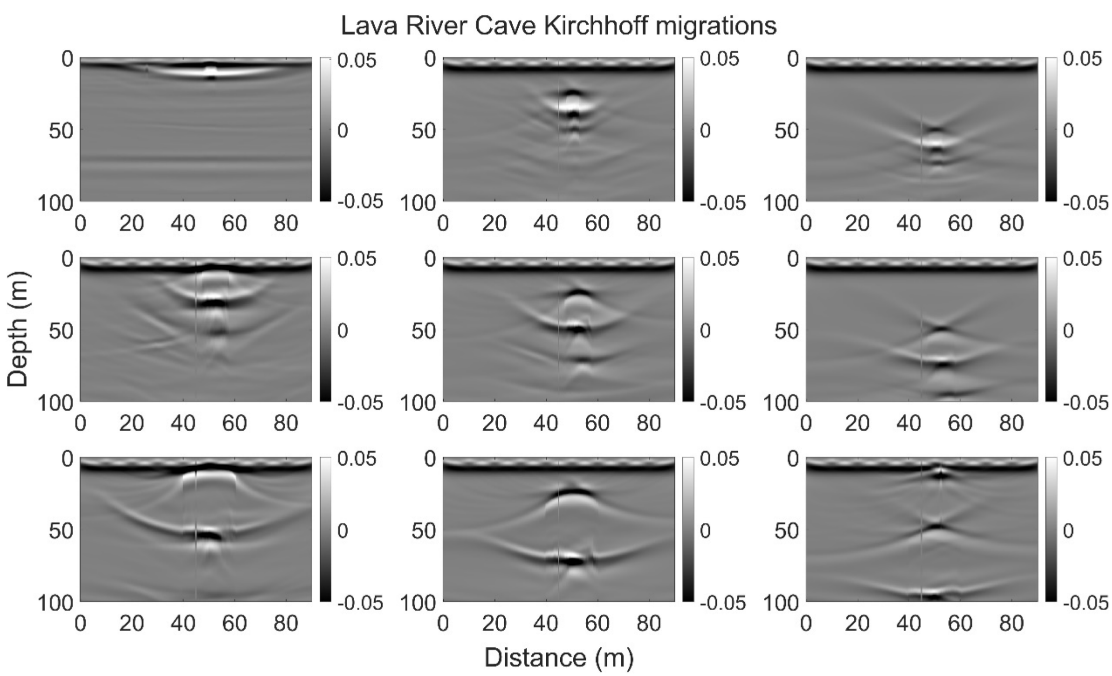

Figure 22. Results for Kirchhoff migrations for each of the nine Lava River Cave model spaces for a 0.5 m geophone spacing. Scale bars represent relative amplitude of the migrated seismic waveform. The background model space is the same as in Figure 7.

3.3 Effect of Receiver Spacing

3.3.1 Skull Cave

The first parameter we evaluated was the efficiency of each method at reconstructing the lava tube image based on the spacing between geophones along the surface. From a qualitative standpoint, the clarity of the output reconstruction decreases with increasing receiver spacing, as seen in the comparison between 0.5 m spacing (Fig. 23a), 1.0 m spacing (Fig. 23b), and 2.0 m spacing (Fig. 23c) for the Skull Cave model with 46 m diameter and 25 m ceiling depth.

We quantitatively determine these differences through picking the arrivals (Fig. 24-25). The ability of each method to determine ceiling depth and lava tube width varies; some models show increased misfit as receiver spacing increases. However, there is an increase in both depth misfit and width misfit as geophone spacing increases from 0.5 m to 1.0 m to 2.0 m. Overall, the RTM method presents the lowest depth (Fig. 24) misfits and width (Fig. 25) misfits, followed by PSPI migration, then Kirchhoff migration.

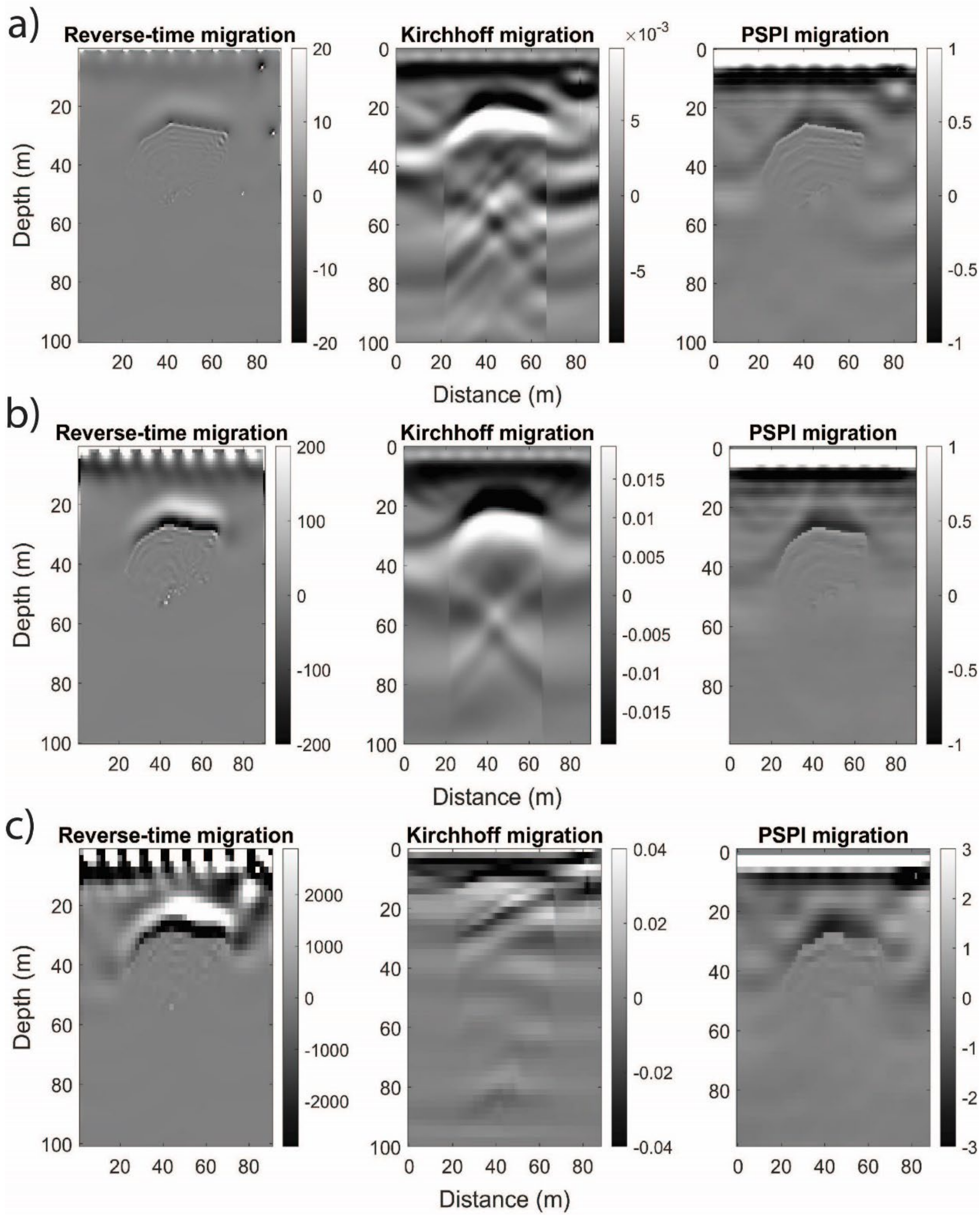

Figure 23. Results of migrations of the Skull Cave 46 m diameter, 25 m ceiling depth model for geophone spacings of a) 0.5 m, b) 1.0 m, and c) 2.0 m. Scale bars represent relative amplitude of the migrated seismic waveform.

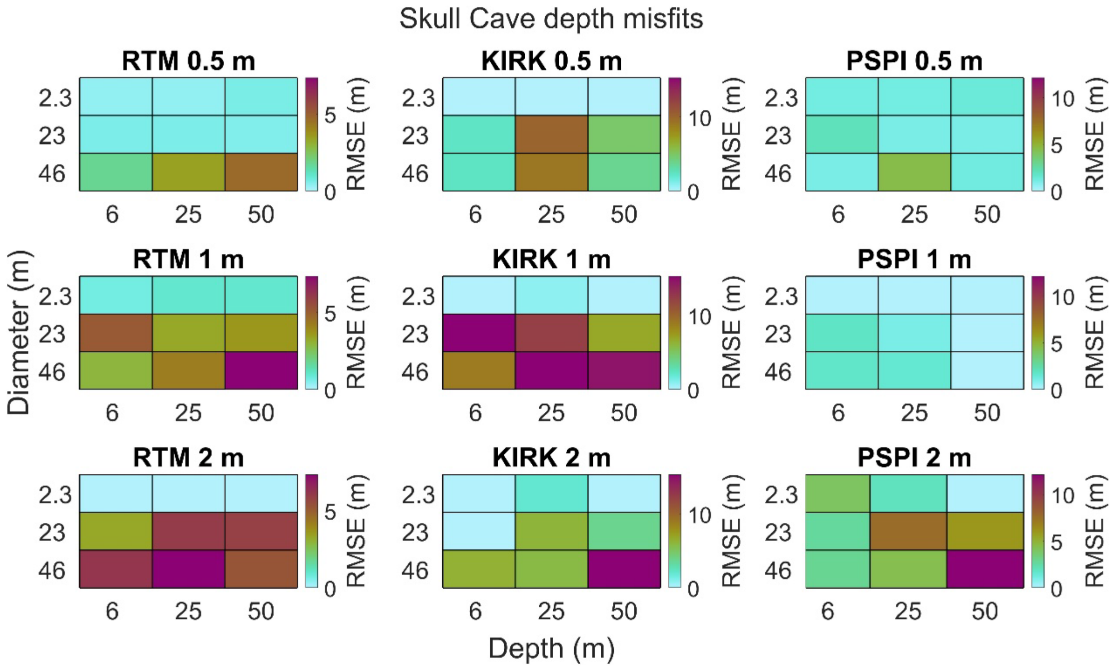

Figure 24. Comparison of reconstruction depth misfit for each Skull Cave model space of varying geophone spacing. There are three unique scalebars, with each respective migration techniques having a consistent scale across geophone spacings. The sets of nine color-scaled boxes attributed to each migration method follow the depth and diameter scheme of Fig. 5.

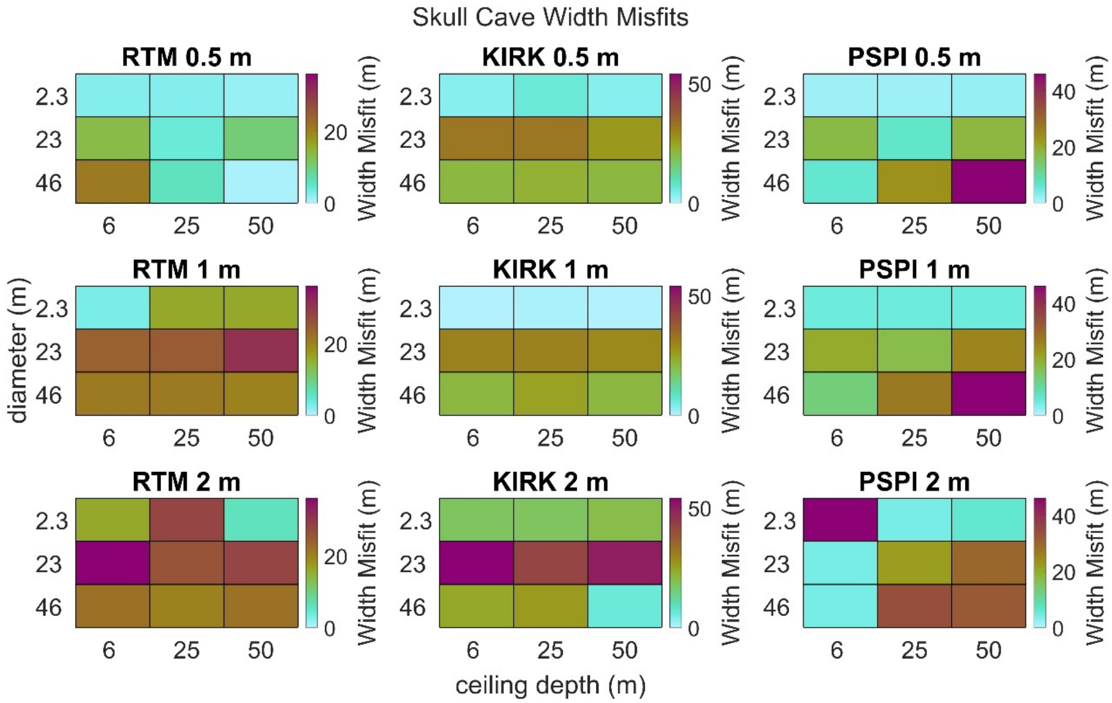

Figure 25. Comparison of reconstruction width misfit for each Skull Cave model space of varying geophone spacing. There are three unique scalebars, with each respective migration techniques having a consistent scale across geophone spacings. The sets of nine color-scaled boxes attributed to each migration method follow the depth and diameter scheme of Fig. 5.

3.3.2 Lava River Cave

Each method presents increasingly inaccurate depth (Fig. 26) and width (Fig. 27) reconstructions with increasing receiver spacing except for the singular case of the Lava River Cave 1.0 m Kirchhoff migrations. This implies that lava tube depth reconstruction decreases with increasing geophone spacing. Based on our results, for surveys that need a one to three meter accuracy in migration of the ceiling depth and lava tube width, denser geophone lines are required.

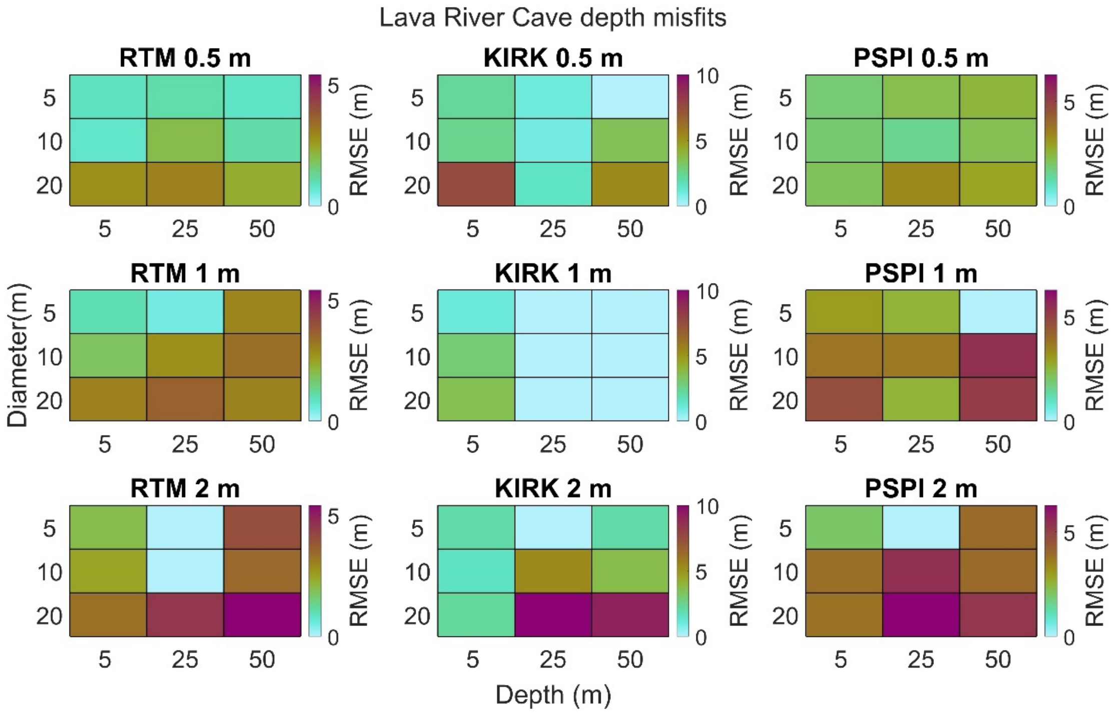

Figure 26. Comparison of reconstruction depth misfit for each Lava River Cave model space of varying geophone spacing. There are three unique scalebars, with each respective migration techniques having a consistent scale across geophone spacings. The sets of nine color-scaled boxes attributed to each migration method follow the depth and diameter scheme of Fig. 7.

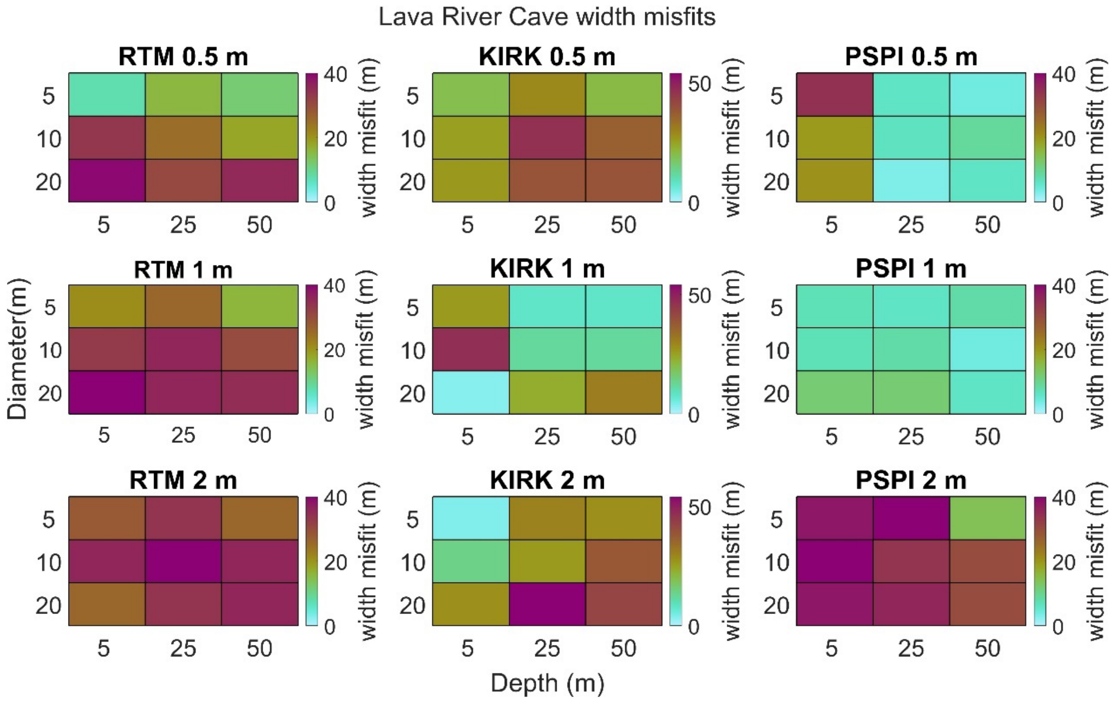

Figure 27. Comparison of reconstruction width misfit for each Lava River Cave model space of varying geophone spacing. There are three unique scalebars, with each respective migration techniques having a consistent scale across geophone spacings. The sets of nine color-scaled boxes attributed to each migration method follow the depth and diameter scheme of Fig. 7.

3.4 Effect of Lava Tube Depth and Size

3.4.1 Skull Cave

The ability of each method to reconstruct the input model was hypothesized to depend on the input model's depth and size. We expected larger, deeper tubes to present the most accurate results; however, for the example of the 0.5 m geophone spacing models, the smaller lava tubes exhibit lower RMSE misfit from the input model, across each size. Proportionally, the meter-scale misfits are more important for these smaller tubes, as 0.5-1 m inaccuracies correspond to 21-43% of the input model diameter (2.3 m), while for the largest lava tubes an inaccuracy of 3-4 m corresponds to 6-8% of the input model diameter (46 m). The relative ability of the method to detect each lava tube's size and depth is shown in Fig. 28 below. For the depth results, there does appear to be a trend of increasing depth misfit with increasing ceiling depth; however, this is less apparent for the width results, which only display less misfit for smaller tubes.

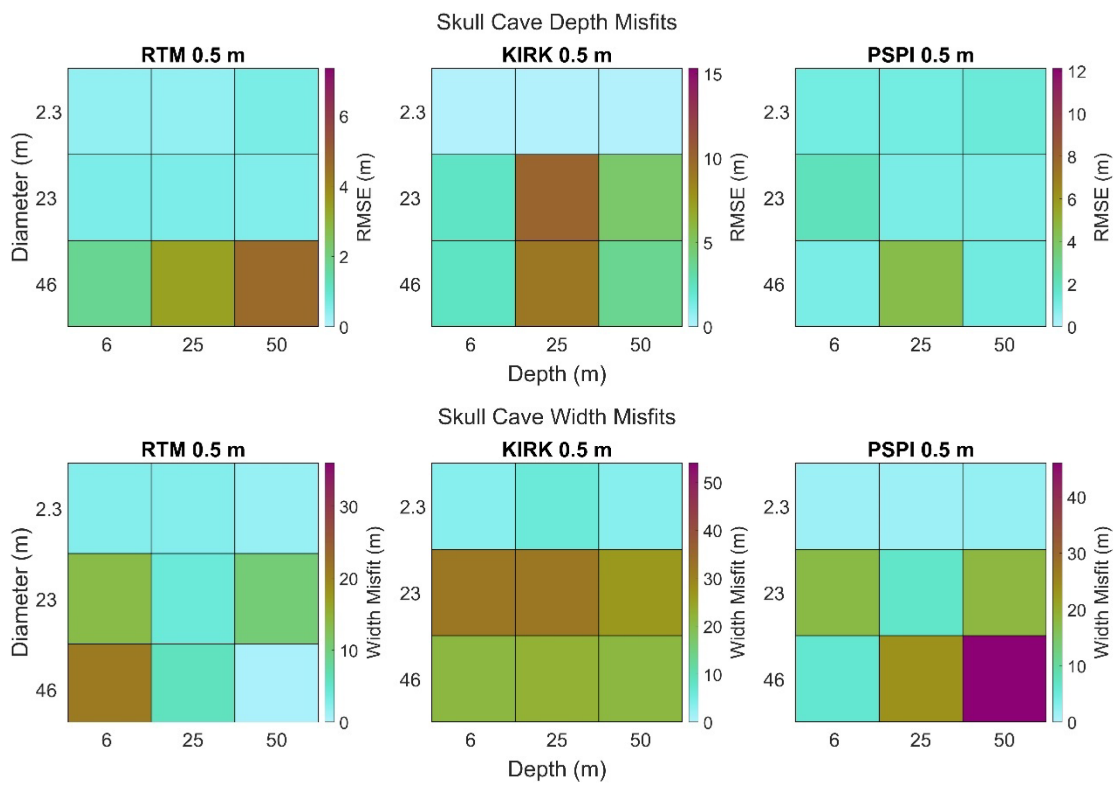

Figure 28. Row one of Figure 24 and row one of Figure 25; these present a comparison of Skull Cave lava tube model reconstruction depth and width misfit for each migration technique as we increase ceiling depth and diameter alone, with no effect of geophone spacing. A high misfit value indicates deviation from the input

model ceiling depth, while a low misfit value indicates a higher fidelity reconstruction.

3.4.2 Lava River Cave

For the case of RTM and Kirchhoff, the resultant migrations present the most accurate depth calculations for the smaller lava tubes at depth, while for PSPI the migrations are the most accurate for mid-sized tubes at depth (Fig. 29). Given that the larger lava tubes span twenty meters and the smaller lava tubes span five meters, a meter-scale error for the latter is proportionally larger. For the largest lava tube, with 20 m diameter, an inaccuracy of 3-6 m is 15-30% of the input model diameter; however, for the smallest lava tube, with 5 m diameter, an inaccuracy of 0.5-2.5 m is 10-50% of the input model diameter. Greater accuracy at depth confirms the idea that deeper lava tubes are more recognizable, as there is more time for reflections to arrive and be distinguished from the low-frequency artificial noise inherent to FDM synthetic simulation and reverberations found in the upper meters.

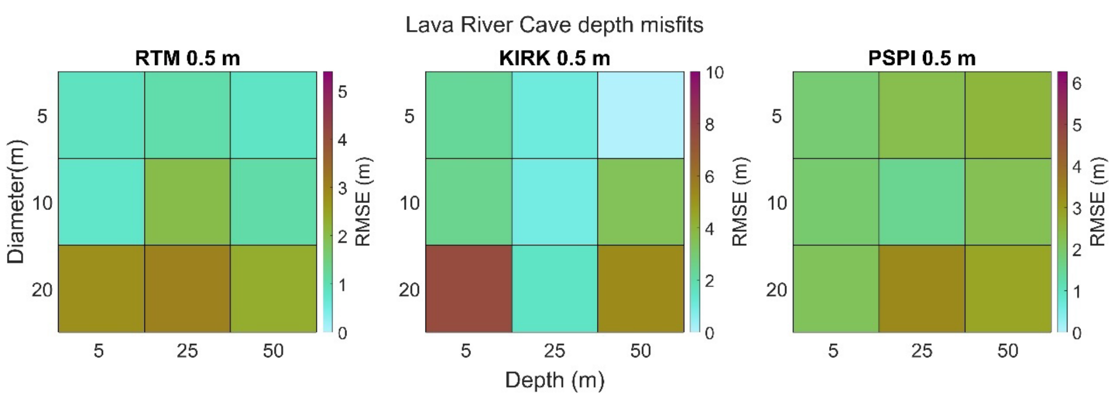

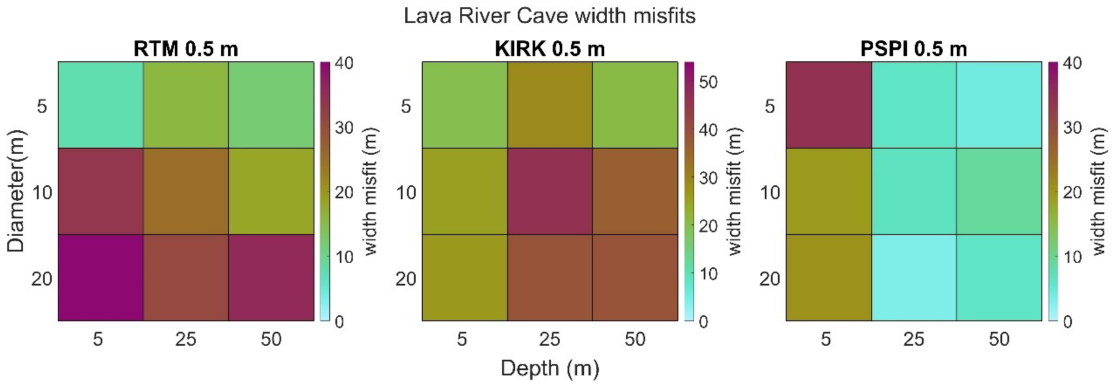

Figure 29. Row one of Figure 26 and row one of Figure 27; these present a comparison of Lava River Cave lava tube model reconstruction depth misfit and width values for each migration technique as we increase ceiling depth and diameter alone, with no effect of geophone spacing. A high misfit value indicates deviation from the input model ceiling depth, while a low misfit value indicates a higher fidelity reconstruction.

3.5 Depth and Width Estimates

We compared the RMSE depth misfit values and width misfit values across all Skull Cave (Fig. 30) and Lava River Cave (Fig. 31) models for each of the three receiver spacings. Each of the three methods demonstrates an increase in both RMSE depth misfit and width misfit as receiver spacing increases, further demonstrating our results in Section 3.3. There appears to be a general effect of decreasing depth and width accuracy with increasing tube ceiling depth, and no effect based on tube diameter. The average RMSE depth misfit values increase with larger geophone spacing for the cases of RTM and PSPI, with Kirchhoff presenting the highest misfit value for 1.0 m spacing; however, the Kirchhoff method presents an increase between the 0.5 m spacing scenario and the 2.0 m spacing one (Table 2). All three methods show an increase in width misfit values with increased geophone spacing (Table 3).

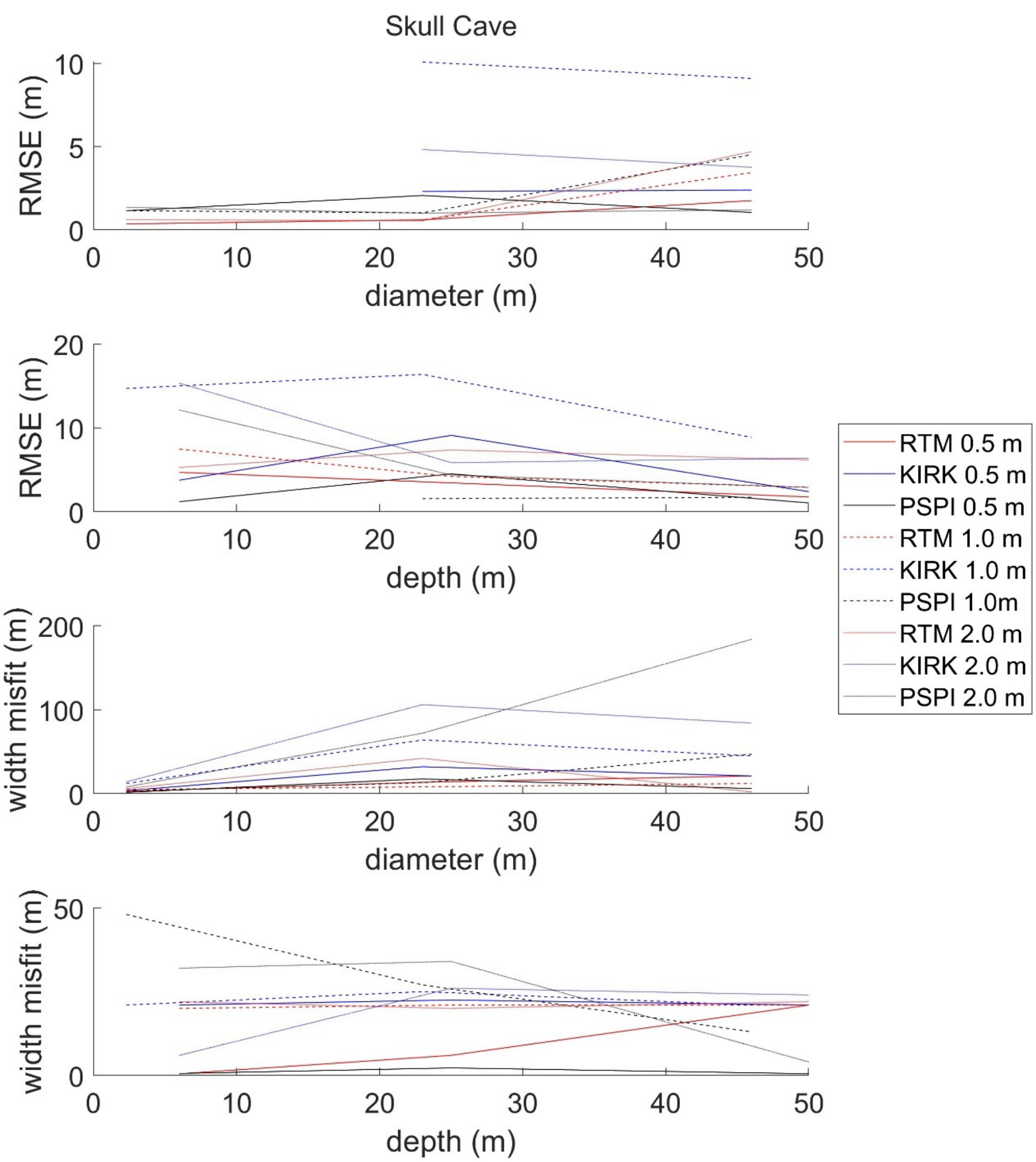

Figure 30. Example RMSE and width misfit values from first arrival picks for each migration technique for the Skull Cave model spaces. For the diameter variable plots, ceiling depth is held at 6 m across all lava tubes. Blank values (e.g., Kirk 1.0 m in plot RMSE (m) vs. diameter (m)) indicate null picks.

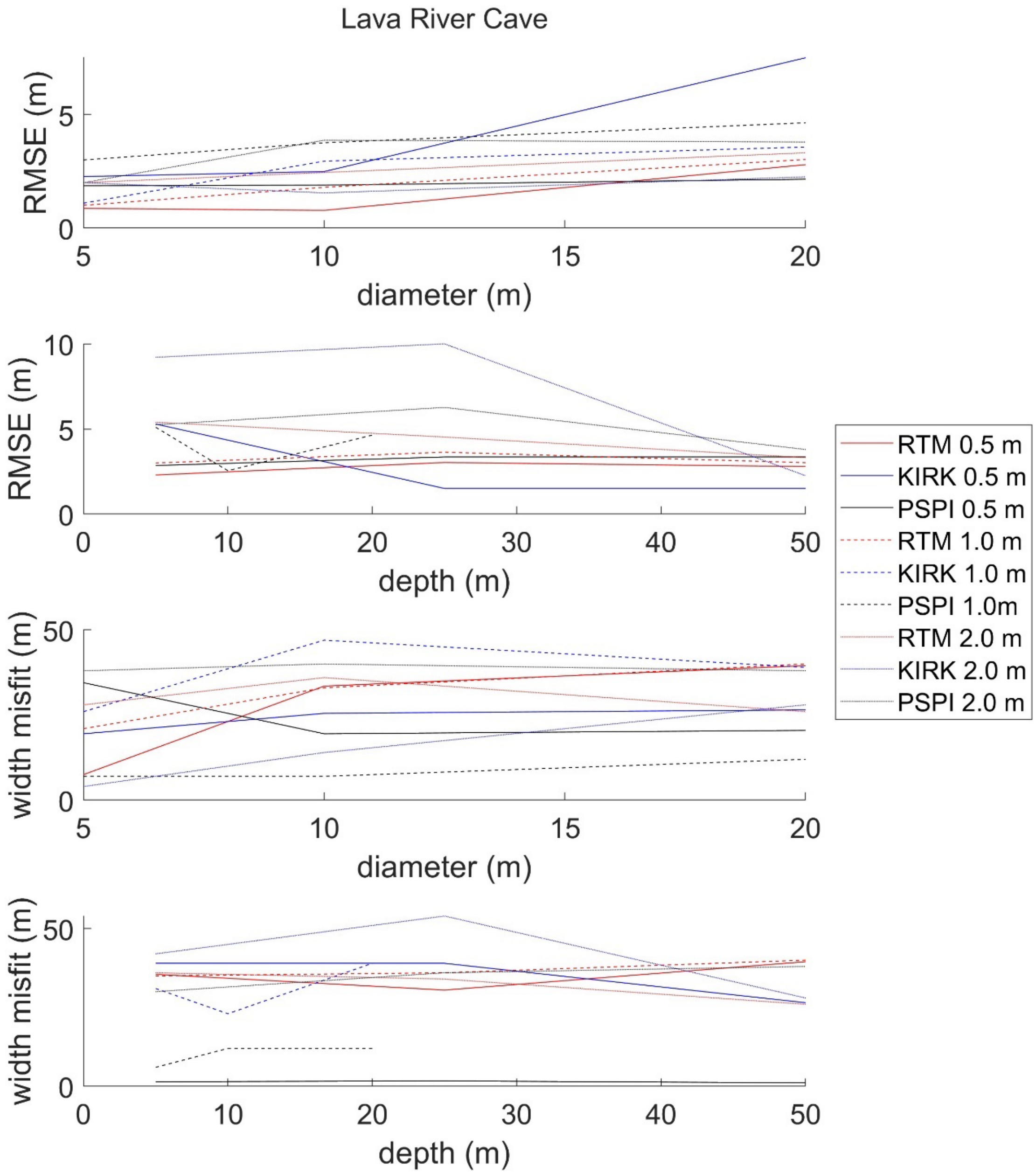

Figure 31. Example RMSE and width misfit values from first arrival picks for the Lava River Cave model spaces. For the diameter variable plots, ceiling depth is held at 5 m across all lava tubes. Blank values indicate null picks.

Migration Type	**0.5 m spacing average RMSE (+/- m)**	**1.0 m spacing average RMSE (+/- m)**	**2.0 m spacing average RMSE (+/- m)**

RTM	1.54	2.86	4.23
Kirchhoff	4.06	8.31	5.39
PSPI	1.95	3.06	4.77

Table 2. Average RMSE depth misfit values across each migration technique and geophone spacing variation, measured in meters.

Migration Type	**0.5 m spacing average width misfit (m)**	**1.0 m spacing average width misfit (m)**	**2.0 m spacing average width misfit (m)**
RTM	7.75	25	55.56
Kirchhoff	25	22.39	29
PSPI	6.43	13.06	53.56

Table 3. Average width misfit values across each migration technique and geophone spacing variation, measured in meters.

RMSE values depend on the input lava tube diameter and depth, where meter-scale depth and width inaccuracies impact the detection of smaller lava tubes more than those of larger lava tubes. This is further supported by the results of scaling each RMSE value by its respective lava tube diameter or converting them into a percentage of the lava tube diameter (Fig. 32a-c). The lava tube RMSEs for the 0.5 m geophone spacing case range from about 1-60%, the 1.0 m geophone spacing case from 1-68%, and the 2.0 m geophone spacing case from 1-173%. There is a trend of increasing RMSE percentage misfit for decreasing lava tube size and decreasing lava tube depth. Once again, the RMSE percentage values are lower for tighter geophone spacing than greater geophone spacing, and for the Skull Cave models when compared to the Lava

River Cave models. Diameter ranges are larger between the Skull Cave models (43.7 m difference) than the Lava River Cave models (15 m difference). RMSE misfit percentages for Lava River Cave have a smaller spread due to the tighter range in diameters. We note that these results may incorporate bias of larger and deeper tubes weighting the results too low; however, we present the results as a comparison study for relative efficiency (Fig. 32, 33).

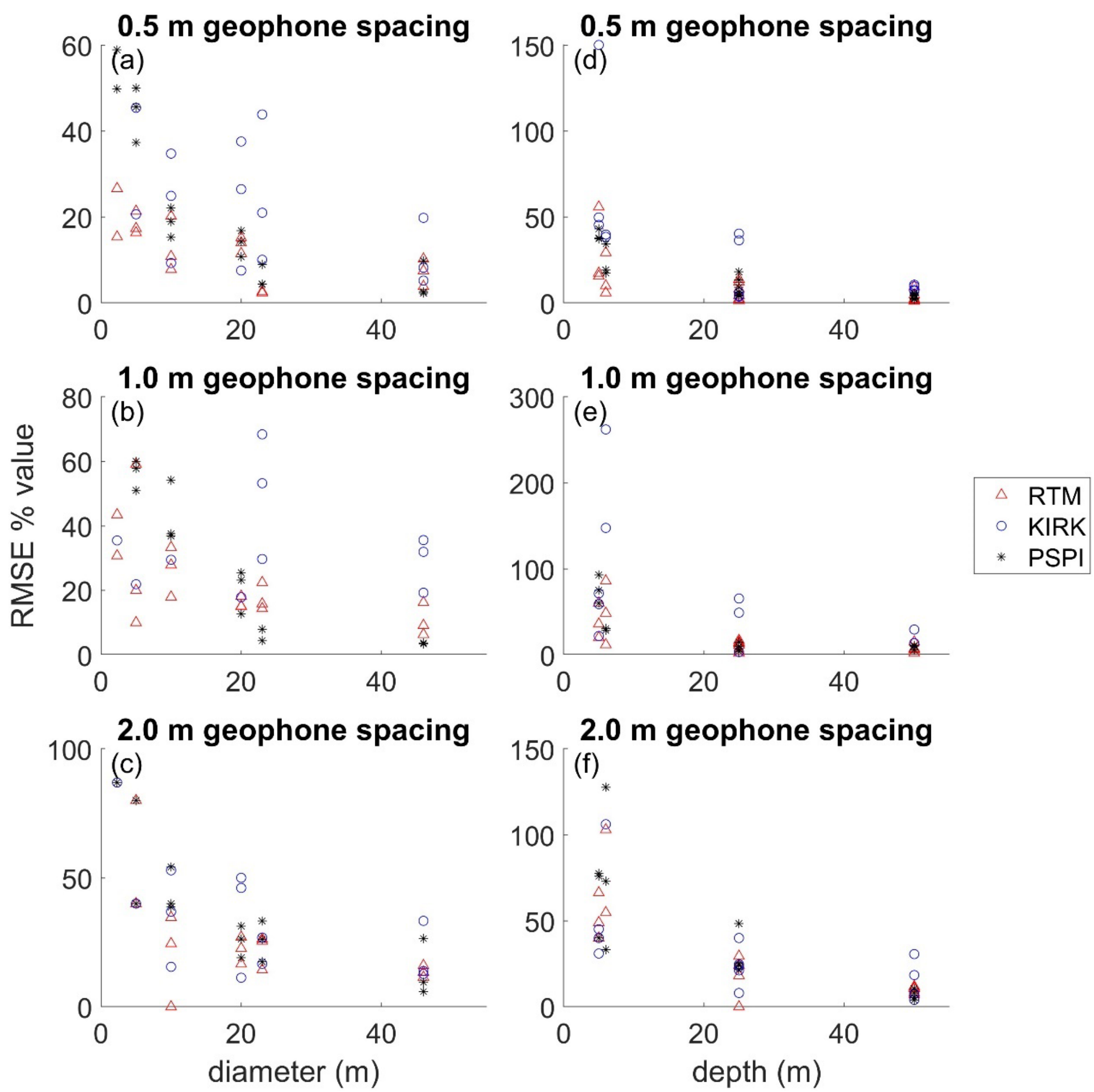

Figure 32. RMSE values for all Skull Cave and Lava River Cave models after normalization to input lava tube diameters, a), b), c), and input lava tube depths, d),

e), f). Lava tubes models with no plotted migration technique have no plotted picks for the migrated data, indicating no lava tube resolution.

Based on Fig. 32, RTM demonstrates the closest depth and width estimates to the input model, followed by PSPI then Kirchhoff. The sharpest increase in inaccuracy is between geophone spacings of 0.5 m and 1.0 m, with the difference between accuracies at 1.0 m and 2.0 m more negligible. This implies that for the case of recovering lava tube width, it is most cost-effective to utilize a 2.0 m grid spacing over 1.0 m (Fig. 32). When considering depth accuracy (Fig. 13), 0.5 m once again shows the highest fidelity ceiling depths, with a sharp decrease in fidelity at 1.0 m and a larger decrease from 1.0 m to 2.0 m. Therefore, we recommend 1.0 m geophone spacing over 2.0 m for a more cost-effective seismic procedure that retains reconstruction accuracy; however, this is dependent on the design objectives of an experiment, where the increase in accuracy of the results for 0.5 m and 1.0 m may outweigh the time constraints.

Width misfit presents similar trends to depth misfit, where larger, deeper tubes consistently have lower percentage differences from the model diameter (Fig. 33a-c). There is likewise an increase in width misfit percentage with increasing geophone spacing. For 0.5 m geophone spacing, the width misfit ranges from 1-580%; for 1.0 m geophone spacing, from 28-1400%; and for 2.0 m geophone spacing, from 9-2000% (note that the 2000% large outlier for 2.0 m grid spacing PSPI is not plotted in Fig. 33f). Across all geophone spacings, the mean width percentage misfits for PSPI, RTM, and Kirchhoff are: 186%, 247%, and 264%. For the case of any lava tube geometry and width, this leave PSPI as the overall most accurate method, with RTM second, and Kirchhoff a close third.

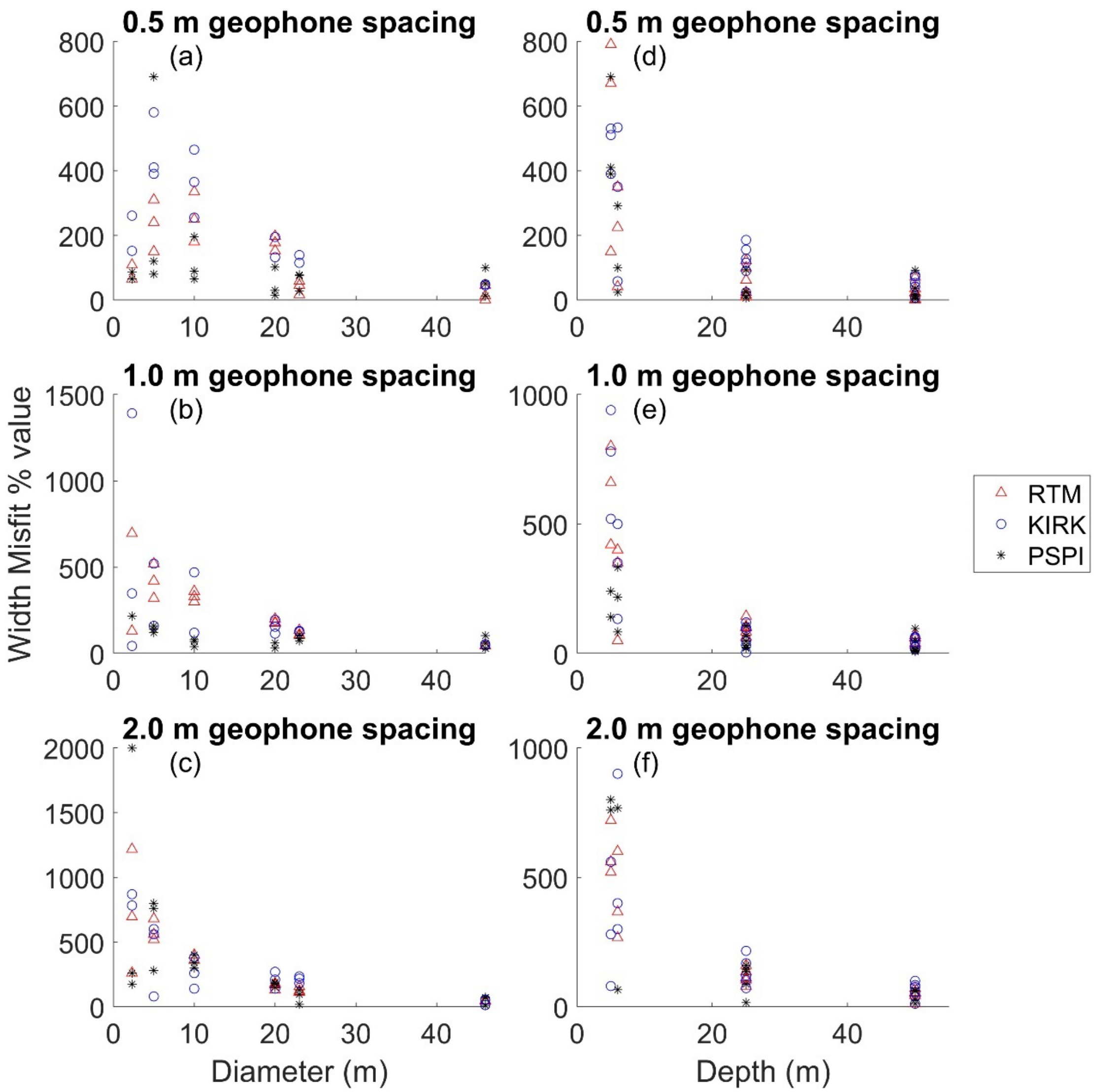

Figure 33. Width misfit (m) values for all Skull Cave and Lava River Cave models after normalization to input lava tube diameters, a), b), c), and input lava tube depths, d), e), f). Lava tubes models with no plotted migration technique have null picks for the migrated data, indicating no lava tube resolution.

3.6 Image Similarity: Migration to Velocity Model

Minimum image similarity values were evaluated for each subset of receiver spacings (Fig. 34, Fig. 35), where a value of one indicates the same image, or matrix, while a value close to zero indicates large misfit between the velocity model and migration. The minimum image similarities, across all eighteen lava tube models, for the 0.5 m, 1.0 m, and 2.0 m scenarios are, respectively, 0.044, 0.078, and 0.006. These correspond to the minimum value for Kirchhoff migration for 0.5 m and 1.0 m, and the minimum value for PSPI migration for 2.0 m. The maximum image similarities across the models for the 0.5 m, 1.0 m, and 2.0 m scenarios are, respectively, 0.955, 0.895, and 0.834. These all correspond to the RTM method. The general trends in similarity values amongst each migration technique are discussed below.

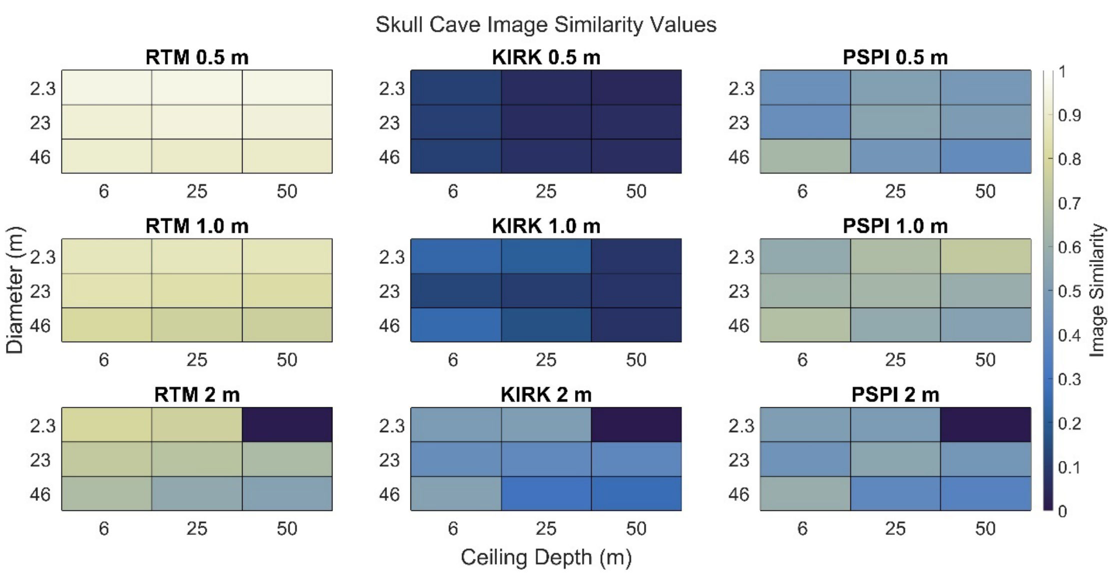

Figure 34. Example image similarities measured as the fit between the input model spaces and output migration images for each of the Skull Cave models with 0.5 m, 1.0

m, and 2.0 m geophone spacing. A value equal to 1 indicates a perfect fit, with misfit increasing the lower the number.

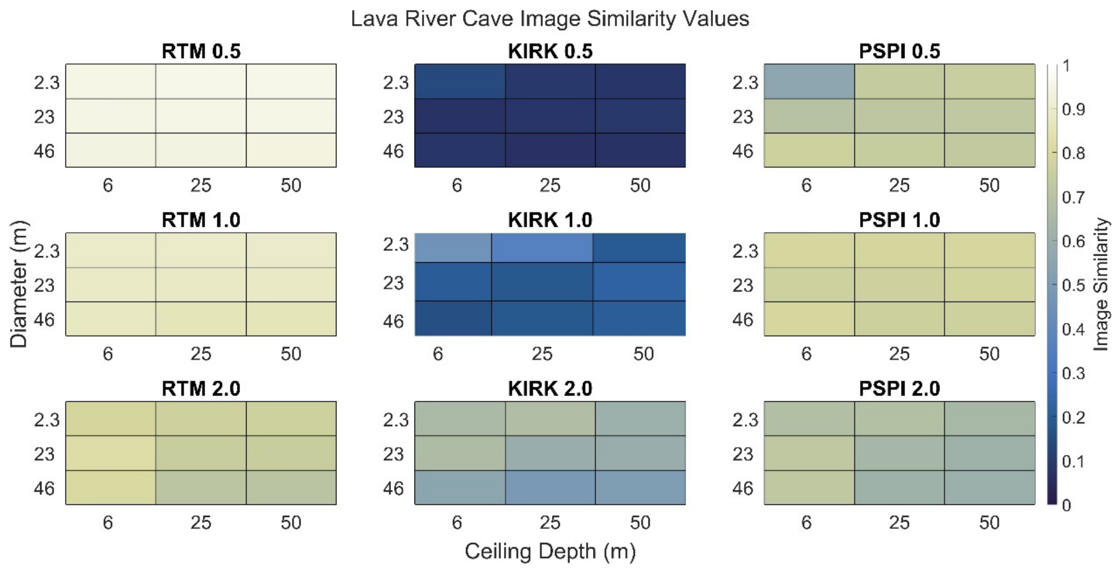

Figure 35. Example image similarities measured as the fit between the input model spaces and output migration images for each of the Lava River Cave models with 0.5 m, 1.0 m, and 2.0 m geophone spacing. A value equal to 1 indicates a perfect fit, with misfit increasing the lower the number.

The image similarity results offer complementary overarching results to those from qualitative analysis of the migrations techniques and the quantitative depth and width analyses. This is apparent in Figures 34 and 35, where the RTM results on average have the lowest misfit between the migration images and the input velocity model for all lava tube models across the three geophone spacing variations (Table 4). Kirchhoff migration exhibits the lowest average image similarity, with all three migration methods demonstrating similar fit for 2.0 m geophone spacing Lava River Cave models (Fig. 35).

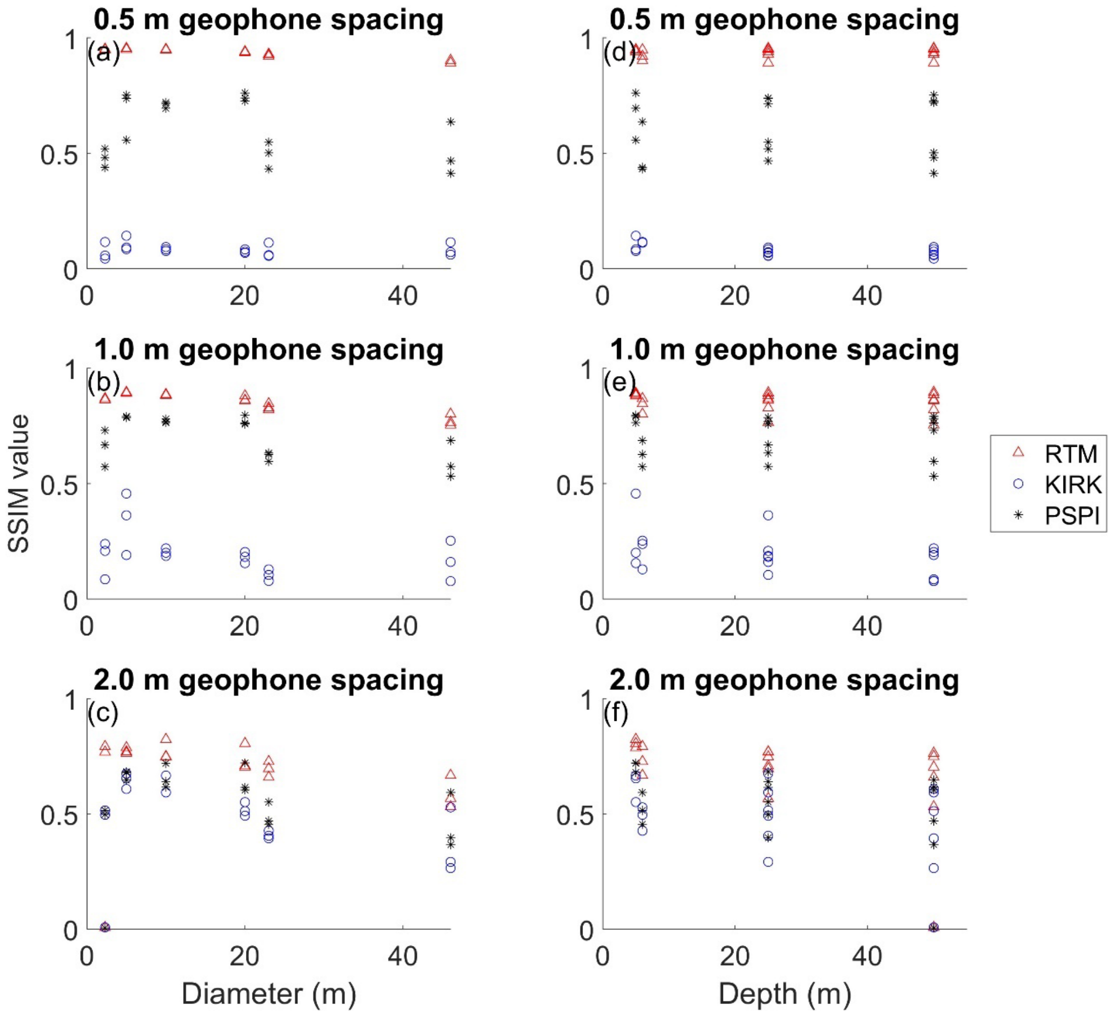

Figure 36. SSIM values for all Skull Cave and Lava River Cave models based on lava tube diameters, a), b), c), and lava tube ceiling depths, d), e), f). A larger value, i.e., closer to 1.0, indicates higher similarity.

Migration	**0.5 m mean SSIM**	**1.0 m mean SSIM**	**2.0 m mean SSIM**
RTM	0.936	0.853	0.682
Kirchhoff	0.083	0.195	0.482
PSPI	0.603	0.701	0.543

Table 4. Mean image similarity values across migration techniques depending on input geophone spacing.

There is an apparent trend in the image similarity analysis' results when comparing each individual migration technique's efficacy against differing geophone spacings. From Fig. 36, on average the migration techniques display lower misfit with higher spacing between geophones. RTM displays similarity decreases from an average 0.983 for 0.5 m spacing to an average 0.682 for 2.0 m spacing (Table 4). RTM further displays a marked contrast between the results for Skull Cave and Lava River Cave, with Skull Cave migrations showing the highest similarity values, and a decrease in similarity for the Lava River Cave models. PSPI and Kirchhoff migration image similarity trend within a single order of magnitude across geophone spacings; PSPI migration exhibits the highest image similarity for the 2.0 m grid spacing migrations, while Kirchhoff varies. The similarity in Kirchhoff migration misfits, regardless of lava tube size and depth, implies a general misfit trend inherent to that migration technique. It is also worth noting that the Kirchhoff migrations have higher misfit values for the Lava River Cave migrations, similar to the trend for RTM. PSPI migration presents similar misfit values across both lava tube model spaces.

Chapter 4: Discussion

Here we address two topics 1) recovery of the input lava tube model and 2) the effect of our assumptions. In terms of recovery, this research presents the results of each migration technique's reconstruction of lava tube models depending on 1) depth, 2) width, and 3) station spacing. These variations likewise depend on the input lava tube size and shape. Our main assumptions for lava tube model and synthetic seismogram creations are: 1) a uniform basaltic background velocity surrounding an air-filled lava tube, 2) a clean seismic wavefield with only numeric noise, 3) clear first arrivals from the wavefields to pick on, and 4) that seismic methods may be used to detect void spaces.

Before evaluating the individual efficacy of each migration technique, the assumptions that went into the process must be noted. For the picking code technique, we assume that 1) the first peak value above a certain threshold is the reflected wave first arrival, and 2) any peak within this criterion along the entirety of the model horizontal axis is associated with the lava tube. This may result in inaccuracy in the depth estimation by picking low-frequency noise that surrounds the lava tube signal, as well as inaccuracy in the width estimation by picking numerical noise rather than the lava tube signal. Future experiments would incorporate varying levels of background noise.

Both the RTM and Kirchhoff methods have their uses in exploration seismology, as well as their specific limitations: Kirchhoff methods are less reliable than RTM methods when it comes to the complexity of migrated structure (e.g., the RTM method will be more able to recover a vertically and laterally varying structure), whereas the RTM method requires a sufficiently accurate baseline model space *a priori*, as is demonstrated by its increasing inaccuracy with geophone spacing in Section 3.3 (Baysal et al. 1983, Zhou et al. 2018., Chang and McMechan 1987, Chattopadhyay and McMechan 2008, Zhu and Lines 1998, Virieux and Operto 2009).

4.1 Method Accuracy

4.1.1 Geophone Spacing

From the results presented in Section 3.3, we can conclude that RTM on average produces the closest reconstructed images to the input for tube depth across each geophone spacing, while PSPI is the most accurate at reproducing tube width across geophone spacings (Fig. 23-27, Table 2, Table 3). In both depth and width reconstruction, Kirchhoff performs the worst with the highest misfit values when compared to RTM and PSPI. RTM and PSPI migration highlight the negative effect on lava tube reconstruction that results from increasing geophone spacing with respect to both lava tube depth and width. While the Kirchhoff migration method demonstrates this effect for width reconstruction, the inaccuracy varies across geophone spacings for depth reconstruction. These results are consistent with the findings of Du et al. (2006) and Zhu and Lines (1998), discussed in the Chapter 4 introductory paragraphs. As expected, regardless of migration technique, the most accurate results are found for the denser geophone spacing of 0.5 m.

4.1.2 Depth and Width Estimation

The best methods of migration for calculating tube depth and width across each technique are calculated in Table 5 and Table 6. RTM presents the lowest

RMSE value for the 2.0 m grid spacing scenario for the Lava River Cave model with 10 m diameter and 25 m ceiling depth, and RTM similarly presents the lowest total width misfit value for the 0.5 m grid spacing scenario for the Skull Cave model with 46 m diameter and 50 m ceiling depth. These values are separate from the general trends of each method's applicability, which are shown in Tables 2 and 3 and Figs. 24 through 29.

Migration Type	**Model**	**Value (RMSE in +/- m)**
RTM	2.0 m spacing, Lava River Cave, 10 m diameter, 25 m ceiling depth	0
Kirchhoff	1.0 m spacing, Skull Cave, 2.3 m diameter, 6 m ceiling depth	0.8165
PSPI	0.5 m spacing, Skull Cave, 23 m diameter, 50 m ceiling depth	1

Table 5. Minimum RMSE values for each migration technique across all the geophone spacings.

Migration Type	**Model**	**Value (width misfit)**
RTM	0.5 m spacing, Skull Cave, 46 m diameter, 50 m ceiling depth	0.25
Kirchhoff	1.0 m spacing, Skull Cave, 2.3 m diameter, 25 m ceiling depth	1
PSPI	0.5 m spacing, Skull Cave, 2.3 m diameter, 6 m ceiling depth	0.75

Table 6. Minimum width misfit values for each migration technique across all the geophone spacings.

Based on ceiling depth reconstruction (Fig. 24-29), Kirchhoff is the least accurate method, and RTM and PSPI are the most consistently accurate across geophone spacings and lava tubes, with RTM holding the lowest values for 0.5 m grid spacing. RTM for 0.5 m grid spacing is the most accurate method. None of the three methods recover the tube floor after picking first arrivals; this is consistent with what we would expect from seismic data collected over an air-filled cavity and would extend to voids with vacuum. The impedance contrast is sufficiently high that the majority of the seismic energy is reflected, leaving tube floor detection unlikely; this is contrasted by GPR techniques, which when modelled, may detect void floors (Esmaeili et al. 2020, Wike et al. 2022).

These findings represent the quantifiable depth and width of lava tubes given a 100 Hz source frequency. From the relationship between frequency, velocity, and wavelength (Shearer 2009), we can expect this source frequency to be sensitive to lava tubes at and above its wavelength. For a basaltic composition matrix with 3 km/s velocity, this corresponds to a 30 m wavelength, and for a basaltic composition matrix with 1.5 km/s velocity, this corresponds to a 15 m wavelength. This respectively sets 30 m and 15 m as the minimum diameters for the Skull Cave and Lava River Cave lava tube models. Based on our results of detecting lava tubes above and below these minimum diameters, we expect to reliably locate lava tubes at or above this diameter given our used 100 Hz source frequency. This is the source frequency attributed to a common man-made Earth active seismic source, that of a 10 lb hammer hitting an aluminum plate (Brom and Stan-Kłeczek 2015). This is an order of magnitude larger than the roughly 22 Hz thumper source for the Lunar Active Seismic Experiment (Mahvelati and Coe 2020). Seismology's dependence on wavelength for void detection is comparable to that of GPR, where waves can only sample structures at or above their respective wavelength (Esmaeili et al. 2020). Chapter 3 illustrates how lava tubes below these respective minima are recovered, given no non-numeric noise; however, the ability of each migration method to locate larger tubes is expected given the relationship between wavelength and the chosen source frequency.

From the relationship between seismic wave wavelength and the size of the target structure, we might conclude that lower frequency seismic sources should be used to detect deeper lava tubes. Higher frequency waves that travel to a deeper tube will experience more seismic attenuation. We know $E = \rho A^2\omega^2$ (Shearer 2009), where the mean energy of a seismic wave (E) is proportional to the density (ρ), the wave amplitude squared (A^2), and the wave frequency squared (ω^2). We also know that attenuation alters the seismic wave propagation dependent on frequency, where $A(x, t) = A_0 e^{-\omega x/2cQ_e - i\omega(t - x/c)}$ (Shearer 2009), where A is amplitude as a function of position and time, A_0 is original amplitude, ω is frequency, c is velocity, t is time, x is distance, and Q_e is the quality factor, or quantification of attenuation and scattering within a medium. As they are proportional, both frequency and distance decrease the amplitude of seismic waves. The effect of this can be seen as the deeper a lava tube, the less signal that will return to the surface from reflections. Higher frequency waves will impart more energy to be dissipated with depth while being more affected by attenuation. Our chosen frequency of 100 Hz identifies high amplitude reflections from the modelled lava tubes. Future work would expand upon the sensitivity of the various methods based upon attenuation effects, which were not included in our modeling efforts.

4.1.3 Similarity Matrix

Based on figures 34 through 36 and Table 4, RTM provides a better similarity matrix between the input velocity model and the resultant reconstructed lava tubes. RTM displays the lowest misfit values, particularly for the case of Skull Cave lava tubes, while PSPI and Kirchhoff migrations vary across lava tubes, while present similar misfit values to each other. From this, PSPI provides the most consistent image similarity across lava tube sizes and shapes and is the most applicable to these void spaces in general. RTM appears highly variable with lava tube shape and size but is the most accurate across each method, especially for the specialized case of Skull Cave geometries. Kirchhoff migration results are more variable than PSPI, with a similar increase in fit value for the Skull Cave geometries, while retaining high misfit values of the same order of magnitude as PSPI.

This method of determining the effectiveness of migrations at reconstructing image tubes is sensitive to low-frequency noise and artifacts, as these will affect the grayscale image comparison between the clean velocity model and the results from each migration technique. The sensitivity of SSIM to low-frequency noise is most apparent when using the Kirchhoff method, as the corresponding results have the lowest image similarity and present the highest noise content in Section 3.1.1 and Section 3.2.1. Qualitatively, the RTM reconstructions are the most similar to the input velocity model, so we expect the image similarity values to be highest for this method. PSPI migrations hold the middle ground for noise content as well as for image similarity. For SSIM, RTM presents the most accurate method, PSPI the second most accurate, and Kirchhoff the least accurate. Future work to filter the low-frequency noise could improve the quality of the reconstructions.

4.2 Uncertainties and Assumptions

RMSE values are the standard deviation of the residuals between our picking of the lava tube outline and the input lava tube models and represent the uncertainty in our determination of lava tube ceiling depth. Our method of picking the first break as the lava tube signal, rather than the maximum amplitude wavelet, translates to uncertainty in our estimated depth; both methods are equally viable for traditional seismic picking methods, and are a user preference. For a background velocity of 3 km/s, a 0.01 s difference in picked arrival time translates to a 30 m difference in depth. Fig. 37 shows an example of the offset found between our first break and the maximum positive amplitude wavelet, where the difference between the two is one meter.

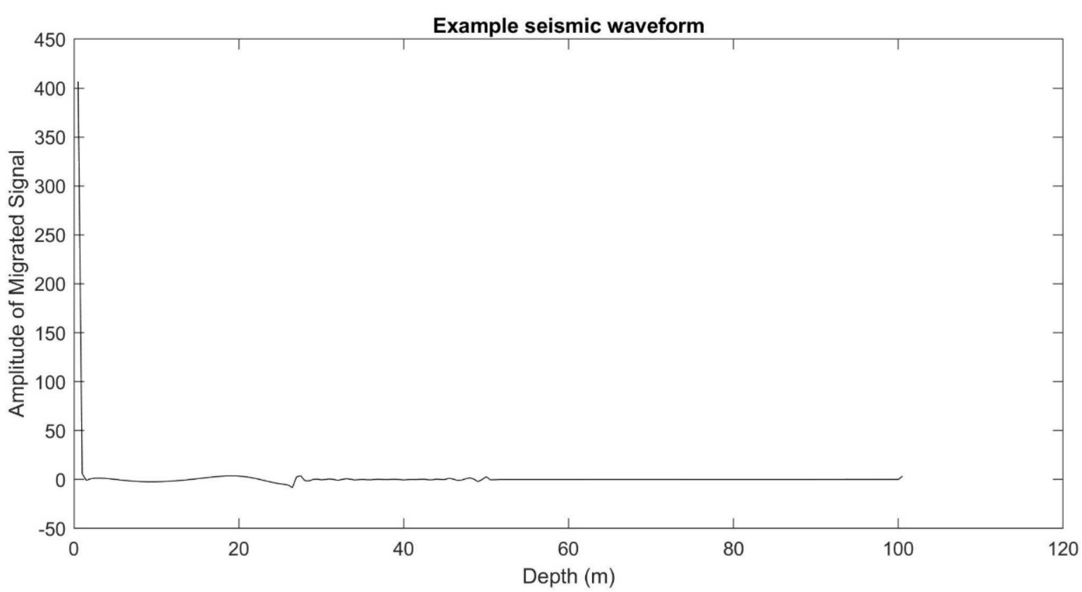

Figure 37. Example synthetic RTM waveform for the Skull Cave model with 46 m diameter, 25 m ceiling depth, and 0.5 m geophone spacing. The first break is located at 27 m. Future work could filter out the low-frequency background to make picking more robust and tube signals more apparent.

Here, we use a ground-truth, or known velocity model due to the synthetic nature of the experiment; however, in nature, this velocity model is dependent on a robust *a priori* refraction survey or information from other geophysical surveys (e.g., GPR, gravity, magnetic) that are sensitive to and would constrain the subsurface velocity structure. The output of migration would be sensitive to the accuracy of the input velocity model, as from the proportional relationship between velocity and distance (Shearer 2009) we can expect a 10% uncertainty in velocity to lead to a 10% uncertainty in distance (depth). To address our assumption of a synthetic case with known information, we would supplement real-world acquisition methods with joint geophysical datasets to both define a robust velocity model and compare migration reconstructions.

We also note that our findings fail to recover the lava tube walls and floor, with only lateral extent and ceiling depth recovered. This leads to an uncertainty in overall geometry, which would likewise need to be supplemented by seismic refraction, GPR, magnetics, gravity, and other geophysical methods.

The assumption of a synthetic seismic wavefield based on FDM inversion incorporates the limitations of that method into the accuracy and uncertainty of our results. FDM and FEM are comparable in the laterally homogeneous, vertically inhomogeneous domain (Marfurt 1984). As discussed in Chapter 2, FDM is affected by grid dispersion where FEM is not; this dispersion is particularly notable at higher frequencies (Yao et al. 2016). We expect the uncertainty in our migration reconstructions to therefore incorporate dispersion inaccuracies inherent to a 100 Hz seismic wave. The FDM is further limited by needing a regular grid, which can limit its applications to complex topography and geometries; however, this complexity may be approximated with finer grids. Finite-difference modeling is widely accepted as a simulation technique despite this limitation (Zhu and Lines 1998, Virieux and Operto 2009, Marfurt 1984, Yao et al. 2016, Gritto et al. 2004) and its advantages in adaptability and cost-effectiveness outweigh this uncertainty.

Each of the three migration techniques has its individual assumptions and limitations. As an overview, Kirchhoff migration is the most cost-effective but most ill-suited to migrating media containing vertical and lateral inhomogeneity (Du et al. 2006). PSPI migration is less cost-effective than Kirchhoff but can manage lateral variations in anisotropy, albeit not as well for rapid differences in velocity and with an assumption of input reference wavefields (Du et al. 2006). RTM is the least cost-effective of the three methods but the most accurate and flexible for reconstruction of lateral anisotropy and complex velocity variations, while requiring a robust velocity background model (Du et al. 2006). These assumptions and effects are clear in our results, where Kirchhoff migrations reconstruct hyperbolic lava tube shapes that extend the breadth of the model space, representing more an angled layer than a laterally discrete void space.

Du et al. (2006) found that in terms of anisotropic media, Kirchhoff migration holds the benefit of cost-effective migration, RTM proves the most reconstruction-effective at imaging dip angles and complex media, and PSPI is the middle-ground between the other methods. These finding are consistent with our results, where Kirchhoff migrations take the least time (order of tens of seconds), while RTM presents the highest fidelity reconstruction with longer computation time (order of tens of minutes), and PSPI is a middle-ground between the two. We note that the study by Du et al. (2006) analyzed anisotropic methods while we did not; however, their overall comparison of the migration techniques remains analogous. A discussion of two of the migration methods was previously asserted by Zhu and Lines (1998), where they compare Kirchhoff and RTM reconstructions for a synthetic model of a region with steeply dipping faults and a real-world dataset. For the synthetics with an exact background velocity model, Zhu and Lines (1998) found that the RTM results more accurately reconstructed the subsurface structure when compared to the Kirchhoff results. Without the assumption of an *a priori* velocity model, the two methods presented similar reconstructions. Their findings of RTM being more accurate for regions of steep layers (a lava tube wall) are validated by our findings; however, our results for a migration with a uniform background velocity model, Section 3.1, contradict their assertion that the two migration methods are compatible for this case.

4.3 Recommendations

4.3.1 Terrestrial Lava Tubes

Previous geophysical studies targeting Earth lava tubes have concluded that a combination of methods is practical for real-world data and its limitations (Meglich et al. 2003, Esmaeili et al. 2020, Bell et al. 2022). For the case of a coordinated GPR and shear wave seismology investigation, the GPR method only reliably imaged to depths of 4 m, while the latter reached double the depth at 8-9 m (Meglich et al. 2003). GPR techniques may be utilized to penetrate deeper with different source frequencies, with the limitation that high-frequency GPR will more readily attenuate and low-frequency GPR will have higher wavelengths that may not sample lava tubes (Esmaeili et al. 2020). Our results demonstrate that seismic techniques viably locate lava tubes up to 50 m deep within Earth-like material, with the limitation that the smaller lava tubes proportionally have the largest depth and width misfit (Fig. 28-29). GPR methods used with seismic methods will augment one another's ability to detect the range of lava tube depths and sizes.

Magnetic techniques are viable in lava tube detection, with deeper lava tubes more visible if they have larger diameters (Bell et. al 2022). This conclusion contrasts our data, where larger lava tubes at depth have similar misfit (Fig. 24-27) or greater misfit (Fig. 24-27) against the input lava tube model than their smaller, shallower counterparts. This presents another opportunity for a joint geophysical analysis, where magnetic data can augment seismic data.

For the case of terrestrial analog fieldwork and characterization of lava tubes, or other large voids at depth, our work demonstrates that RTM and PSPI migration techniques present an improvement over Kirchhoff migration. Our work implies that an increase in lava tube depth decreases their detectability, while lava tube size does not clearly affect detectability.

There is also a marked increase in lava tube ceiling depth and lateral width recovery when utilizing 0.5 m geophone spacing along the modeled 90 m seismic line. For time-effective studies, 1.0 m geophone spacing presents less accurate, but worthwhile results. The models and simulations discussed utilize Earth basaltic parameters for two bulk unconsolidated, basaltic materials (Skull Cave unconsolidated, 3.0 km/s P-wave velocity; and Lava River cave unconsolidated, 1.5 km/s P-wave velocity), and the interior of the lava tubes are filled with air (0.350 km/s P-wave velocity); this allows for their results to be directly compared to the expected outputs of fieldwork conducted over terrestrial lava tubes. The results from our seismic simulations show that PSPI and Kirchhoff migration are capable of migrating data containing terrestrial lava tubes. This finding is consistent with a prior study that found that these migration methods can migrate GPR data containing lava tubes (Esmaeili et al. 2020). Denser seismic receiver spacing has been attributed to higher quality data (Dean 2012, Campman et al. 2016), and this holds true for our simulations and analysis. Two NASA Solar System Exploration Research Virtual Institute (SSERVI) GEODES expeditions targeted Skull Cave and Lava River Cave utilized 0.5 m geophone spacing along lines similar in length to the modelled 90 m. In further field expeditions, we recommend maintaining a maximum 0.5 m geophone spacing with down sampling opportunities to analyze RTM, PSPI, and Kirchhoff's' effectiveness on field data at 1.0 m and 2.0 m receiver spacing.

4.3.2 Lunar and Martian Lava Tubes

Applications of terrestrial-based recommendations to the Moon and Mars are less straightforward, as the physical parameters of rock material surrounding lava tubes and voids vary greatly (Esmaeili et al. 2020). In particular, the seismic velocities of our closest extra-terrestrial field site, the Moon, are 0 km/s velocity for vacuum, 0.1-1.1 km/s for the P-wave, and 0.04-0.58 km/s for the S-wave velocities for the regolith (Chang and McMechan 1987). The martian shallow subsurface (meter-scale) has similar P-wave velocities constrained as hundreds of meters per second (0.15-0.25 km/s) (Morgan et al. 2018, Bates et al. 2022). Lava tubes are proposed to exist on the Moon and Mars, with depths and widths ranging on the order of meters to kilometers (Kaku et al. 2017, Chappaz et al. 2017, Sauro et al. 2020), and they are expected to be stable within this size range (Blair et al. 2017, Sauro et al. 2020). Our lava tube simulations range on the order of tens of meters in both depth and width, corresponding to the terrestrial-adjacent, lower end of lunar and martian lava tubes.

To characterize kilometer-scale voids, seismic lines would need to be scaled up to the order of kilometers to span them. Assuming the physics scale linearly, we expect that the effects of lava tube scaling would apply in the following way: we obtain higher-fidelity migration results for a Skull Cave lava tube with 46 m diameter, 50 m depth, 0.5 m geophone spacing, and a 90 m seismic line; thus, for a lunar lava tube with ~1000 m diameter and ~100 m depth, the geophone spacing would scale to ~10 m station spacing along a ~2000 m seismic line, for ~200 total stations. For a smaller scale example, a ~100 m diameter, ~50 m depth lava tube on the Moon or Mars would only need ~1.0 m station spacing along a ~200 m seismic line, for again, ~200 total stations. Section 4.2.2 discussed the scaling between velocity, source frequency, and wavelength, a median velocity for the lunar near subsurface discussed above is 0.5 km/s. With our source frequency of 100 Hz, this leads to a wavelength of 5 m. A lava tube on the order of a kilometer will appear as a relatively flat surface, with a slight incline when examined with this Earth-based source frequency; instead, a frequency of 0.5-1 Hz would be needed for a wavelength of 0.5-1 km that can adequately sample the curved structure. Lunar and martian seismic studies of void spaces will need to utilize lower source frequencies of this order to detect larger lava tubes at depth.

Due to the lower seismic velocities inherent to the lunar and martian shallow subsurface, travel-times of the lava tube reflections would increase, requiring longer-duration seismic acquisition. Both the lunar and martian regolith have thicknesses on the order of meters to tens of meters (McKay et al. 1991, Ziborov et al. 2024), well above the expected lava tube ceiling depths; for regions containing lava tubes, we can expect volcanic material, or unconsolidated basalt, to underlie the regolith and overlie the lava tubes. The shallow lunar and martian sub-surfaces are described in Sollberger et al. (2016) and Lognonné et al. (2020). In terms of bulk material, lower velocities can be attributed to higher porosity, lower density materials (Shearer 2009), which in turn leads to higher attenuation and lower signal-to-noise ratio. These low-density, scattering regolith materials above lava tubes on the Moon and Mars will likely lead to less coherent reflection signals due to higher attenuation (Onodera et al. 2022). A higher density of geophone spacing, as well as the more costly migration techniques of RTM and PSPI, is the most likely scenario for seismic recovery of lunar and martian lava tubes.

Chapter 5: Conclusions

Lava tubes are a subsurface void found on the Earth, the Moon, and Mars; their depths and lateral extents may vary on the order of meters to kilometers in scale. Methods of detecting and characterizing lava tubes on Earth include remote sensing, direct access, and geophysical techniques, with one of the predominant geophysical techniques being seismology. Seismology has been utilized to detect various Earth void spaces, including caves, karsts, coal seams, and lava tubes. One of the first steps in determining how we will discover lava tubes on the Moon and Mars is to benchmark our ability to define them on Earth.

We created a suite of eighteen terrestrial analog lava tubes constructed from LiDAR data of Skull Cave, CA, and Lava River Cave, AZ, to simulate the diversity of these structures found on Earth. Our analysis of three migration techniques, RTM, PSPI, and Kirchhoff, concluded that each method can detect lava tubes of various depths, widths, and surface geophone spacing; however, RTM and PSPI proved the more accurate methods, with RTM particularly accurate at reconstructing lava tube ceiling depth, while Kirchhoff, the traditional migration method, proved the least accurate method. The results of our first break pick method found that, before diameter comparison, smaller lava tubes were more accurately picked across the methods. When compared after normalizing each depth and width inaccuracy against the input lava tube diameter, the misfits for larger lava tubes were lower than for smaller ones. We also find that shallower lava tubes generally display lower misfit in migrated ceiling depth and width than deeper lava tubes. Image similarity matrix analysis found that RTM reconstructions were, on average, more similar to the input lava tube geometry model than PSPI and Kirchhoff reconstructions. We found that a setup of 0.5 m geophone spacing demonstrated the lowest depth and width inaccuracies, on the order of one to five meters. None of the migration methods reliably located lava tube floor depths via picking methods.

We chose these three migration techniques of reflection seismology due to their adaptability; RTM, PSPI, and Kirchhoff migration have been applied extensively to reconstructions of the shallow subsurface, with the ability to resolve laterally inhomogeneous media (e.g., lava tubes). However, each technique uses a pre-defined background velocity model in its reconstruction, which will not be readily available for studies on the Moon and Mars. Section 3.1 shows how each method can recover a lava tube model given ana background velocity model made of pure basalt and lacking a lava tube structure. This research does not incorporate noise beyond the numeric noise inherent to the FDM synthetic simulations; we expect the incorporation of real-world noise on Earth, the Moon, and Mars to negatively impact reflection migration reconstructions.

Aside from real-world noise, these simulations likewise did not investigate the material properties of lunar and martian regolith, and their effects on the scattering and attenuation of the seismic wave. We assumed Earth-like media with an appropriately high source frequency and implemented these parameters into realistic tube geometries with air-filled void properties, created synthetic seismic 2D wavefields interacting with these geometries, and analyzed the effect of geophone spacing, lava tube depth, and lava tube width on the reflection migration reconstructions. We expect our findings to vary when applied to lunar and martian media, particularly the source frequency, which will need to be lower to identify larger tubes in higher-attenuating media; however, this is beyond the scope of this project.

These findings can be applied to the characterization of lava tube ceiling depth and lateral extent on the Moon and Mars. Based on differing material properties, we can expect higher scattering attenuation within the lunar and martian regolith to negatively impact the resultant lava tube signal. We can also expect the necessity of longer seismic lines with proportionally larger geophone spacing due to the scale of these features. Though more costly, RTM and PSPI migration techniques are the most likely to detect extra-terrestrial lava tubes, and we advise utilizing them. An investigation into the exact effect of lunar and martian regolith and lava tube scale on the results of each migration technique is beyond the scope of this project; a further investigation into using this workflow to simulate and evaluate kilometer scale lava tubes and geophone lines is recommended.

Appendix A

Seismic Simulation Parameters and Results

The fifty-four FDM seismic simulations corresponding to the Skull Cave and Lava River Cave geometries for each geophone spacing scenario are presented in the Digital Repository of the University of Maryland as supplemental materials to this thesis. These data are attached to the thesis as supplemental materials.

This directory contains a README.txt describing the data format and content of each file, the architecture of the archive, and an overview of the creation and analysis of the synthetics, as well as a spreadsheet in the form of Microsoft Excel listing each .dat file and its properties and metadata. The FDM and SPECFEM2D synthetics are in the form of SEG-2 .dat files (Pullan 1990) and follow a general nomenclature of shot1_xx_xx_tube.dat, where in order the xx represent the horizontal and vertical grid numbers and tube denotes the lava tube field site, diameter, and ceiling depth. For example, shot1_181_201_sb6.dat corresponds to a 181 by 201 grid, or 0.5 m geophone spacing, containing the Skull Cave lava tube model with a larger, 46 m, diameter, and 6 m ceiling depth. Included in the directory is a Microsoft Excel spreadsheet listing the results of our diagnostic measures (RMSE, width misfit, and structural similarity) for each of the 54 FDM simulations.

We also archive the results of our SPECFEM2D simulations for reference, in SEG2 and MATLAB format, as well as the parameter files used to run the code as necessary for subsequent analysis.

Appendix B

Lava Tube	Field Site	Diameter (m)	Depth (m)	RTM RMSE (m)	KIRK RMSE (m)	PSPI RMSE (m)	RTM Width Misfit (m)	KIRK Width Misfit (m)	PSPI Width Misfit (m)	RTM Image Fit (unitless)	KIRK Image Fit (unitless)	PSPI Image Fit (unitless)	Geophone Spacing (m)
Skull	1	46	6	1.755	2.385	1.04	21	21	6	0.903	0.115	0.637	0.5
Skull	1	46	25	3.433	9.098	4.514	6	22.5	23.5	0.892	0.072	0.468	0.5
Skull	1	46	50	4.692	3.756	1.194	0.5	21	46	0.892	0.061	0.413	0.5
Skull	1	23	6	0.598	2.305	2.06	13.5	32	17.5	0.921	0.113	0.432	0.5
Skull	1	23	25	0.591	10.082	1.017	4	32	6.5	0.93	0.056	0.548	0.5
Skull	1	23	50	0.54	4.823	1	10.5	26.5	18	0.928	0.059	0.502	0.5
Skull	1	2.3	6	0.353	NaN	1.145	2.5	3.5	1.5	0.949	0.116	0.439	0.5
Skull	1	2.3	25	0.353	NaN	1.145	2.5	6	1.5	0.952	0.057	0.52	0.5
Skull	1	2.3	50	0.612	NaN	1.354	1.5	3.5	2	0.951	0.044	0.482	0.5
Lava River	2	20	5	2.793	7.508	2.152	39.5	26.5	20.5	0.94	0.084	0.762	0.5
Lava River	2	20	25	3.03	1.504	3.355	30.5	39	3	0.941	0.069	0.74	0.5
Lava River	2	20	50	2.298	5.29	2.853	35.5	39	6	0.937	0.074	0.727	0.5
Lava River	2	10	5	0.777	2.489	1.889	33.5	25.5	19.5	0.948	0.077	0.695	0.5
Lava River	2	10	25	2.018	0.927	1.526	25	46.5	6.5	0.95	0.084	0.714	0.5
Lava River	2	10	50	1.08	3.473	2.209	18	36.5	9	0.951	0.094	0.72	0.5
Lava River	2	5	5	0.866	2.269	1.865	7.5	19.5	34.5	0.95	0.143	0.558	0.5
Lava River	2	5	25	1.067	1.03	2.279	15.5	29	6	0.955	0.092	0.738	0.5
Lava River	2	5	50	0.816	NaN	2.5	12	20.5	4	0.955	0.085	0.752	0.5
Skull	1	46	6	2.908	8.857	1.707	21	21	13	0.801	0.253	0.687	1
Skull	1	46	25	4.197	16.37	1.558	21	25	27	0.765	0.161	0.574	1
Skull	1	46	50	7.468	14.693	NaN	20	21	48	0.754	0.078	0.531	1
Skull	1	23	6	5.159	15.731	1.829	24	30	20	0.846	0.129	0.627	1
Skull	1	23	25	3.302	12.241	1	25	30	17	0.828	0.105	0.633	1
Skull	1	23	50	3.64	6.835	NaN	31	29	25	0.82	0.079	0.597	1
Skull	1	2.3	6	0.707	NaN	NaN	3	8	5	0.868	0.239	0.572	1
Skull	1	2.3	25	1	0.816	NaN	16	1	5	0.868	0.209	0.668	1
Skull	1	2.3	50	1	NaN	NaN	16	32	5	0.863	0.086	0.73	1
Lava River	2	20	5	3.02	3.572	4.64	40	39	12	0.88	0.156	0.795	1
Lava River	2	20	25	3.636	NaN	2.549	36	23	12	0.861	0.183	0.758	1
Lava River	2	20	50	3	NaN	5.099	35	31	6	0.859	0.204	0.762	1
Lava River	2	10	5	1.795	2.949	3.76	33	47	7	0.886	0.201	0.764	1
Lava River	2	10	25	2.788	NaN	3.681	36	12	8	0.882	0.187	0.769	1
Lava River	2	10	50	3.333	NaN	5.419	30	12	4	0.885	0.22	0.779	1
Lava River	2	5	5	1	1.095	3	21	26	7	0.891	0.457	0.79	1
Lava River	2	5	25	0.5	NaN	2.549	26	8	6	0.893	0.363	0.786	1
Lava River	2	5	50	2.958	NaN	2.889	16	8	8	0.895	0.191	0.791	1
Skull	1	46	6	6.179	6.369	4.375	22	24	4	0.667	0.528	0.592	2
Skull	1	46	25	7.354	5.848	12.124	20	26	34	0.567	0.292	0.397	2
Skull	1	46	50	5.273	15.32	2.696	22	6	32	0.531	0.265	0.366	2
Skull	1	23	6	3.286	NaN	7.659	36	54	4	0.727	0.427	0.455	2
Skull	1	23	25	6.033	6.164	6	26	42	22	0.696	0.405	0.552	2
Skull	1	23	50	5.859	3.829	4	28	50	30	0.659	0.394	0.469	2
Skull	1	2.3	6	NaN	NaN	2	16	18	46	0.792	0.496	0.515	2
Skull	1	2.3	25	NaN	2	NaN	28	18	4	0.768	0.515	0.497	2
Skull	1	2.3	50	NaN	NaN	2	6	20	6	0.008	0.008	0.006	2
Lava River	2	20	5	3.316	2.256	3.794	26	28	38	0.805	0.551	0.721	2
Lava River	2	20	25	4.527	10	6.266	34	54	36	0.708	0.492	0.615	2
Lava River	2	20	50	5.398	9.213	5.249	36	42	30	0.703	0.512	0.604	2
Lava River	2	10	5	2.449	1.549	3.872	36	14	40	0.823	0.666	0.719	2
Lava River	2	10	25	0	5.291	5.416	40	26	34	0.747	0.593	0.64	2
Lava River	2	10	50	3.464	3.687	4	36	38	30	0.749	0.593	0.617	2
Lava River	2	5	5	2	2	2	28	4	38	0.787	0.654	0.679	2
Lava River	2	5	25	NaN	NaN	NaN	34	30	40	0.769	0.675	0.683	2
Lava River	2	5	50	4	2	4	26	28	14	0.763	0.608	0.646	2

Table B1. The RMSE, width misfit, and similarity matrix values (image similarity) for the 54 lava tube seismic simulations. A NaN (not a number) value indicates failure to constrain a value, or maximum misfit for the pick process. The Microsoft Excel spreadsheet is included in the directory referenced in Appendix A.

Bibliography

Alam, M., Abbasi, S., & Riikola, L. (2021). Near-surface void characterization using surface-wave inversion. *SEG Technical Program Expanded Abstracts*: 3250-3254. https://doi.org/10.1190/segam2021-3583712.1

Almadani, M, bin Waheed, U., Masood, M., & Chen, Y., (2021). Dictionary learning with convolutional structure for seismic data denoising and interpolation. *Geophysics, 86*, 361-374. DOI: 10.1190/geo2019-0689.1

Bailey, N. (1967). Cinder Lake crater field location test. *U.S. Geological Survey, Open-File Report 67-7*. https://doi.org/10.3133/ofr677

Bakurov, I., Buzzelli, M., Schettini, R., Castelli, M., & Vanneschi, L. (2022). Structural similarity index (SSIM) revisited: A data-driven approach. *Expert Syst. Appl., 189*, 116087. https://doi.org/10.1016/j.eswa.2021.116087

Bates, A., Lorenzo, J.M., & Karunatillake, S. (2022). Seismic experimentation to further understanding of martian regolith ice. *53rd Lunar and Planetary* Science Conference: 2417.

Baysal, E., Kosloff, D., & Sherwood, J. (1983). Reverse time migration. *Geophysics, 48*(11), 1514-1524. https://doi.org/10.1190/1.1441434

Bednar, J.B. (2005). A brief history of seismic migration. *Geophysics, 70*(3), 3MJ20MJ. https://doi.org/10.1190/1.1926579

Bell, E., Schmerr, N., Young, K., Esmaeili, S., Garry, W. B., Jazayeri, S., Kruse, S., Richardson, J., & Whelley, P. (2022). Field mapping and modeling of terrestrial lava tube magnetic anomalies as an analog for lunar lava tube exploration and prospecting.

Journal of Geophysical Research: Planets, 127(6), 1-26. https://doi.org/10.1029/2021JE007140

Blair, D.M., Chappaz, L., Sood, R., Milbury, C., Bobet, A., Melosh, J.H., Howell, K.C., & Freed, A.M. (2017). The structural stability of lunar lava tubes. *Icarus, 282*, 47–55. https://doi.org/10.1016/j.icarus.2016.10.008

Braden, S.E., Stopar, J.D., Robinson, M.S., Lawrence, S.J., van der Bogert, C.H., & Hiesinger, H. (2014). Evidence for basaltic volcanism on the Moon within the past 100 million years. *Nature Geoscience, 7*(11), 787-791. https://doi.org/10.1038/NGEO2252

Brom, A., & Stan-Kłeczek, I. (2015). Comparison of seismic sources for shallow seismic: sledgehammer and pyrotechnics. *Contemporary Trends in Geoscience, 4*(1), 39-45. https://doi.org/10.1515/ctg-2015-0004

Buckley, F. & Lane, J., Jr. (2012). Near-Surface Void Detection Using a Seismic Landstreamer and Horizontal Velocity and Attenuation Tomography. *Symposium on the Application of Geophysics to Engineering and Environmental Problems Proceedings*: 561-571. https://doi.org/10.4133/1.4721875

Buske, S. (1999). Three-dimensional pre-stack Kirchhoff migration of deep seismic reflection data. *Geophysical Journal International, 137*(1), 243–260. https://doi.org/10.1046/j.1365-246x.1999.00789.x

Campman, X., Behn, P., & Faber, K. (2016). Sensor density or sensor sensitivity? *The Leading Edge, 35*(7), 578-585. https://doi.org/10.1190/tle35070578.1

Chalikakis, K., Plagnes, V., Guerin, R., Valois, R., & Bosch, F.P. (2011). Contribution of geophysical methods to karst-system exploration: an overview. *Hydrogeology Journal, 19*(6), 1169–1180. https://doi.org/10.1007/s10040-011-0746-x

Castañeda Marin, H. (2016). System Identification Method by Structural Similarity for Seismic Migration. *International Journal of Geology, 10*, 18-23.

Chang, W., & McMechan, G. (1987). Elastic Reverse-time Migration. *Geophysics, 52*(10), 1365-1375. https://doi.org/10.1190/1.1442249

Chattopadhyay, S., & McMechan, G. (2008). Imaging conditions for pre-stack reverse-time migration. *Geophysics, 73*(3), S81-S89. https://doi.org/10.1190/1.2903822

Christensen, N., & Stanley, D. (2003). Seismic Velocities and Densities of Rocks. *International Handbook of Earthquake and Engineering Seismology, 81B*,1587-1593. ISBN: 0-12-440658-0

Courant, R., Friedrichs, K., Lewy, H. (1928). Über die partiellen Differenzengleichungen der mathematischen Physik. *Mathematische Annalen (in German)*, *100*(1), 32–74. https://doi.org/10.1007/BF01448839

Courant, R., Friedrichs, K., Lewy, H. (March 1967) [1928]. On the partial difference equations of mathematical physics. *IBM Journal of Research and Development, 11*(2), 215–234. https:/doi.org/10.1147/rd.112.0215, MR 0213764

Dean, T. (2012). Land seismic: the 'quiet' revolution. *Engineering, Geology, Environmental Science*, 38-41. https://doi.org/10.1071/PVv2012n157p38

Donnelly-Nolan, J. (2010). Geologic map of Medicine Lake volcano, northern California (Scientific Investigations Map No. Scientific Investigations Map 2927). U.S. Department of the Interior, U.S. Geological Survey.

Du, X., Bancroft, J.C., Lawton, D.C., & Lines, L.R. (2006). Evaluations of prestack anisotropic Kirchhoff, Phase-shift-plus interpolation and reverse-time depth migration methods for dipping TI media. *SEG Technical Program Expanded Abstracts, 25*(1). https://doi.org/10.1190/1.2369873

Esmaeili, S., Kruse, S., Jazayeri, S., Whelley, P., Bell, E., Richardson, J., Garry, W.B., & Young, K. (2020). Resolution of Lava Tubes with ground penetrating radar: The TubeX project. *Journal of Geophysical Research: Planets*, 125, 1-23. https://doi.org/10.1029/2019JE006138

Feigenbaum, D., Sloan, S., Simpson, D., Coronel, W., & Smith, J. (2019). Near-surface void detection in karst terrain using first arrival tomography. *SEG Technical Program Expanded Abstracts*: 2792-2797. https://doi.org/10.1190/segam20193212401.1

Gazdag, J. (1978). Wave equation migration with the phase-shift method. *Geophysics, 43*(7), 1342-1351. https://doi.org/10.1190/1.1440899

GeoSci Developers (2017). Geophysics for Practicing Geoscientists. https://gpg.geosci.xyz/

Geuzaine, C. & Remacle, J. (2009). Gmsh: A 3-D finite element mesh generator with built-in pre- and post-processing facilities. *International Journal for Numerical Methods in Engineering, 79*, 1309–1331. https://doi.org/10.1002/nme.2579

Geuzaine, C. & Remacle, J. (2022). Gmsh Reference Manual. Gmsh ver. 4.10.5.

Gilbert, F. & Knopoff, L. (1960). Seismic scattering from topographic irregularities. *Journal of Geophysical Research, 65*(10). https://doi.org/10.1029/JZ065i010p03437

Glaser, D., Burch, K., Brinkley, D., & Reppert, P. (2021). Localization of deep voids through geophysical signatures of secondary dewatering features. *Geophysics, 86*(3), WA139-WA152. https://doi.org/10.1190/geo2020-0491.1

Gullikson, A.L., Rumpf, M.E., Edgar, L.A., Keszthelyi, L.P., Skinner, J.A., Jr., & Thompson, L. (2021) A geologic field guide to S P Mountain and its lava flow, San Francisco Volcanic Field, Arizona. *U.S. Geological Survey Open-File Report 2021–1072*, 1-37. https://doi.org/10.3133/ofr20211072

Gritto, R., Korneev, V.A., & Daley, M.T. (2004). Surface-to-tunnel seismic tomography studies at Yucca Mountain, Nevada. *Journal of Geophysical Research, 109*, 1-14. https://doi.org/10.1029/2002JB002036

Haruyama, J., Kioki, K., Shirao, M., Tomokatsu, M., Hiesinger, H., van der Bogert, C., Miyamoto, H., Iwasaki, A., Yokota, Y., Ohtake, M., Matsunaga, T., Hara, S., Nakanotani, S., & Pieters, C. (2009). Possible lunar lava tube skylight observed by SELENE cameras. *Geophysical Research Letters, 36*(21). https://doi.org/10.1029/2009GL040635

Haruyama, J., Hiesinger, H., & van der Bogert, C. (2010). Observation of Possible Lava Tube Skylights by SELENE cameras. *38th COSPAR Scientific Assembly*.

Hurwitz, D., Head, J., & Hiesinger, H. (2013) Lunar sinuous rilles: Distribution, characteristics, and implications for their origin. *Planetary and Space Sciences*, *79-80*, 1-38. https://doi.org/10.1016/j.pss.2012.10.019

Kaku, T., Haruyama, J., Miyake, W., Kumamoto, A., Ishiyama, K., Nishibori, T., Yamamoto, K., Crites, S.T., Michikami, T., Yokota, Y., Sood, R., Melosh, H.J., Chappaz, L., & Howell, K.C. (2017). Detection of Intact Lava Tubes at Marius Hills on the Moon by SELENE (Kaguya) Lunar Radar Sounder. *Geophysical Research Letters, 44*(10), 10155-10161. https://doi.org/10.1002/2017GL074998

Kalita, H., Quintero, A., Wissing, A., Haugh, B., Angie, C., Nail, G., Wilson, J., Richards, J., Landin, J., Kukkala, K., Vazquez, M., Tan, N., Lamey, Q., Lu, R., Peralta, R., Vilvanathan, V., & Thangavelautham, J. (2021). Evaluation of Lunar Pits and Lava Tubes for Use as Human Habitats. *Earth and Space 2021*, 944-957. https://doi.org/10.1061/9780784483374.086

Komatitsch, D., & Vilotte, J.-P. (1998). The spectral element method: An efficient tool to simulate the seismic response of 2D and 3D geological structures. *Bulletin of the Seismological Society of America, 88*(2), 368-392. https//doi.org/10.1785/BSSA0880020368

Kruger, J., Smith, A., & Welhan, J. (2002). Microgravity and magnetic detection of mafic dikes, fissures, and lava tubes in basalt: Potential barriers and fast-flow paths for contaminant migration within the eastern Snake River Plain, Idaho. *SEG Technical Program Expanded Abstracts*: 1440-1443. https://doi.org/10.1190/1.1816933

Lee, D., Chung, D., & Seo Kim, Y., (2023). Efficient source wavefield reconstruction for full-waveform inversion. *Geophysics, 88*, 769-788. https://doi.org/10.1190/geo2022-0570.1

Lewis, T.S., Kraft, D.W., & Hom, N. (1976). Scattering of elastic waves by a cylindrical cavity in a solid. *Journal of Applied Physics, 47*(5), 1795-1798. https://doi.org/10.1063/1.322894

Leveille, R. (2011). Life in Antarctic deserts and other cold dry environments: astrobiological analogs. Edited by P.T. Doran, W.B. Lyons & D.M. McKnight, Cambridge University Press, Cambridge, 2010. ISBN 10 9780521889193. *Antarctic Science. 23*. 414-415. https://doi.org/10.1017/S0954102011000502.

Liu, Y., Wu, R.-S., & Ying, C.F. (2000). Scattering of elastic waves by an elastic or viscoelastic cylinder. *Geophysics Journal International, 142*(2), 439–460. https://doi.org/10.1046/j.1365-246x.2000.00173.x.

Lognonné, P., Banerdt, W.B., Pike, W.T. et al. (2020) Constraints on the shallow elastic and anelastic structure of Mars from InSight seismic data. *Nature Geoscience, 13*, 213–220. https://doi.org/10.1038/s41561-020-0536-y

Mahvelati, S., & Coe, J.T. (2020) Revisiting Lunar Seismic Experiment Data Using the Multichannel Simulation with One Receiver (MSOR) Approach and Random Field Modeling. *Earth Moon Planets, 124*, 73–90. https://doi.org/10.1007/s11038-020-09536-6

Marfurt, K. (1984). Accuracy of finite-difference and finite-element modeling of the scalar and elastic wave equations. *Geophysics 1984, 49*(5), 533–549. https://doi.org/10.1190/1.1441689

Margrave, G.F., & Lamoureux, M.P. (2019). Numerical Methods of Exploration Seismology: With Algorithms in MATLAB®. *Cambridge University Press*. https://doi.org/10.1017/9781316756041

Martin, R. & Benaroya, H. (2023). Pressurized lunar lava tubes for habitation. *Acta Astronautica, 204*, 157-174. https://doi.org/10.1016/j.actaastro.2022.12.013

Marusiak, A., Schmerr, N., Bands, & M., Daubar, I. (2020). Terrestrial single-station analog for constraining the martian core and deep interior: Implications for InSight. *Icarus, 335*. https://doi.org/10.1016/j.icarus.2019.113396

McKay, D.S., Heiken, G., Basu, A., Blanford, G., Simon, S., Reedy, R., French, B., & Papike, J. (1991). The Lunar Regolith. Chapter 7 in *The Lunar Sourcebook*. Cambridge University Press, 1991.

Meglich, T. M., Williams, M. C., Hodges, S. M., & DeMarco, M. J. (2003). Subsurface geophysical imaging of lava tubes, Lava Beds National Monument. CA. *Geophysics*.

Miller, D.M. & Steeples, D.W. (1991). Detecting voids in a 0.6 m coal seam, 7 m deep, using seismic reflection. *Geoexploration, 28*(2), 109- 119. https://doi.org/10.1016/0016-7142(91)90043-C

Mirzanejad, M., Tran, K., McVay, M., Horhota, D., & Wasman, S. (2021). Deep void detection with 3D seismic waveform tomography. *SEG Global Meeting Abstracts*: 256-260. https://doi.org/10.1190/iceg2021-066.1

Morgan, P., Grott, M., Knapmeyer-Endrun, B. et al. (2018). A Pre-Landing Assessment of Regolith Properties at the InSight Landing Site. *Space Science Reviews, 214*(104). https://doi.org/10.1007/s11214-018-0537-y

Mouginis-Mark, P. & Wilson, L. (2022). Terrestrial Analogs to Planetary Volcanic Phenomena. *Oxford Research Encyclopedia of Planetary Science*. https://doi.org/9780190647926.013.253

Mousavi, J., Radad, M., Soleimani Monfared, M. et al. (2022). Fault Enhancement in Seismic Images by Introducing a Novel Strategy Integrating Attributes and Image Analysis Techniques. *Pure Appl. Geophys. 179*, 1645–1660. https://doi.org/10.1007/s00024-022-03014-y

National Academies of Sciences, Engineering, and Medicine (2023). Origins, Worlds, and Life: A Decadal Strategy for Planetary Science and Astrobiology 2023-2032 (2023). *Washington, DC: The National Academies Press*. https://doi.org/10.17226/26522

National Aeronautics and Space Administration (2020a). ARTEMIS PLAN: NASA's Lunar Exploration Program Overview. National Aeronautics and Space Administration (2020b). Artemis III Science Definition Team Report.

National Aeronautics and Space Administration (2020b). Artemis III Science Definition Team Report.

Nilsson, J. & Akenine- Möller, T. (2020). Understanding SSIM. *NVIDIA*. arXiv:2006.13846v2

Nolan, J., Sloan, S., Broadfoot, S., McKenna, J., & Metheny, O. (2011). Near-surface void identification using MASW and refraction tomography techniques. *SEG* Technical Program Expanded Abstracts: 1401-1405. https://doi.org/10.1190/1.3627464

Nolan, J., Miller, R., Ivanov, J., Peterie, S., & Lindgren, D. (2013). Near-surface salt dissolution void identification using passive MASW. *SEG Technical Program Expanded Abstracts*: 2212-2217. https://doi.org/10.1190/segam2013-1146.1

Northup, D.E. et al. (2012). Life in Earth's Lava Caves: Implications for Life Detection on Other Planets. In: Hanslmeier, A., Kempe, S., Seckbach, J. (eds) Life on Earth and other Planetary Bodies. *Cellular Origin, Life in Extreme Habitats and Astrobiology*, *24*. Springer, Dordrecht. https://doi.org/10.1007/978-94-007-4966-5_26

Nunn, C., Garcia, R.F., Nakamura, Y. Marusiak, A., Kawamura, T., Sun, D., Margerin, L., Weber, R., Drilleau, M., Wieczorek, M., Khan, A., Rivoldini, A., Lognonné, P., &

Zhu, P. (2020). Lunar Seismology: A Data and Instrumentation Review. *Space Science Reviews, 216*(89), 1-39. https://doi.org/10.1007/s11214-020-00709-3

Onodera, K., Kawamura, T., Tanaka, S., Ishihara, Y., & Maeda, T. (2022). Quantitative Evaluation of the Lunar Seismic Scattering and Comparison Between the Earth, Mars, and the Moon. *Journal of Geophysical Research: Planets, 127*(12). https://doi.org/10.1029/2022JE007558

Paris, J.A., Davies, E.T., Tognetti, L., & Zahniser, C. (2019). Prospective lava tubes at hellas planitia. *The Journal of the Washington Academy of Sciences*. https://doi.org/10.48550/arXiv.2004.13156

Park, C.B., Miller, R.D., & Xia, J. (1999). Detection of near-surface voids using surface wave. *Proceedings of the Symposium on the Application of Geophysics to Engineering and Environmental Problems, EEGS*: 281-286. https://doi.org/10.3997/2214-4609-PDB.202.1999_031

Peterie, S., Miller, R., & Steeples, D. (2009). Diffraction imaging versus reflection processing for shallow void detection. *SEG Technical Program Expanded Abstracts*: 1421-1424. https://doi.org/10.1190/1.3255115

Phillips, C., Cascante, G., & Hutchinson, D. (2002). The Innovative Use of Seismic Surface Waves for Void Detection and Material Characterization. *Symposium on the Application of Geophysics to Engineering and Environmental Problems Proceedings: CAV8*. https://doi.org/10.4133/1.2927072

Pullan, S. E. (1990) Recommended standard for seismic (/radar) files in the personal computer environment. *Geophysics, 55*(9), 1260-1271. https://doi.org/10.1190/1.1442942

Reitz, G., Berger, T., & Matthiae, D. (2012). Radiation exposure in the moon environment. *Planetary and Space Science, 74*(1), 78-83.https://doi.org/10.1016/j.pss.2012.07.014

Richardson, J.A., Wilson, J.A., Connor, C.B., Bleacher, J.E., & Kiyosugi, K. (2017). Recurrence rate and magma effusion rate for the latest volcanism on Arsia Mons, Mars. *Earth and Planetary Science Letters, 458*, 170–178. https://doi.org/10.1016/j.epsl.2016.10.040

Riddle, G., Hickey, C., & Schmitt, D. (2010). Subsurface Tunnel Detection Using Electrical Resistivity Tomography and Seismic Refraction Tomography: A Case Study. *Symposium on the Application of Geophysics to Engineering and Environmental Problems Proceedings*: 552-562. https://doi.org/10.4133/1.3445481

Rosten, T. & Ramstad, T.A. (1998). Kirchhoff migration of 2-D post-stack seismic data after subband decomposition. *Proceedings 1998 International Conference on Image Processing, 3*, 353-357. https://doi.org/10.1109/ICIP.1998.999026

Sacchi & Hall (2022). SeismicLab. https://github.com/msacchi/SeismicLab. (2024)

Sauro F., Pozzobon, R., Massironi, M., De Berardinis, P., Santagata, T., & De Waele, J. (2020). Lava tubes on Earth, Moon and Mars: A review on their size and morphology revealed by comparative planetology. *Earth-Science Reviews, 209*. https://doi.org/10.1016/j.earscirev.2020.103288

Shearer, P.M. (2009). Introduction to Seismology Third Edition. *Cambridge University Press*. https://doi.org/10.18814/epiiugs/2010/v33i2/007

Sheehan, J., Doll, W., Watson, D., & Mandel, W. (2005). Detecting Cavities with Seismic Refraction Tomography: Can it Be Done? *Symposium on the Application of*

Geophysics to Engineering and Environmental Problems Proceedings: 989-1003. https://doi.org/10.4133/1.2923557

Sherman, C., Rector, J., Dreger, D., & Glaser, S. (2014). Seismic tunnel detection at Black Diamond Mines Regional Preserve. *SEG Technical Program Expanded Abstracts*: 2078-2082. https://doi.org/10.1190/segam2014-1591.1

Shoemaker, E. (1959). Impact mechanics at Meteor Crater, Arizona. *U.S. Geological Survey, Open-File Report 59-108*. https://doi.org/10.3133/ofr59108

Sloan, D., Peterie, S., Ivanov, J., Miller, R., & McKenna, J. (2010). Void Detection Using Near-Surface Seismic Methods. *Geophysical Developments Series: 201-218*. https://doi.org/10.1190/1.9781560802259.ch12

Sloan, S., Peterie, S., Miller, D., Ivanov, J., McKenna, J., Broadfoot, S., & Metheny, S. (2012). Tunnel detection using near-surface seismic methods. *SEG Technical Program Expanded Abstracts*: 1-5. https://doi.org/10.1190/segam2012-1442.1

Smitha, N., Bharadwaj, D.R.U., Abilash, S., Sridhara, S.N., & Singh, V. (2016). Kirchhoff and F-K migration to focus ground penetrating radar images. *Geo-Engineering, 7*(4), 1-12. https://doi.org/10.1186/s40703-016-0019-6

Sollberger, D., Schmelzbach, C., Robertsson, J., Greenhalgh, A., Nakamura, Y., & Khan, A. (2016). The shallow elastic structure of the lunar crust: New insights from seismic wavefield gradient analysis. *Geophysical Research Letters, 43*(19). https://doi.org/10.1002/2016GL070883

Stolt, R.H. (1978). Migration by Fourier transform. *Geophysics, 43*(1), 24-48. https://doi.org/10.1190/1.1440826

Tezuka, A. (2006). Finite Element and Finite Difference Methods. In: Czichos, H., Saito, T., Smith, L. (eds) Springer Handbook of Materials Measurement Methods. *Springer Handbooks*. Springer, Berlin, Heidelberg. https://doi.org/10.1007/978-3-642-16641-9_19

The MathWorks, Inc. (2022). MATLAB version: 23.2.0.2515942 (R2023b). Available: https://www.mathworks.com.

Thienat, A., Modiriasari, A., Bobet, A., Melosh, H., Dyke, S., Ramirez, J., Maghareh, A., & Gomez, D. (2020). Lunar lava tubes: Morphology to structural stability. *Icarus, 338*. https://doi.org/10.1016/j.icarus.2019.113442

Torrese, P., Pozzobon, R., Rossi, A. P., Unnithan, V., Sauro, F., Borrmann, D., Lauterbach, H., & Santagata, T. (2021). Detection, imaging and analysis of lava tubes for planetary analogue studies using electric methods (ERT). *Icarus, 357*, 114912. https://doi.org/10.1016/J.ICARUS.2022.114912

Tromp, J., Komatitsch, D., & Liu, Q. (2008). Spectral-Element and Adjoint Methods in Seismology. *Communications in Computational Physics, 3*(1), 1-32. ISBN: 18152406

Tromp, J. (2015). 1.07 - Theory and Observations - Forward Modeling and Synthetic Seismograms, 3D Numerical Methods. *Treatise on Geophysics (Second Edition), 1*, 231-251. https://doi.org/10.1016/B978-0-444-53802-4.00006-3

van der Bogert, C. (2010). Marius Hills Pit - Lava Tube Skylight? *LROC*, https://www.lroc.asu.edu/posts/202

Virieux, J. & Operto, S. (2009). An overview of full-waveform inversion in exploration geophysics. *Geophysics, 74*(6), WCC1-WCC26. https://doi.org/10.1190/1.3238367

Wagner, R. & Robinson, S. (2014). Distribution, formation mechanisms, and significance of lunar pits. *Icarus, 237*, 52-60. https://doi.org/10.1016/j.icarus.2014.04.002.

Wang, Z., Simoncelli, E.P., & Bovik, A.C. (2003). Multi-scale structural similarity for image quality assessment. Proceedings of the 37th IEEE Asilomar Conference on Signals, Systems, and Computers.

Whelley, P., Garry, B., Yount, K., & Richardson, J. (2021). Skull Cave LiDAR Point Cloud – TubeX. *Digital Repository of the University of Maryland*. https://doi.org/10.13016/oxyt-vg4c

Wike, L. and Coonan, J., Kim, D., Ghent, R., Kruse, S., Lekic, V., Richardson, J., & Schmerr, N. (2022). Imaging heterogeneity in regolith using a joint ground penetrating radar and seismology approach. *53rd Lunar and Planetary Science Conference*: 2357.

Xia, J., Nyquist, J., Xu, Y., & Roth, M. (2006). Feasibility of Detecting Voids with Rayleigh-Wave Diffraction. *Symposium on the Application of Geophysics to Engineering and Environmental Problems Proceedings*: 1168-1180. https://doi.org/10.4133/1.2923575

Xiao, L., Zhu, P., Fang, G., Xiao, Z., Zou, Y., Zhao, J., Zhao, N., Yuan, Y., Qiao, L., Zhang, X., Zhang, H., Wang, J., Huang, J., Huang, Q., He, Q., Zhou, B., Ji, Y., Zhang, Q., Shen, S., Li, Y., & Gao, Y. (2015). A young multilayered terrane of the northern Mare Imbrium revealed by Chang'E-3 mission. *Science, 347*, 1226-1229. https://doi.org/10.1126/science.1259866

Yang, R., Chang, X., Ling, Y., Feng, Y.E. & Qu, L. (2020). Amplitude-compensated Laplacian filtering of reverse time migration and its application. *Geophysical Prospecting, 68*, 1089-1096. https://doi.org/10.1111/1365-2478.12881

Yao, G., Wu, D. & Debens, H. (2016). Adaptive finite difference for seismic wavefield modelling in acoustic media. *Sci. Rep., 6*. https://doi.org/10.1038/srep30302

Youn, O.K. & Zhou, H. (2001). Depth imaging with multiples. *Geophysics 66* (1), 246–255. https://doi.org/ 10.1190/1.1444901

Zanetti, M., Miller, K., Whetsel, C., King, W., Hayward, E., & Bremner, P.M. (2024). Better than 10m GPS-Denied Navigation Accuracy with the Kinematic Navigation and Cartography Knapsack (KNaCK) LiDAR System. *55th Lunar and Planetary Science Conference*: 2431.

Ziborov, V., Rostilov, T., Kronrod, E., Kuznetsov, I., & Dolnikov, G. (2024). Impact response of physical analog of Martian regolith. *International Journal of Impact Engineering, 104949*. https://doi.org/10.1016/j.ijimpend.2024.104949

Zhang, J., Yang, W., Hu, S., Lin, Y., Fang, G., Li, C., Peng, W., Zhu, S., He, Z., Zhou, B., Lin, H., Yang, J., Liu, E., Xu, Y., Wang, J., Yao, Z., Zou, Y., Yan, J., & Ouyang, Z. (2015). Volcanic history of the Imbrium basin: A close-up view from the lunar rover Yutu. *Proceedings of the National Academy of Sciences of the United States of America, 112*(17), 5342-5347. https://doi.org/10.1073/PNAS.1503082112

Zheng, Y., Malallah, A.H., Fehler, M.C., & Hu, H. (2016). 2D Full-Waveform Modeling of Seismic Waves in Layered Karstic Media. *Geophysics, 81*(2), T25–T34. DOI: 10.1190/GEO2015-0307.1

Zhou, W., A. C. Bovik, H. R. Sheikh, & E. P. Simoncelli. (2004). Image Quality Assessment: From Error Visibility to Structural Similarity. *IEEE Transactions on Image Processing, (13)*4, 600–612. https://doi.org/ 10.1109/TIP.2003.819861

Zhou, H., Hu, H., Zou, Z., Wo Y., & Youn, O. (2018). Reverse time migration: A prospect of seismic imaging methodology. *Earth-Science Reviews, 179*, 207-227. https://doi.org/10.1016/j.earscirev.2018.02.008

Zhu, J. & Lines, L.R. (1998). Comparison of Kirchhoff and reverse-time migration methods with applications to prestack depth imaging of complex structures. *Geophysics, 63*(4), 1166-1176. https://doi.org/10.1190/1.1444416